MEASUREMENT AND ANALYSIS OF CARDIAC TISSUE DURING ELECTRICAL STIMULATION

By

Mark Raymond Holcomb

Dissertation

Submitted to the Faculty of the

Graduate School of Vanderbilt University

in partial fulfillment of the requirements

for the degree of

DOCTOR OF PHILOSOPHY

in

Physics

August, 2007

Nashville, Tennessee

Approved:

Professor John P. Wikswo

Professor Richard A. Gray

Professor Richard F. Haglund

Professor Veniamin Y. Sidorov

Professor M. Shane Hutson

TABLE OF CONTENTS

Page

LIST OF TABLES v

LIST OF FIGURES vi

Chapter

I. INTRODUCTION 1

1.1. Objectives 1
1.2. Specific Aims 1

II. BACKGROUND AND SIGNIFICANCE 4

2.1. Introduction 4
2.2. The heart 5
2.3. Electrophysiology background 5
2.4. Hodgkin and Huxley membrane model 6
2.5. Propagating action potentials 10
2.6. Bidomain model 12
2.7. Cardiac action potentials 14
2.8. Fluorescence imaging of cardiac tissue 15
2.9. Field stimulation 16
2.10. References 17

III. DATA ACQUSITION SYSTEM FOR CARDIAC STUDIES 20

3.1. Introduction 20
3.2. Overview 20

IV. USB POWERED AND CONTROLLED ISOLATED CONSTANT-CURRENT PHYSIOLOGICAL STIMULATOR 32

4.1. Abstract 32
4.2. Introduction 33
4.3. Stimulator Design 34
4.4. Discussion 46
4.5. References 48
4.6. Command Summary 49
4.7. Stimulator Parts List 51

V. DUAL CAMERA IMAGING SYSTEM FOR CARDIAC STUDIES.....53

5.1. Abstract.....53
5.2. Introduction.....54
5.3. Camera Hardware.....55
5.4. Image Alignment.....55
5.5. Results.....59
5.6. Discussion.....62
5.7. Acknowledgements.....63
5.8. References.....63

VI. HIGH-RESOLUTION HIGH-SPEED PANORAMIC CARDIAC IMAGING SYSTEM.....65

6.1. Abstract.....65
6.2. Introduction.....66
6.3. Experimental Setup.....69
6.3.1. Base Plate.....69
6.3.2. Perfusion System.....71
6.3.3. Illumination.....71
6.3.4. Cameras.....74
6.3.5. Rotation System.....75
6.3.6. Kinematic Mount.....76
6.3.7. Enclosure.....78
6.3.8. Computer Control.....79
6.4. Algorithms and Post Processing.....79
6.5. Results.....82
6.6. Discussion.....83
6.7. Acknowledgements.....83
6.8. References.....84

VII. FIELD STIMULATION OF THE DIASTOLIC RABBIT RIGHT VENTRICLE..85

7.1. Abstract.....85
7.1.1. Electroporation.....86
7.1.2. Virtual Electrode Polarization.....87
7.1.3. Fiber Geometry.....89
7.2. Materials and Methods.....90
7.2.1. Experimental Preparation.....90
7.2.2. Stimulation Protocol.....92
7.2.3. Optical Imaging.....93
7.2.4. Experimental Considerations.....94
7.2.5 Analysis Methods.....96
7.3. Protocol 1.....100
7.3.1. Complementary Shock Response.....100
7.3.2. Polarity Dependent Activation.....110

7.3.3. Hyperpolarization and Electroporation....113
7.3.4. Ancillary Procedures....122
7.3.5. Global Hyperpolarization....125
7.4. Protocol 2....130
7.5. Protocol 3....133
7.6. Conclusions....138
7.7. References....140

LIST OF TABLES

Table Page

4.1. Requested and measured small currents 42

4.2. Requested and measured large currents 42

LIST OF FIGURES

Figure		Page
2.1.	Hodgkin and Huxley measurements.	7
2.2.	Relative conductivities of Hodgkin and Huxley membrane model	7
2.3.	Non-linear core-conductor cable model of a nerve	10
2.4.	Schematic representation of the bidomain model	12
2.5.	Typical ventricular action potential.	15
3.1.	Timing diagrams for the S1, S1-S2, and S1-S2-S3 protocols	22
3.2.	Stimulation Entry Window.	23
3.3.	Panoramic three-camera main display.	27
3.4.	Laser control panel	30
4.1.	Schematic of the voltage controlled constant current source	35
4.2.	Stimulator components.	37
4.3.	Stimulator schematic	39
4.4.	Example of *Wavetrain* mode.	44
4.5.	Example of an enhanced mode stimulation sequence	46
5.1.	Dual camera system.	54
5.2.	Pixel mapping.	56
5.3.	Demonstration of numerical alignment of two-camera images.	60
5.4.	The voltage and calcium responses to anodal stimulation.	61
6.1.	System as seen from outside the Faraday cage	66
6.2.	Top view of the system base plate	69

6.3. One of the three cameras and its mount on the Delrin track....70
6.4. An LED mounted on CPU heat sink and fan with a motorized shutter....71
6.5. Emission spectrum of the green Luxeon Star/V LED (LXHL-LM5C)....72
6.6. The Z-translation stage....75
6.7. The three components of a kinematic mount....77
6.8. Screenshot of the control program during an experiment....79
6.9. Isosurface Display Toolbox....81
6.10. Figure of eight reentry during polymorphic tachycardia....82
7.1. RV bath and holder....92
7.2. Correlations....99
7.3. RV1 Endocardial Response....102
7.4. RV2 Endocardial Response....103
7.5. RV3 Endocardial Response....104
7.6. RV4 Endocardial Response....105
7.7. Cross-correlations....108
7.8. Cross-correlations....109
7.9. Proportion activated pixels....111
7.10. Temporal evolution....112
7.11. S2 response....114
7.12. S2 response....115
7.13. Post-shock resting potential shift....116
7.14. Rapid hyperpolarization after shock onset....117
7.15. Endocardial response of RV2....118

7.16. Resting offset vs. maximum hyperpolarization 120
7.17. Resting offset vs. maximum depolarization 121
7.18. Comparison of systolic and diastolic shocks 123
7.19. Response of RV2 to a 200 μs shock 124
7.20. Response of RV2 to a 10 ms 500 V shock 124
7.21. Distribution of individual pixel values 126
7.22. Strong shock correlations 128
7.23. Endocardial and epicardial activation times 131
7.24. Activation time differences 132
7.25. Pacing response of RV10 in different orientations 133
7.26. Anatomical MRI of RV10 134
7.27. RGB images of DTMRI of RV10 135
7.28. Shock response and subsequent resting offset of RV10 137

CHAPTER I

INTRODUCTION

1.1. Objectives

The objectives of this research were to develop and apply new instrumentation for use in fluorescence imaging studies of *ex-vivo* rabbit hearts investigating the response of cardiac tissue to electrical stimulation. Future development of pacemakers, defibrillators, and pharmacological treatments are dependent on understanding the heart's response to electrical stimulation. In order for the heart to perform its mechanical function of pumping blood, intricate, coordinated electrodynamic and chemical processes must take place. Trying to understand such a complex system in terms of first-principles is a worthwhile endeavor in itself.

The primary probes used in these studies are fluorescent dyes, whose spectra shift with changing transmembrane potential or intracellular calcium concentration. The fluorescence emitted by the dyes is collected via optical imaging techniques that yield high-spatial and high-temporal resolution data.

1.2. Specific Aims

Aim 1. Create a flexible software library that can be used to control multiple high-speed CCD cameras, illumination, and electrical stimulation. Our laboratory uses two types of cameras: the Dalsa DS-12-16K5H and the Redshirt Imaging CardioCCD-SMQ. The former has higher spatial resolution, and the latter has higher temporal

resolution capabilities. They can be used in combinations in multiple camera configurations. Integration and automation of the control of all experimental devices will improve experiment design and data analysis.

Aim 2 Design and construct a microcontroller-based constant-current electrical stimulator that is able to deliver complex biphasic stimulation sequences. The ability to provide a stimulus sequence with variable amplitude, polarity, duration, and period will allow experimental protocols that were previously not possible. Control of this stimulator is integrated in the software developed in Aim 1.

Aim 3 Design and construct a dual camera imaging system with camera calibration ability. A two camera system allows simultaneous measurement of two dynamic quantities, V_m (Transmembrane Potential) and $[Ca^{2+}]_i$, (Intracellular Calcium Concentration) from the same spatial region. A software-based camera calibration approach eliminates the need for precise camera alignment. The system is based on the software from Aim 1.

Aim 4 Design and construct a panoramic cardiac imaging system consisting of three cameras. The ability to image the entire epicardium will allow more thorough studies of non-localized phenomena, such as phase singularities and responses to defibrillation shocks, than is possible with a traditional single view configuration. The system is based on the software from Aim 1.

Aim 5 Examine the V_m dynamics of an isolated right ventricle under field-shock conditions. Structural heterogeneities are thought to play a prominent role in defibrillation success or failure. By removing curvature, which dominates the

response to field shock in whole hearts, the response of smaller heterogeneities can be studied. The measurements are made with the system from Aim 3.

CHAPTER II

BACKGROUND AND SIGNIFICANCE

2.1. Introduction

The heart is the first organ in a human embryo to become functional. Throughout the life of a human, the heart drives blood through the circulatory system, which delivers vital materials to the rest of the body as well as carries away waste products. Over the average life span of a human, the heart beats around three billion times. Any interruption in heart function lasting more than a few minutes results in death. Numerous types of cardiac disease have been identified that range from mechanical to electrical. The focus of this research is on the electrophysiology of the heart. Specifically, changes in transmembrane potential and calcium concentration under point and field stimulation are targets of this research.

Over 300,000 deaths in the United States each year are caused by sudden cardiac death [1]. The most common cause of sudden cardiac death is ventricular fibrillation. Once initiated, ventricular fibrillation in humans almost never terminates spontaneously. Ventricular fibrillation is characterized by uncoordinated contractions which prevent blood from being pumped through the cardiovascular system. If allowed to persist, death usually occurs within minutes. The application of strong electric shocks, termed defibrillation, is a very effective and well-established method of terminating fibrillation, but the underlying dynamics are still not well understood. A better understanding of the

heart's response to electrical stimulation can help improve the future design of defibrillators, pacemakers, and pharmacological treatments.

2.2. The Heart

The heart is comprised of four chambers. The upper two chambers, the atria, receive blood by way of veins returning from the body. The atria fill the two lower chambers, the ventricles, which in turn pump blood out of the heart. The heart is a dual pump in that the right and left sides are physically isolated by the septum. The ventricles and atria are electrically isolated except at the atrioventricular node. Four one-way valves ensure efficient operation of the heart by allowing blood to flow from veins to atria to ventricles to arteries only. The valves open and close passively due to pressure gradients. The left and right atrioventricular valves are positioned between the atria and ventricles on both sides. They allow ventricular filling while preventing backflow during ventricular contraction. The aortic valve and pulmonary valve are located at the juncture where blood leaves the left and right ventricles, respectively.

2.3. Electrophysiology Background

Physicist and physician Luigi Galvani is credited with discovering a relationship between electricity and biology. Around 1780, while dissecting a frog at a table where he had recently been conducting static electricity experiments, he touched the frog with a charged metal instrument and noticed the leg twitch. Scientists at the time were very interested in investigating this relationship, but a modern understanding of electromagnetism and statistical mechanics would not come until much later. The most

significant work in bioelectricity was reported by Hodgkin and Huxley (HH) in a series of five papers in 1952 [2,3,4,5,6]. Using newly available instrumentation and considerable physical insight, HH developed the modern channel-based model of an electrically active cell membrane. The HH model was derived from data collected from experiments on a squid giant axon.

2.4. Hodgkin and Huxley Membrane Model

From previous experiments HH knew that Na^+ and K^+ accounted for most of the current across the membrane of a squid giant axon. By manipulating the ionic concentrations they isolated the contribution of each ion to the membrane current seen in their voltage clamp experiments.

Figure 2.1A shows the total membrane current as measured in a voltage clamp experiment on a squid giant axon. In this particular experiment V_m is taken from the resting potential of -60 mV to 0V in a step fashion. By placing the axon in a bath with Na^+ concentration equal to the interior, they created a Na Nernst potential of 0V. When the experiment is repeated there is no Na^+ membrane current, and the measured current is due only to K^+. The individual currents are shown in Figure 2.1B. HH also used channel blocking toxins to isolate specific currents.

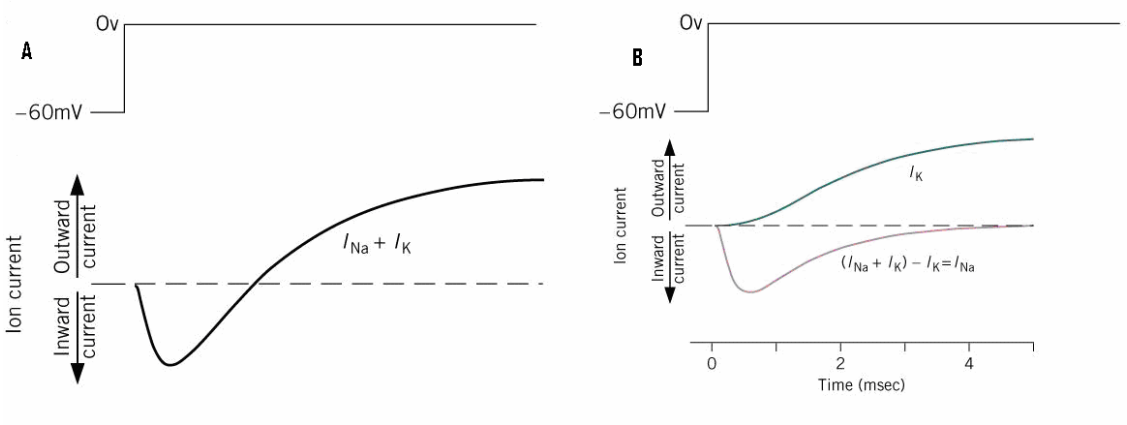

Figure 2.1. Hodgkin and Huxley measurements. (a) total current measurement from voltage clamp experiment. (b) individual ionic currents.

By performing many similar experiments, HH were able to determine the conductivities during an action potential. The relative conductivities and action potential are superimposed in Figure 2.2.

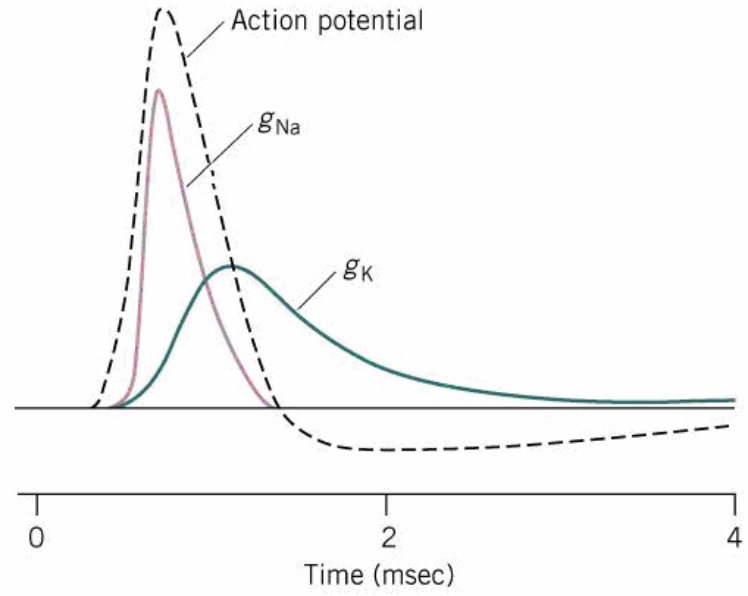

Figure 2.2. Relative conductivities of Hodgkin and Huxley membrane model during an action potential.

These were interesting phenomenological data, but HH wanted a more quantitative understanding of membrane function. They started with the equation

$$g_K(t,v) = \overline{g_K} n^4(t,v_m), \tag{2.4}$$

where $\overline{g}_K$ is the maximum conductivity which requires $0 \le n \le 1$ for consistency. HH arrived at the '4' as the exponent of Equation 2.4 by curve-fitting their K data. They surmised that *n* represents the probability of a "gate" being open, with four such gates being in each channel, and all have the same probability of being open. All four gates must be open for the channel to be open; hence the probability of a channel being open is n^4. Later investigations in channel structure confirmed this hypothesis.

At this point the problem of determining the K conductivity is one of finding $n(t,V_m)$. The measured $g_k(t)_v$ in the voltage clamp experiments all had the same basic asymptotic shape approaching a constant conductivity for a fixed voltage. Assuming the time rate of change in *n* obeys first order kinetics, HH wrote

$$\frac{dn(t,v_m)}{dt} = \alpha_n(v_m)(1-n) - \beta_n(v_m)n \quad . \tag{2.5}$$

With this formulation, the rate constants are functions of V_m only and can be determined from the voltage clamp data. This is a first order differential equation with constant coefficients and can be solved analytically. To do this, Equation 2.5 can be rewritten as

$$\int \frac{dn(t)_v}{\alpha_n - n(\alpha_n + \beta_n)} = \int dt \quad . \tag{2.6}$$

When Equation 2.6 is integrated and simplified it becomes

$$n(t,v_m) = \frac{\alpha_n - e^{\frac{-t}{\alpha_n+\beta_n}}}{\alpha_n + \beta_n} \tag{2.7}$$

With substitutions $\tau_n = \frac{1}{(\alpha_n - \beta_n)}$ and $n_\infty = \frac{\alpha_n}{(\alpha_n + \beta_n)}$ inserted in to 2.7, we obtain the standard form of *n* as a function of time

$$n(t) = n_\infty - (n_\infty - n_0)e^{\frac{-t}{\tau_n}} \tag{2.8}$$

A similar model for the sodium conductivity was also derived by HH

$$g_{Na}(t, V_m) = \overline{g_{Na}} m^3(t, V_m) h(t, V_m) \quad . \tag{2.9}$$

When Equation 2.9 is solved in a similar manner as Equation 2.4, one obtains

$$m(t) = m_\infty - (m_\infty - m_0)e^{\frac{-t}{\tau_m}} \tag{2.10}$$

and

$$h(t) = h_\infty - (h_\infty - h_0)e^{\frac{-t}{\tau_h}} \quad . \tag{2.11}$$

The variable *m* plays the same role as *n* in the K formulation, but *h* is added to better fit the voltage clamp data. The variables *m* and *h* are often called the activation and inactivation parameters. The inactivation parameter is understood to represent the probability of a channel remaining open.

For some length of time after an action potential the tissue cannot be stimulated again, a state termed absolutely refractory. Later the tissue goes into a relative refractory state in which it is possible to be stimulated, but requires a large stimulus. Other important properties such as break excitation and degraded response can be understood in terms of the HH formulation.

Shortly after HH published their physiologically based model, FitzHugh proposed a simplified mathematical model [7]. The FitzHugh-Nagumo model preserves much of the interesting behavior of the HH model, but uses only two variables. It also lacks the

numerous exponentials which are computationally expensive. The first variable represents excitability, and the second variable represents recovery.

2.5. Propagating Action Potentials

In order to understand how an action potential travels down a nerve, a structural model is needed. A simple model is shown in Figure 2.3a. This model represents a nerve as two conductors connected together periodically by resistive and capacitive elements that represent the membrane. Figure 2.3b shows the connecting elements in terms of capacitance per unit length, the Nernst potentials, and the conductivities per unit length. If ΔX is small compared to the width of an action potential, then this is a reasonable

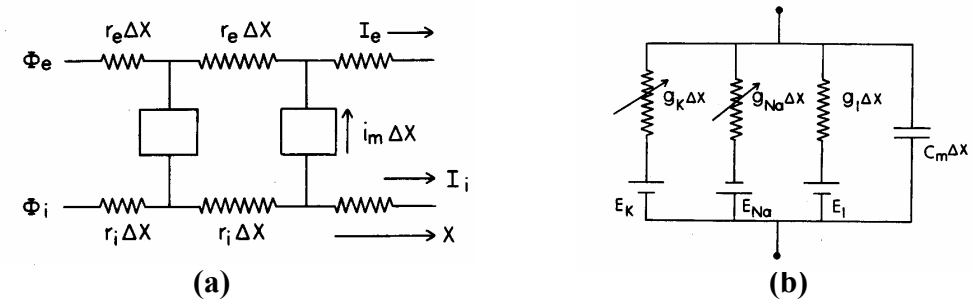

Figure 2.3. Non-linear core-conductor cable model of a nerve. (a) external (e subscripts) and internal (i subscripts) passive spaces are separated by the active membrane (m subscript). (b) parallel conductance model. Each membrane element (the boxes) in (a) is represented by (b). K, Na, and l (the leakage) conductivities are represented as resistors. The Nernst potentials for each species are represented by batteries. The membrane capacitance is represented by C_m.

The membrane current per unit length, i_m, in Figure 2.3a is determined by the Nernst potentials, E_K, E_{Na}, E_l and conductivities and V_m. The displacement current (i_d), given below in Equation 2.12, does not cross the membrane, but is a major factor in

impulse propagation. It determines how much charge leaves the membrane in *dt*, and affects the locally calculated V_m used in the subsequent iteration.

$$i_d = c_m \frac{dV_m}{dt} \tag{2.12}$$

$$j_m = g_{Na}(V_m - V_{Na}) + g_K(V_m - V_K) + g_L(V_m - V_L) \tag{2.13}$$

Application of charge conservation to an intercellular point gives two currents: i_m which crosses the membrane and i_d which changes the charge on the membrane. Ohm's law gives

$$i_i(x) = -\frac{1}{r_i}\frac{dV_m}{dx} \tag{2.14}$$

$$\frac{\partial V_m}{\partial t} = -\frac{j_m}{c_m} + \frac{1}{2\pi a r_i c_m}\frac{\partial^2 V_m}{\partial x^2} \tag{2.15}$$

The internal resistance per unit length is given by

$$r_i = \frac{1}{2\pi a^2 \sigma_i} \quad . \tag{2.16}$$

The resting V_m occurs when the net membrane current is zero. By setting (2.13) equal to zero and solving for V_m, V_{rest} can be expressed in terms of the Nernst potentials and conductivities

$$V_{rest} = \frac{g_K v_K + g_{Cl} v_{Cl} + g_{Na} v_{Na}}{g_K + g_{Cl} + g_{Na}} \quad . \tag{2.14}$$

This expression gives the resting potential for the HH membrane model. For any membrane with ionic species *j* with conductivity g_j and Nernst potential V_j, the resting potential is

$$V_{rest} = \frac{\sum g_j V_j}{\sum g_j} \quad . \tag{2.15}$$

2.6. Bidomain Model

A simple one dimensional cable model does not adequately describe the structure of cardiac tissue. A cardiac cell is approximately 100 μm in length and 20 μm in diameter. Each cell is connected to approximately 10 other cells by junctions. The cells are arranged as staggered bricks in a plane, and the cells are grouped in fibers which form sheets. Arvanitaki, Schmitt, Tung, Geselowitz and Miller were the primary creators of the bidomain model, which offers a realistic computational model of cardiac tissue [8-11]. The bidomain model uses averaged properties represented in two discrete regions separated by a membrane. While the geometry is complex, a current can conceivably flow from one cardiac cell to any other cell without going through the membrane. The second space, the extracellular space, is the fluid that surrounds the tissue. These two domains are separated by the membrane. A schematic representation is shown in Figure 2.4

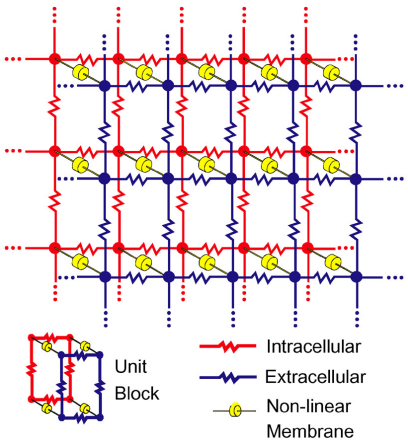

Figure 2.4. Schematic representation of the bidomain model [12].

Application of the bidomain model is complicated by the anisotropic nature of the heart. Early implementations of the bidomain model assumed equal anisotropies for computational ease. In real cardiac tissue the conductivity ratios are not equal [13]. The intercellular to extracellular conductivity ratio is approximately 10:1 along the fiber direction but only approximately 4:1 traverse to the fiber direction. Incorporation of the unequal anisotropies in the bidomain model of cardiac tissue led to good agreement with experimental results [14,15]. For example, with unequal anisotropy ratios the bidomain model predicts that under anodal point stimulation a "dog bone" shaped region of hyperpolarization centered on the electrode and aligned transverse to the fiber direction will form. This "dog bone" is flanked by two regions of depolarization, termed "virtual cathodes", lying in the convex portions of the "dog bone", aligned along the fiber direction [15]. The bidomain model is described by two coupled first-order partial differential equations:

$$\nabla \cdot \tilde{\sigma}_i \nabla V_i = \beta(C_m \partial V_m / \partial t + J_{ion}) - I_i \tag{2.16}$$

$$\nabla \cdot \tilde{\sigma}_e \nabla V_e = -\beta(C_m \partial V_m / \partial t + J_{ion}) - I_e \tag{2.17}$$

where $\tilde{\sigma}_i$ and $\tilde{\sigma}_e$ are the electrical conductivities of the intracellular and extracellular spaces, respectively. C_m is membrane capacitance per unit area, β is the ratio of cell membrane area to tissue volume, J_{ion} is the membrane ionic current per unit area, and I_i and I_e are the intracellularly-applied and extracellularly-applied external current sources per unit volume, respectively. V_i, V_e, and V_m are the intracellular, extracellular, and transmembrane potentials, respectively.

2.7. Cardiac Action Potential

A cardiac action potential was first measured by Coraboeuf and Weidmann in 1948 [16]. Figure 2.5 shows a typical ventricular action potential. There is a marked difference in shape and duration when compared to the HH-type nerve action potential. Using the HH paradigm, many channel-based models have been developed that accurately describe the cardiac action potential. The Luo-Rudy 91 (LR) model is one modern model [17]. Several versions of LR models have been developed, with some improving on previous models, and some designed to be used in special circumstances such as examining defibrillation shocks. Resting V_m is normally approximately -85 mV. The upstroke phase, phase 0, occurs when threshold is reached, and the voltage-gated Na^+ channels open. Na^+ rushes in and raises V_m to approximately +25 mV, and the Na^+ channels close. A short repolarization after the initial upstroke, Phase 1, is caused by outward K^+ currents. The plateau, Phase 2, lasts 200-300 ms, and is very different from the simple HH action potentials. An inward Ca^{2+} current which is not present in the HH model, balances the outward K^+ current. Contraction of the heart occurs during this phase. At the end pf the plateau phase, the Ca^{2+} channels close and additional K^+ channels open, causing V_m to decrease (Phase 3). Ion concentrations approach resting levels via pumps and exchangers, and V_m approaches rest, Phase 4.

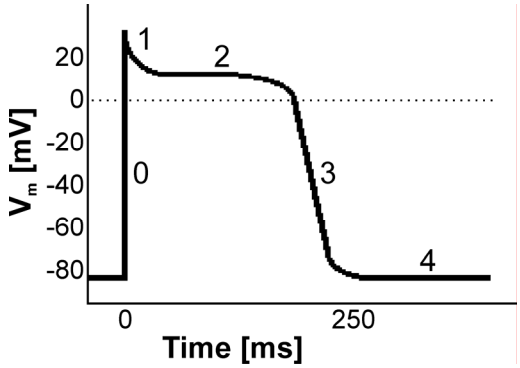

Figure 2.5. Typical ventricular action potential. Phases of action potential : (0) upstroke, (1) early repolarization, (2) plateau, (3) repolarization, and (4) diastole.

2.8. Fluorescence Imaging Of Cardiac Tissue

Optical mapping is currently the most common method to collect high spatial and temporal data of the electrical activity in cardiac tissue. A fluorescent dye was first used in cardiac studies by Salama and Morad in 1976 while studying frog hearts [18]. Fluorescent dyes work by using a fluoroprobe that is sensitive to changes in transmembrane potential, or some other dynamic quantity such as $[Ca^{2+}]_i$, When voltage sensitive dyes are introduced, usually through the perfusion system in whole heart studies, many become affixed inside the membrane. As the transmembrane potential changes, so does the fluorescence spectrum. Many voltage dyes are available which have varying levels of toxicity, as well as differences in absorption and emission spectra, signal-to-noise ratio, and dynamic range. Di-4 ANEPPS, the voltage sensitive dye used in most of our experiments, has been found to be linear over a range of -280 mV to 100 mV, which includes the range of interest in normal cardiac action potentials [19].

By convention, the signal is expressed as $-\Delta F/F$ where F is the strength of the fluorescence signal from a pixel imaging resting tissue, and ΔF is the difference between F and the current intensity recorded by the pixel. The fluorescence signal from most

voltage dyes shift toward shorter wavelengths when the tissue is depolarized. Long-pass filters are normally used in recording fluorescence signals; therefore, the negative inverts the signal so that a more positive number corresponds to depolarized tissue.

One disadvantage of optical mapping is the translucent epicardium, layers of tissue beneath the surface, which gives a depth-weighted average of transmembrane potential, not just the surface of the tissue [20]. Depth estimates range from 300-500 microns [19,21] up to 1-2 mm [22-24]. Another disadvantage of optical mapping is excitation-contraction decouplers are usually required to prevent motion. These drugs do affect the action potential and restitution curve. They are also toxic to the heart. The decouplers do not eliminate all motion, and some motion artifacts can be visible in the data.

2.9. Field Stimulation

In 1899 Prevost and Batelli demonstrated that a strong electrical stimulus could stop ventricular fibrillation in dogs [25]. Beck, Prichard, and Feil reported successful electrical defibrillation of a human heart in 1947 [26]. Electrical defibrillation has become standard treatment for human patients in ventricular tachycardia or fibrillation. Although electrical defibrillation is commonly used, the mechanisms which lead to successful defibrillation are poorly understood. In terms of a simple cable model, cardiac tissue has a length-constant of approximately 1 mm. Therefore, most regions of a large heart should be unaffected by an externally applied stimulus. Activation that has been observed at large distances from the electrodes has been termed “far-field” stimulation. Many explanations have been offered for far-field stimulation, most of which propose

that heterogeneities at various scales are responsible for the effect. More data is needed to substantiate the theories. The final chapter of this dissertation presents new data describing far-field stimulation of an isolated rabbit right ventricle.

2.10. References

1 Zipes, D.P. and Wellner, M., "Sudden cardiac death." Circulation, vol. 98, no. 21, pp. 2334-2351, 1998.

2 Huxley, A.L. and Hodgkin, A.F., "Measurement of Current-Voltage Relations in the Membrane of the Giant Axon of Loligo". Journal of Physiology 1: 424-448, 1952(a).

3 Huxley, A.L. and Hodgkin, A.F., "Currents Carried by Sodium and Potassium Ions Through the Membrane of the Giant Axon of Loligo". Journal of Physiology 1:449-472, 1952 (b).

4 Huxley, A.L. and Hodgkin, A.F., "The Components of Membrane Conductance in the Giant Axon of Loligo". Journal of Physiology 1: 473-496, 1952 (c).

5 Huxley, A.L. and Hodgkin, A.F., "The Dual Effect of Membrane Potential on Sodium Conductance in the Giant Axon of Loligo". Journal of Physiology 1: 497-506,1952 (d).

6 Huxley, A.F. and Hodgkin, A.L., "A Quantitative Description of Membrane Currentand Its Application to Conduction and Excitiation in Nerve". Journal of Physiology 1: 500-544, 1952 (e).

7 FitzHugh, R., "Impulses and physiological states in theoretical models of nerve membrane". Biophysical J. 1:445-466, 1961

8 Arvanitaki, A., "Effects evoked in an axon by the activity of a contiguous one". J Neurophys, vol. 5, pp. 89-108. 1942.

9 Schmitt, "Biological information processing using the concept of interpenetrating domains". In Information Processing in the Nervous System, K. N. Leibovic, editor. Springer-Verlag, New York pp 325-331. 1969.

10 Tung, L., "A bi-domain model for describing ischemic myocardial d-c potentials". Ph.D. dissertation, Massachusetts Institute of Technology, Cambridge, 1978.

11 Geselowitz, D.B. and Miller III W.T., “A bidomain model for anisotropic cardiac muscle”. Annals of Biomedical Engineering, vol. 11, pp. 191-206. 1983.

12 Lin, S.-F. and Wikswo, J. P., Jr., “New perspectives in electrophysiology from the cardiac bidomain”. in Rosenbaum, D. S. and Jalife, J. (eds.) *Optical Mapping of Cardiac Excitation and Arrhythmias.* Armonk, NY: Futura Publishing Company, Inc., 2001, pp. 335-359.

13 Roth, B.J., “Electrical conductivity values used with the bidomain model of cardiac tissue”. IEEE Trans Biomed Eng, vol. 44, no. 4, pp. 326-328, 1997.

14 Roth, B.J., “How the anisotropy of intracellular and extracellular conductivities influences stimulation of cardiac muscle”. J Math Biol, vol. 30, no. 6, pp. 633-646, 1992.

15 Wikswo, J.P. Jr., Lin, S.F., and Abbas, R.A., “Virtual electrodes in cardiac tissue: A common mechanism for anodal and cathodal stimulation”. Biophys J, vol. 69, no. 6, pp. 2195-2210, 1995.

16 Coraboeuf, E., Weidmann, S., Potentiel de repos et potetiel d’action du muscle cardiaque, measures a l’aide d’electrodes intracellulaire, C R Seances Soc Biol Fil. 1949;143:1329-1331.

17 Luo, C.H., Rudy, Y. “A model of the ventricular cardiac action potential. Depolarization, repolarization, and their interaction”. Circ Res 68:1501-26, 1991

18 Salama, G. and Morad, M., “Merocyanine 540 as an optical probe of transmembrane electrical activity in the heart”. Science, vol. 191, no. 4226, pp. 485-487, Feb.1976

19 Knisley, S.B., “Transmembrane voltage changes during unipolar stimulation of rabbit ventricle”, Circ Res, vol. 77, no. 6, pp. 1229-1239, 1995.

20 Gray, R.A., “What exactly are optically recorded action potentials,”. J Cardiovasc Electrophysiol, vol. 10, no. 11, pp. 1463-1466, 1999.

21 Girouard, S.D., Laurita, K.R., and Rosenbaum, D.S., “Unique properties of cardiac action potentials recorded with voltage-sensitive dyes”. J Cardiovasc Electrophysiol, vol. 7, no. 11, pp. 1024-1038, 1996.

22 Efimov, I.R., Sidorov, V., Cheng, Y., and Wollenzier, B., “Evidence of three-dimensional scroll waves with ribbon-shaped filament as a mechanism of ventricular tachycardia in the isolated rabbit heart”. J Cardiovasc Electrophysiol, vol. 10, no. 11, pp. 1452-1462, 1999.

23 Al-Khadra, A., Nikolski, V., and Efimov, I.R., “The role of electroporation in defibrillation”. Circ Res, vol. 87, no. 9, pp. 797-804, 2000.

24 Baxter, W.T., Mironov, S.F., Zaitsev, A.V., Jalife, J., and Pertsov, A.M., “Visualizing excitation waves inside cardiac muscle using transillumination”. Biophys J, vol. 80, no. 1, pp. 516-530, 2001.

25 Prevost, J.L., Battelli, F., La mort par les déscharges électriques (French: "Death by electrical discharges,". J. Physiol 1899;1:1085-1100.

26 Beck, C.S., Pritchard, W.H., Feil, H.S., “Ventricular fibrillation of long duration abolished by electric shock”. J Amer Med Assoc 1947;135:985

CHAPTER III

DATA ACQUISITION SYSTEM FOR CARDIAC STUDIES

3.1. Introduction

A large subset of current and future cardiac experiments conducted by John Wikswo's group requires the control of multiple high-speed CCD cameras, electrical stimulation, and illumination. A Win32 library written in "C" has been developed that allows a single computer to control most experimental variables and thereby streamline experiment design and data analysis. No third party libraries were used other than the primitives exposed by the PCI card device drivers supplied by the manufactures. The library supports Dalsa DS-12-16K5H cameras via the Bitfow R2 framegrabber, and CardioCCD-SMQ "Little Joe" cameras manufactured by SciMeasure and sold by Redshirt Imaging. The software also requires a National Instruments 6602 counter/timer PCI card that is used to synchronize the cameras and stimulation. Single, dual, and triple camera configurations have been used in various studies, but all use the same base library which was designed to be adaptable to new configurations with minimal effort. Some configurations have unique features not described here.

3.2. Overview

Virtually all experiments require cardiac pacing induced by an external stimulator. The sinus node is the heart's natural pacemaker, and will provide periodic

beats if not overdriven by an external stimulus. By pacing the heart externally, the timing of excitation can be controlled. This allows a test stimulus to be applied at a desired point in the action potential.

Custom stimulators described in chapter 4 have been built that allow virtually any stimulus protocol. Three basic stimulus protocols are used so frequently that they have been included explicitly in the acquisition software described here. In the following discussion S1, S2 and S3 refer to separate stimuli, although they may be connected to the same electrode. The stimulators used with the software described here output a constant current when a TTL signal is high. Therefore, S1, S2, and S3 in the software being discussed presently refer to the control TTL pulses which are sent to the stimulators. S1 is usually used for pacing the heart. S2 and S3 are test pulses, such as defibrillation shocks. The basic sequences are S1, S1-S2, and S1-S2-S3 which are illustrated in figure 3.1.

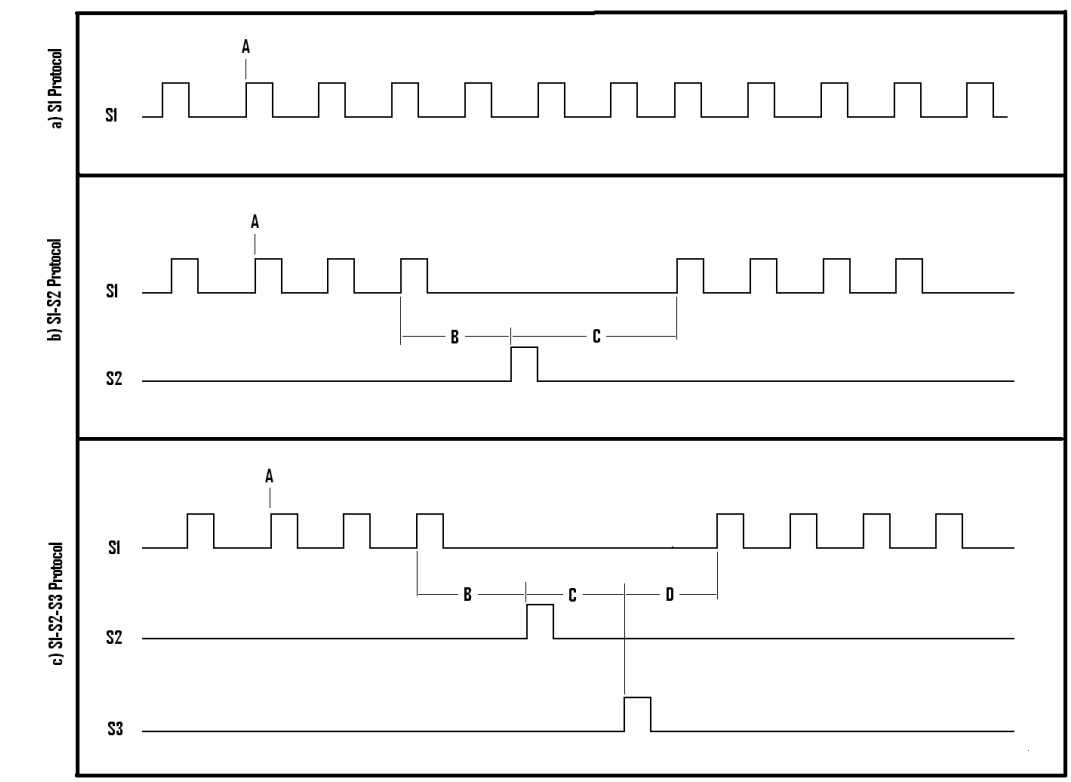

Figure 3.1. Timing diagrams for the S1, S1-S2, and S1-S2-S3 protocols. In all protocols, image acquisition begins with the upstroke of the first prepulse (discussed later) labeled A in each sequence. In the S1-S2 and S1-S2-S3 protocols, B indicates the S1-S2 delay. In the S1-S2 protocol, C represents the post S2 pause. In the S1-S2-S3 protocol, C represents the S2-S3 delay. In the S1-S2-S3 protocol, D represents the post S3 pause.

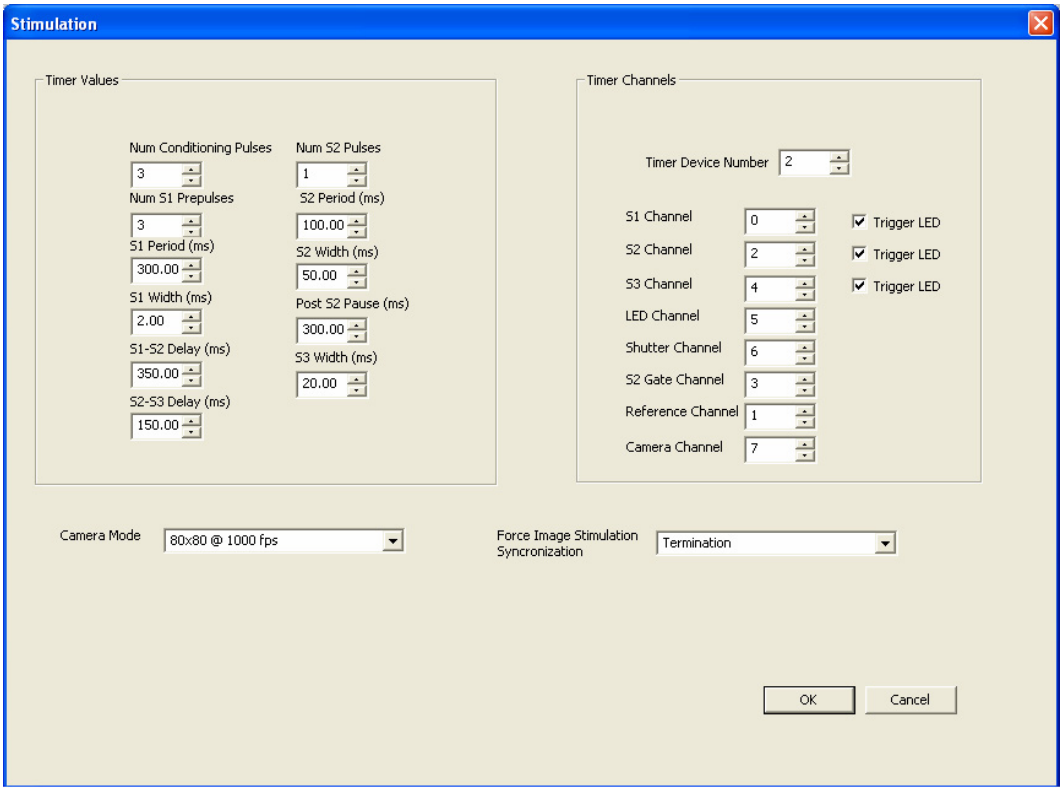

Figure 3.2. Stimulation Entry Window. This window allows stimulation information to be entered along with the camera/stimulus synchronization.

Figure 3.2 shows the stimulation window where the user enters the configuration and stimuli settings. This window appears when the ***Setup*** button is pressed in Panel E of figure 3.3. The ***Timer Channels*** group has twelve settings which specify which timer channels to use for specific stimuli and internal reference. ***Timer Device Number*** is the device number assigned by the National Instruments installation program for the 6602. The number assigned depends on what other cards are already assigned in the computer, and does not change once configured. The 6602 has eight 32-bit timer channels which may work independently or in concert with other timers or external signals. The ***S1 Channel***, ***S2 Channel*** and ***S3 Channel*** fields specify which TTL outputs should be connected to external stimulators. Each

of these fields has a ***Trigger LED*** checkbox next to it, which if selected will mirror the pulses from that channel on the ***LED Channel.*** The ***LED Channel*** specifies the channel dedicated to mirroring one or more stimulus channels. This is included to allow connection of an LED which can be placed in the field of view of a camera that will provide a record of the stimuli timing in an image sequence. In the software that previously existed, the stimulus-camera synchronization was inaccurate; however, this LED feature is no longer needed in the present software because the log file, discussed later, provides exact timing information. There is still a small uncertainty when using the Dalsa cameras, so this feature may still be useful and provides a visual representation of the stimuli timing, which is often helpful to the experimenter. Most of the configurations make use of one or more motorized shutters in the illumination system that are used to block laser or LED light except when images are being acquired and hence minimize photobleaching. The motorized shutters work by simple pulse-width-modulation and can be controlled directly from a timer channel. The ***Shutter Channel*** specifies which channel will be used. In some experiments, we use a large external stimulator for delivering defibrillation-strength shocks which requires a gating pulse in addition to a control pulse. The ***S2 Gate Channel*** specifies which channel will be used to provide the gating pulse. The ***Reference Channel*** is used internally by the software and does not need to be connected externally. The ***Camera Channel*** specifies which channel is used for camera triggering. The user may arbitrarily assign channels in the ***Timer Channels*** group, but each setting must be unique.

The ***Timer Values*** group shown in figure 3.2 has eleven fields which control the onset, duration, and number of various stimuli. All time intervals can be specified with a resolution of 10 μs. The times are entered in terms of ms with two decimal places allowed. If more than two decimals are entered, the value is rounded to the nearest 10 μs. ***Num Conditioning Pulses*** specifies how many conditioning S1 pulses to deliver in a stimulation sequence. Images are not recorded during this time. There is a slight interruption in the S1 period when the system switches from scanning mode to acquisition mode. Selecting a few conditioning pulses ensures the heart's pacing remains synchronized with S1 timing. No additional computer resources are used by increasing the number of conditioning pulses and the relative timing of the other stimuli are unaffected. ***Num Prepulses*** specifies how many prepulses to deliver. Prepulses are S1 pulses that are recorded. There is no disruption in the S1 signal between the last conditioning pulse and the first prepulse. Image acquisition begins simultaneously with the onset of the first prepulse. ***S1 Width, S2 Width, S3 Width, S1 Period, and S2 Period, and Num S2 Pulses*** are self-explanatory. ***S1-S2 Delay, S2-S3 Delay,*** and ***Post S2 Pause*** are illustrated in figure 3.1.

The ***Camera Mode*** combo-box shown in figure 3.2 specifies which of the various resolution and frame rate combinations of the Redshirt cameras is being used (this is not visible when using the Dalsa cameras). It is often desirable, especially when dealing with very short stimuli, to have a frame begin at the same instant a stimulus begins or ends. The various offsets could be adjusted to make this happen in most cases. For ease of use the ***Force Image Stimulus Synchronization*** combo-box was added. By selecting *Onset*, the system will adjust the S1-S2 interval slightly so

that the onset of the first S2 will coincide with the beginning of a frame. Alternatively, selecting *Termination* will cause the falling edge of the first S2 to coincide with the beginning of a frame. Selecting *None* makes no adjustments, and the default S1-S2 interval is used. If S3 is being used, the selections refer to the S3 pulse instead. The adjustments made to the offsets are noted in the log file.

Figure 3.3 shows the main window of a three-camera panoramic configuration. Panels E and F control global stimulus and camera parameters. The stimulus protocol generated for an image sequence is controlled by selecting the ***Use S1***, ***Use S2***, and ***Use S3*** buttons in panel E. If none of these three buttons is selected, image acquisition begins immediately when ***Acquire*** is pressed in panel F and the requested number of frames is recorded, but no S1 pulses will be sent during acquisition even if ***Start Pacing*** is selected.

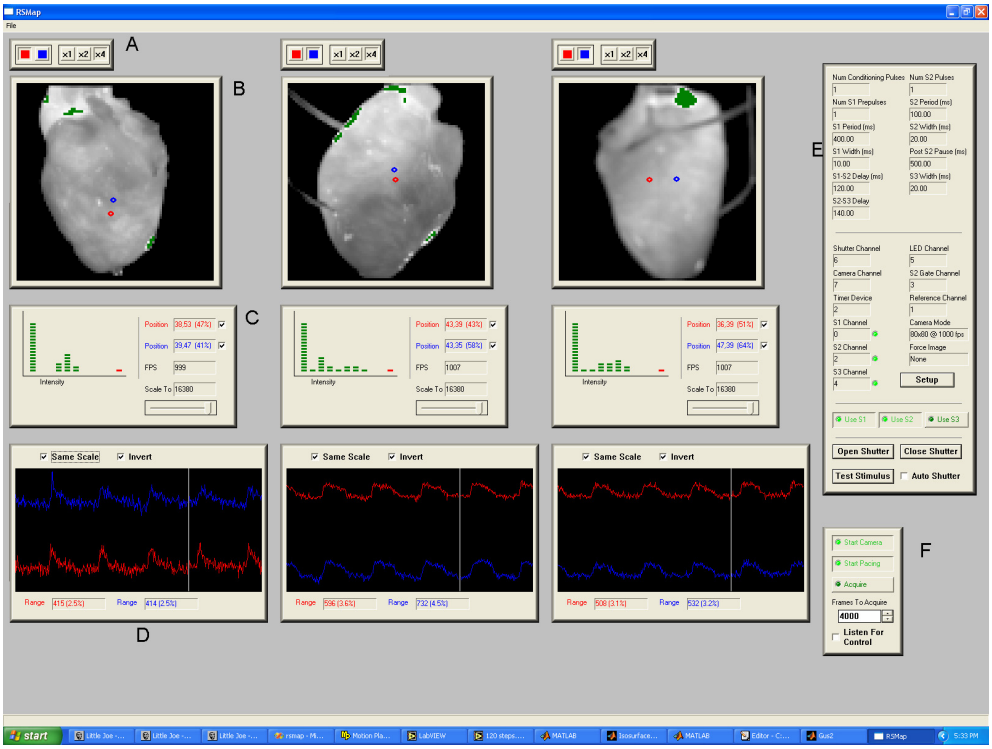

Figure 3.3. Panoramic three-camera main display. Four panels (A-D) are duplicated for each camera. Panels E and F provide stimulus and camera control.

Pressing ***Start Camera*** will start the camera(s) and begin displaying reduced frame-rate images, as well as other information discussed shortly. No information is recorded by pressing ***Start Camera,*** it is for viewing only. Pressing ***Start Pacing*** begins pacing using the parameters entered in the timing values for S1. The ***Acquire*** button initiates image acquisition of the number of frames specified in the ***Frames To Acquire*** field. It also initiates whatever stimulus sequence has been specified. When the ***Listen For Control*** checkbox is selected, an external Labview program, running on the same computer or remotely, can send image requests. This is used in the panoramic system to allow automated single image acquisition when rotating the heart. The naming of the 360 individual files required by the geometric

reconstruction as well as control of the rotation motor is entirely automated. The ***Open Shutter*** and ***Close Shutter*** buttons in panel E open and close the illumination shutter(s). If ***Auto Shutter*** is selected, the shutter(s) will close automatically when image acquisition is complete. However, the shutters will not open automatically when ***Acquire*** is pressed.

For each camera being used, there are four panels arranged vertically which provide data and display control for that camera. The four panels labeled A to D in figure 3.3 are for the first camera. Panel B shows a reduced-rate display of real-time data coming from the first camera. The images are scaled to 256 shades of gray which is the maximum number of shades common computer video hardware can display. All saturated pixels are shown as green in the images. There are two cursors that can be positioned by clicking the left mouse button. The real-time trace for these two data points, discussed shortly, is displayed in the graph.

Panel A shows magnification and cursor control. Three magnification buttons provide a spatial magnified view of the data. The available settings are different depending on the camera and mode. The two color buttons control which of two cursors (red or blue) that are displayed in the image display window is being positioned with the left mouse button.

Panel C shows a histogram of the intensity distribution for the image currently displayed. Ten ranges are established equally spaced over the possible range of intensity. An eleventh range is used for all pixels that are saturated. Since only the relative numbers are important, the histogram is scaled to the range with the largest population. The histogram is scaled such that the range with the largest count is 80%

of full scale. The one exception is the range dealing with saturation where a single saturated pixel will cause one red bar to be shown. Also on the histogram is a scaling slider. The cameras used are 12-bit or 14-bit; however, only 256 shades of gray can be displayed on a computer monitor. When the slider is at its rightmost position, the images are scaled linearly down to 256 shades of gray assuming that the maximum intensity is present. If the slider is moved to another value the scaling factor is changed which allows dimmer images to be seen more easily. This is also allows the heart to be viewed under lower illumination intensity during setup, which helps prevent photo-bleaching. The two ***Position*** fields in panel C give the spatial coordinates inside the image of the respective cursors as well as the signal strength at these points relative to full scale. The ***FPS*** field in panel C displays the current frame rate of the camera (frames per second). This value is a software measurement and is updated periodically. Some small fluctuation in this number is normal and does not indicate the frame rate of the camera is not fixed at the rate specified. The checkboxes in panel C adjacent to the ***Position*** fields control the display of the respective cursor. If a box is checked, the cursor is displayed in the display window and the real-time trace is displayed in the graph. If the box is not checked, the cursor and trace are not displayed.

Panel D is a graph of two intensity traces for the positions of the cursors in the display window. The ***Invert*** button in panel D inverts the signal of both traces. The ***Same Scale*** checkbox in panel D scales both traces to the same scale such that they can both be seen completely on the graph simultaneously. This is useful for viewing areas which have non-uniform illumination or poor signal due to poor perfusion or

some other reason. For each trace the ***Range*** field in panel D displays the difference in maximum and minimum intensity over the last graph update period as a percentage of overall range.

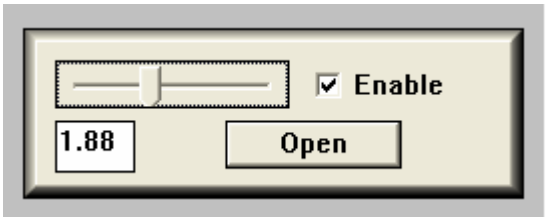

Figure 3.4. Laser control panel. Control panel for controlling Verdi laser.

For those configurations that use laser illumination instead of LEDs, control of the laser is integrated in the acquisition library. Figure 3.4 shows the laser control panel which works with a Verdi 5-watt 532 nm laser we often use for illumination. The ***Enable*** checkbox enables the panel. The slider and edit window allow the output to be set in watts. The ***Open*** button, whose text changes to *"Closed"* when open, cycles the internal laser shutter. This shutter is different than the mechanical shutters discussed earlier. The internal shutter is usually left open during an experiment.

As noted earlier, pressing the ***Acquire*** button initiates the stimulus and image sequences. When the acquisition is complete the user is prompted to enter a file name where the data will be saved. If the user cancels the entry, the data is discarded and the acquisition program returns to the state it was in just before ***Acquire*** was pressed. If a file name "*filename"* is entered, the user is next prompted for a comment. After a comment is entered, a log file will be created named "*filename.txt*" which contains all timing and stimulus information used as well as the laser power. If one of the ***Force Image Synchronization*** options was selected, the adjustment is included. The comment is recorded here also. The beginning frame and ending frame of each

stimulus is recorded. For example, an entry "*S2 4 Start Image 1221.2 End Image 1233.7*", means the fourth S2 started 20% in to frame 1221 and ended 70% in to frame 1233. Each stimulus has an entry in this format which is useful for data analysis. The actual image sequence data is stored in a file named "*filename.img*". This is a binary file of unsigned 16-bit integers. The unused high order bits for either the 14-bit or 12-bit cameras are set to zero. A final file named "*filename.hdr*" is created which contains information, such as pixel resolution, date, bit-depth, and comments, used by a custom MATLAB viewer. If more than one camera is used, a letter is appended to the image sequence data files to indicate which camera's data it contains. For example, if three cameras were used, three image files would be created—"*filename-A.img*", "*filename-B.img*", and "*filename-C.img*". Since the cameras are synchronized, the single log file applies to all image files. Three identical header files are created with names "*filename-A.hdr*", "*filename-B.hdr*", and "*filename-C.hdr*" to accommodate the MATLAB viewer.

CHAPTER IV

USB POWERED AND CONTROLLED ISOLATED CONSTANT-CURRENT PHYSIOLOGICAL STIMULATOR

Mark R. Holcomb[1], Robel Y. Bekele[1], Eduardo A. Lima[2], John P. Wikswo[1,2,3]

1. Department of Physics and Astronomy, Vanderbilt University
2. Department of Biomedical Engineering, Vanderbilt University
3. Department of Molecular Physiology and Biophysics, Vanderbilt University

Portions of this chapter will be submitted to *Review of Scientific Instruments*.

4.1. Abstract

We have developed a compact, isolated, physiological, constant-current stimulator that is Universal Serial Bus (USB) powered and controlled. The stimulator is designed to be used in *ex-vivo* cardiac experiments, but is suitable for a wide variety of settings. The cost and features compare very favorably with commercial stimulators usually used in research and student labs. In addition to being USB powered, other novel aspects of our stimulator include the ability to produce large currents up to 100 mA through a typical 1 kΩ load by using a single high-voltage DC-to-DC converter; user-specified variable period, magnitude, and duration of complex monophasic or biphasic sequences; and easy integration via hardware or software into existing experimental setups. We make use of an inexpensive control module comprised of a 16×2 LCD (Liquid Crystal Display), a PIC microcontroller,

and USB interface circuitry which connects to a custom PCB (Printed Circuit Board) containing the isolation and stimulation circuitry. The stimulator produces accurate stimuli in 100 μs and 100 μA increments with fast rise times. A high-speed micro-relay is used to produce biphasic sequences. There is no measurable leakage current when the stimulator is inactive. The high-voltage DC-to-DC converter generates 25 kHz noise which can be picked up near the stimulator with an oscilloscope or electrodes on the heart.

4.2. Introduction

Most cardiac electrophysiology studies require some form of electrical stimulation. The stimulator described here was specifically designed to be used in cardiac studies of isolated rabbit hearts, but is generally applicable to a large class of physiological stimulation requirements. Other custom stimulators have been described by Land *et al*. [1] which produce constant voltage, and Brasil *et al*. [2] which produce constant voltage and small constant currents, among others. Both are geared toward pacing or single pulse generation. A more sophisticated multiple channel stimulator by Cheever *et al*. [3] is used for skeletal muscle cardiac assist.

In the past we used commercial stimulators (Bloom) to produce constant current stimuli, hereafter called legacy stimulators. In the following discussion a load of 1 kΩ is assumed which is typical in our experiments on small hearts. The magnitude of the output current from our legacy stimulators is set by an analog control on the enclosure. The duration of the stimuli is controlled by external TTL pulses we generate using a PCI counter/timer card (6602, National Instruments). The

legacy stimulators have numerous shortcomings: (1) they require high-voltage batteries which need to be changed frequently and are difficult to obtain, (2) there is approximately 25 μA of leakage current when the stimulator is inactive, (3) the stimulators are unable to provide over 80 mA, (4) there are no means to change magnitude or polarity during a rapid stimulation sequence, and (5) modern commercially produced stimulators are not well suited for modification or optimization for specific applications.

We have built stimulators that address the above shortcomings as well as add other useful features. The USB stimulators have the following advantages: (1) elimination of batteries; all power comes from the host computer via a USB connection, (2) no measurable output when the stimulator is inactive, (3) 100 mA can be delivered to a typical load, (4) nearly any desired stimulus sequence with variable period, magnitude, and polarity can be generated, and (5) the output is isolated electrically from the computer and ground.

4.3. Stimulator Design

The stimulator uses a classic buffered voltage-controlled constant current source (CCS) with a few modifications. Figure 4.1 shows a schematic of the CCS. A set-point voltage provided by a 12-bit digital to analog converter (DAC) and a digital enable signal, both described shortly, control the set-point and activation of the CCS. In order to prevent any output from the stimulator when it is inactive, an unconventional op-amp power supply has been implemented. The digital enable signal is fed in the base of transistor Q1 that, when turned on, supplies power to the

op-amp (U1), and when off ensures zero output by effectively disconnecting the power. This unconventional op-amp supply does introduce rise time delays: we measured 5 μs and 15 μs rise times for currents of 10 mA and 100 mA, respectively. In cardiac experiments pulses generally are at least several milliseconds in duration; therefore this minor increase in rise time is an acceptable tradeoff to eliminate any leakage current. Except for the enable circuitry, this is a routine circuit and will not be analyzed further here.

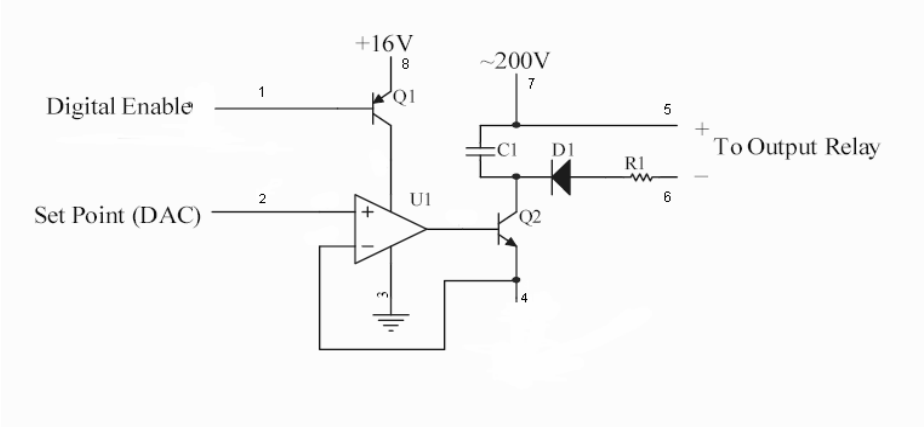

Figure 4.1. Schematic of the voltage controlled constant current source. An externally supplied set-point controls the output current, and a digital enable controls the onset and duration of the pulse. The components are Q1(2N3906), Q2(2N3440), U1(LM385N), D1(1N4004), R1(100 Ω 1/4 watt), and C1(250V 0.1 μF).

A USB controller module (MT-USB, Molex), shown in figure 4.2b and 4.2c, contains a 20 MHz, 40-pin PIC 18F452 microcontroller (Microchip), 16×2 LCD, and USB connector and circuitry that is used to communicate with the host personal computer (PC) and control the stimulator. The MT-USB has two 10-pin headers which are connected to our custom PCB, shown in figure 4.2d, that contains the isolation and stimulation circuitry. The pin connections are shown in figure 4.3. The PIC module uses the USB connection as a virtual serial port to communicate with the

host PC. The Windows driver for the virtual serial port is included in the standard Windows installation (since Windows 98 SE), but can be downloaded from FTDI (Future Technology Devices International) if needed. The PIC control program is written in C and compiled with the CCS PCWH version 3.236 compiler.

a) 

b) 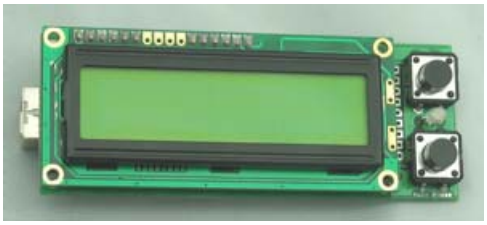

c) 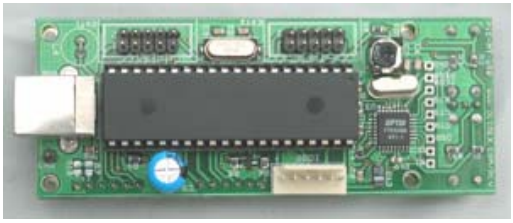

d) 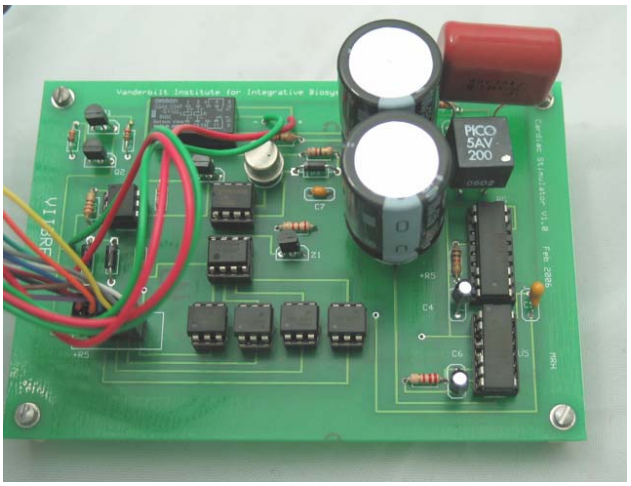

Figure 4.2. Stimulator components. (a) An external view of the front of the stimulator. (b) Front view of MT-USB module. (c) Back view of MT-USB module. (d) Custom PCB.

Figure 4.3 shows a schematic of the custom PCB. The CCS shown in figure 4.1 is shown as a block labeled CCS in the schematic. The PIC module, and therefore the host PC, is electrically isolated from the stimulation circuitry. The 5V supply

provided by the USB powers three DC-to-DC converters which provide power isolation and produce voltages of 5V, 12V, and 200V (U4, U5, and U10, respectively). Four digital lines from the PIC control the DAC (U2) by four-wire SPI (Serial Peripheral Interface), and are isolated by optoisolators (U6-U9). By isolating the stimulator from the host PC by either optical or electrical means, the chance of electrical interference, ground loops, or feedback of a potentially damaging voltage to the PC or experimenter is significantly reduced. In the following discussion, "local" refers to the stimulation circuitry side of isolation, and "remote" refers to the PIC/PC side of the isolation.

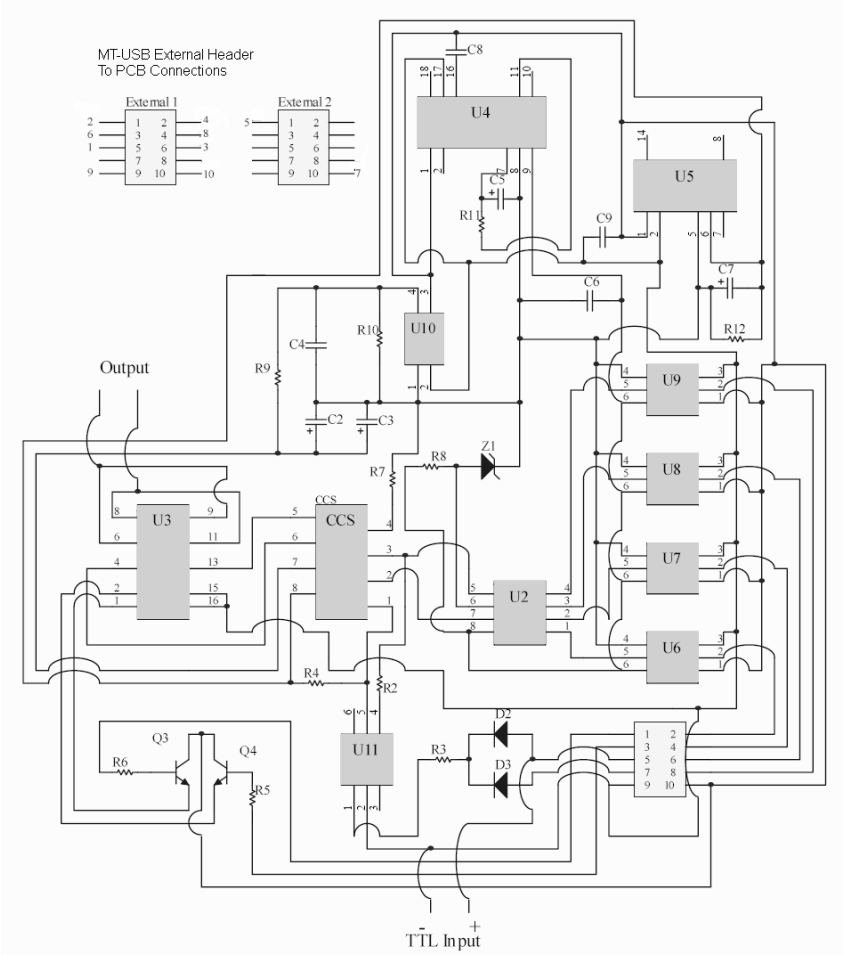

Figure 4.3. Stimulator schematic. The constant current source with parts list shown in figure 4.1 is shown as a device labeled CCS. A parts list of the remaining components is given in section 4.7.

The DC-to-DC converters all require a minimum load. The 5V components, which are always on, consume enough current to provide an adequate load for the 5V converter. The 12V converter is used to power the op-amp in the CCS. The op-amp is only active when the stimulator is enabled, so a 57 kΩ (R12) resistor is placed in parallel with the 12V converter which gives a minimum load of 5 mA. The 200V converter has a maximum output of 6.6 mA. It also requires a 10% minimum load at all times. A 247 kΩ (R10) resistor is placed in parallel with the converter to ensure

the minimum load, and a 47 KΩ (R9) resistor is placed in series with the two 100 μF capacitors (C2,C3) being charged. This ensures a maximum current draw that is below the 6.6 mA maximum. An advantage of the minimum load resistor is the rapid capacitor discharge (τ = 49 s) when the stimulator is disconnected from the USB.

The USB 2.0 specification states that a maximum of 500 mA may be drawn by a connected device. The maximum current drawn when the stimulator is connected to the USB connector is approximately 400 mA, which is well below the maximum. This is the peak current when the stimulator is first connected; the steady-state current is about 300 mA.

The output polarity is controlled by a latching micro-relay (U3). Since the relay control pins are isolated from the inputs and outputs, the relay is switched directly by two output pins on the PIC and the remote 5 V supply. The digital outputs of the PIC are connected through 1 kΩ resistors (R5,R6) to the bases of two NPN transistors (Q3,Q4). The transistor reduces the required source current from the PIC as well as protects the digital outputs from the back-emf of the relay. The specifications state the relay has a maximum switching time of 5 ms with 3.3 ms being typical. The software is designed to ensure that the relay is never switched during a pulse, only between pulses.

Rather than try to achieve output accuracy by selecting expensive precision components, we chose a software calibration instead. The DAC voltage reference and sense resistor (R_S) are the components which fundamentally determine the precision of the output. Calibration information is stored in the PIC's EEPROM. The two calibration values are set via software command and are retained indefinitely.

The first calibration value (C_1) is a calculated value that is a function of R_S and DAC voltage reference. To arrive at this value the two components are measured with a DMM (Digital Multi-Meter) after stimulator construction. The second calibration value (C_2) is an offset value which compensates for the DAC's small offset voltage. This offset is the primary source of an approximately 0.12 mA current pulse that occurs when the stimulator is set to zero. Therefore, accurate stimuli begin at 0.2 mA even though 0.0 mA and 0.1 mA settings are accepted. This offset has no affect on leakage when the stimulator is not producing a pulse. The two calibration values are sent to the stimulator with a text command which causes them to be written to EEPROM. The PIC calculates the DAC setting using the two calibration values as shown in Equation 4.1.

$$\text{DAC Setting} = \frac{(4.095)(I_{req})(R_s)}{2V_{ref}} - C_2 = C_1 I_{req} - C_2 \qquad (4.1)$$

Where I_{req} is in mA, and V_{ref} is in Volts, and R_s in in Ohms. If the DAC setting is calculated to be less than zero, then it is set to zero. By measuring the voltage reference and sense resistor after construction, an approximate value for C_1 can be obtained. By measuring the output of the DAC when the output is set to zero gives an approximate value of C_2. The calibration values can then be fine-tuned by direct output measurement as described shortly.

The 12-bit DAC does introduce small errors due to quantization, especially at low currents. Other factors such as DAC non-linearity and non-ideal op-amp behavior cause errors to a lesser extent. Using a FLUKE 75 DMM, we measured the current through a 2-watt 1 kΩ (993 Ω measured) resistor for stimulator settings of 0.2

mA to 1.0 mA in 0.1mA increments, and then in larger increments. The results are shown in table 4.1.

Table 4.1. Requested and measured small currents

Requested Current (mA)	0.2	0.3	0.4	0.5	0.6	0.7	0.8	0.9	1.0	2.0	3.0	4.0	5.0	10.0
Measured Current (mA)	0.20	0.31	0.41	0.51	0.62	0.69	0.79	0.90	1.00	1.98	3.00	3.99	5.01	10.01
Percent Error	0.0	-3.3	-2.5	-2.0	-3.3	1.4	1.3	0.0	0.0	1.0	0.0	0.2	-0.2	-0.1

The capacitors have insufficient charge to maintain larger currents for a second or longer as is required to obtain stable measurements with a DMM. For larger currents the voltage amplitude of 50 ms pulses were measure across the same 1 kΩ resistor using an oscilloscope (TDS5034B, Tektronix) with a differential probe (DP-25, AMEC Instruments). The results are shown in table 4.2.

Table 4.2. Requested and measured large currents.

Requested Current (mA)	20.0	30.0	40.0	50.0	60.0	70.0	80.0	90.0	100.0
Calculated Current (mA)	20.1	29.8	39.5	50.0	59.6	70.1	79.8	89.4	99.1
Percent Error	-0.5	0.7	1.3	0.0	0.7	-0.1	0.3	0.7	0.9

In order to make the stimulator as versatile as possible, all communication is accomplished via text commands, which offer a variety of advantages. For example, LabVIEW, MATLAB, Excel, or any other program that can write to a serial port can control the stimulator without the need for specialized libraries or software tools. The stimulator accepts currents in tenths of mA and durations in tenths of ms.

Descriptions of the nine acceptable commands with examples are included in the supplementary material. One example sequence:

```
output=-10.1
fire=5
```

The first command sets the output to -10.1 mA. The second command generates a 5 ms pulse. This is an example of *Manual* mode, which is one of the modes discussed shortly.

The device has five modes of operation—*Compatibility, Manual, Wavetrain, Enhanced and Standalone*. In *Compatibility* mode the stimulator outputs a constant current for the duration of an externally-supplied TTL pulse. For most of our experiments it is desirable to have the onset and termination of the stimulus synchronized with an external counter/timer that also controls camera timing. Driving both stimulators and cameras by the same clock improves experiment design and data analysis. For example, with our custom software we can specify for the onset or termination of a stimulus to coincide with the beginning or end of the acquisition of a camera frame. This mimics the functionality of the legacy stimulators discussed earlier except our devices are digitally controlled.

Manual mode is similar to *Compatibility* mode, except a software command from the host computer instructs the PIC to generate a single TTL pulse of a specified duration to drive the stimulator. No external TTL pulse is required.

In *Wavetrain* mode the stimulator can output stimuli with fixed frequency, duration, and amplitude. The wavetrain is initiated via software command from the host PC and, as in *Manual* mode, no external TTL pulse is required. Figure 4.4a

shows an oscilloscope trace of a wavetrain, and figure 4.4b shows the utility program used to control the stimulator.

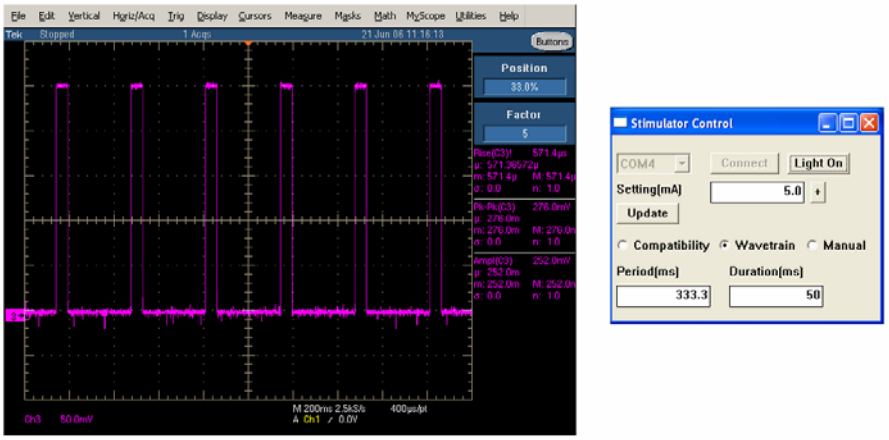

a) b)

Figure 4.4. Example of *Wavetrain* mode. (a) 3 Hz, 50 ms duration, +5.0 mA wavetrain as measured with an oscilloscope (TDS5034B, Tektronix) with a 20× differential probe (DP-25, AMEC Instruments) across a 1 kΩ resistor (b) The user interface for a utility program that can be used to control the stimulator in *Compatibility*, *Wavetrain*, and *Manual* modes.

Enhanced mode is specialized for our purposes and adds the ability to change the magnitude, polarity, period, and duration during a rapid stimulation sequence. *Enhanced* mode, as we use it, accepts TTL pulses from the 6602 counter/timer card that control the onset and duration of the individual stimuli exactly as they are in *Compatibility* mode. Using a text command, the host computer uploads the magnitudes and polarities for the stimulation sequence to the stimulator before the sequence begins. When the stimulator detects the falling edge of an incoming TTL pulse it loads the next set-point and changes the relay state if needed. This process continues for each entry in the list. In principle it is possible to mimic this behavior using the *Manual* or *Compatibility* modes by having the host computer change the

set-point at controlled times. However, our host computer is heavily taxed by acquiring images from as many as three high-speed cameras as well as controlling the 6602; the *Enhanced* mode eliminates an additional load on the host. Figure 4.5a gives an example of an *Enhanced* mode stimulation sequence which spells "VU" in constant current pulses, and figure 4.5b shows the control program which is integrated in our acquisition system discussed in chapter 2.

Standalone mode has the same functionality as *Enhanced* mode, but does not require external TTL pulses because the PIC generates all control pulses in this mode. The sequence is initiated with a software command, but there is an option to trigger a sequence with a single external TTL pulse. Due to limitations of the PIC architecture, *Standalone* mode has stimulus onset timing errors on the order of 10 μs to 50 μs depending on the sequence.

National Instruments makes several pattern I/O cards which are capable of outputting variable period and duration waveforms similar to our outputs with the 6602 in the *Enhanced* mode; however, they are more expensive and consume large amounts of computer memory. For our relatively long periods, at least 30 ms, a technique that uses a combination of the 6602's internal functionality and a Windows multimedia high-resolution timer callback allows the 6602 to output variable period and duration pulses while remaining exactly synchronized to the master clock on the 6602—the accuracy of the pulses is not dependent on the absolute accuracy of the Windows timer

a) b)

Figure 4.5. Example of an enhanced mode stimulation sequence. (a) The letters "VU" spelled with constant current pulses measured on an oscilloscope (TDS5034B, Tektronix) with a differential probe (DP-25, AMEC Instruments) across a 1kΩ resistor. (b) The user interface of the control program where the delay, duration, magnitude, and polarity of each stimuli are entered. The values shown were used to generate the oscilloscope trace shown in (a).

We often use multiple stimulators with the cameras which all need to be synchronized to a master clock. For these reasons we use *Enhanced* mode instead of *Standalone* mode. *Standalone* mode is included for completeness and possible future use in other types of experiments. Integrating control of the stimulators into our image acquisition software as we have done with *Enhanced* mode has the additional benefit of allowing a log of all stimulus information to be written to disk along with each image capture sequence which reduces the work-load on the experimenter.

4.4. Discussion

The total cost in parts including the custom PCBs is approximately $200, making this stimulator an attractive device for use in either research or student labs. The 6602, approximately $500, is required for operating the stimulator in *Enhanced*

mode and for synchronization with high-speed CCD cameras. Similar stimulators from a prominent commercial vendor range from approximately $1,000 with functionality similar to what we have termed *Compatibility* and *Wavetrain* modes, to over $6,000 for one that offers features similar to *Enhanced* and *Standalone* modes, although only to 10 mA. Neither of these options is USB powered. This does not imply that the stimulators described here are equivalent to, or are suitable replacements for, any particular commercial stimulator. Commercial stimulators may have desired features that our USB stimulators lack such as multiple channels and continuous waveforms. However, the comparison is useful to put the cost and functionality into context. Our designs have not been certified by a professional engineer.

The high-voltage DC-to-DC converters cost approximately $83. If only small currents were needed, a less expensive converter(s) could be used. The MT-USB module is designed to be a development/prototyping board, but we use it in the final product to simplify construction. The entire module including the PIC is approximately $43. We had the custom PCBs manufactured for $38 each.

The current capacity of the high-voltage DC-to-DC converter and USB port does limit the total amount of current in a continuous wavetrain, and the capacitor size is the limiting factor for a rapid stimulation sequence. Components were selected to meet our needs. For example, if we rely only on the charge stored in the capacitors, a 100 mA pulse can be maintained for 200 ms through a 1 kΩ load, or a 50 mA pulse can be maintained for 600 ms through a 1 kΩ load. This capacity far exceeds our requirements for stimulation of small hearts, but could be insufficient for

other types of experiments. The stimulators are also used for continuous pacing, with a typical value being 3 Hz, 0.4 mA to 10 mA pulses of 4 ms duration. Sufficient supply exists to easily maintain this type of continuous pacing indefinitely. The high-voltage DC-to-DC converter generates 25 kHz noise which can be picked up near the stimulator with an oscilloscope or electrodes on the heart. The RMS output is negligible, but this noise could be a significant problem when making electrode measurements.

If more accuracy were required, a larger sense resistor could be used for smaller currents. A second relay similar to the output relay could be used to switch between the two sense resistors which would provide two scales. For example, a 330 Ω resistor for a 0 to 10 mA range and the present 33 Ω resistor for a 10 mA to 100 mA range would allow two scales..

This work was supported in part by National Institutes of Health (R01-HL58241), and the Vanderbilt Institute for Integrated Biosystems Research and Education (VIIBRE). We thank John Fellenstein for the design and fabrication of the enclosures.

4.5. References

1 Land B.R., Johnson B.R., Wyttenbach R.A., Hoy R.R., "Tools for Physiology Labs: Inexpensive Equipment for Physiological Stimulation". J Under Neurosci Edu. 3(1):A30-A35, 2004.

2 Brasil R.O., Leal-Cardoso J.H., "An optically coupled power stimulus isolation unit with high voltage and fast rise time output". Braz J Med Biol Res 32:767-771, 1999.

3 Cheever E.A., Thompson D.R., Cmolik B.L., Santamore W.P., George D.T., A versatile microprocessor-based multichannel stimulator for skeletal muscle cardiac assist. IEEE Trans Biomed Eng 45:56-67, 1998.

4.6. Command Summary

Commands are not case-sensitive. No blank spaces are allowed in commands. The following is a list of commands accepted by the stimulator:

calibration=

Function: Writes two calibration values to the PIC EEPROM. The two values are used to calculate the correct DAC setting for a particular set-point. The values are retained indefinitely and should not need to be changed unless components are replaced.

Syntax: calibration=n,n.nnnn

Returns: '0' if successful

Comments: The first value is an integer which is subtracted from the calculated DAC setting. This compensates for the small DAC offset. A typical value would be 4. The second value is a floating-point value which when multiplied by the requested current times 10 gives the DAC setting that will produce the requested current. A typical value would be 3.487.

$DAC = \frac{(4.095)(I_{req})(R_s)}{2V_{ref}} = C_1 I_{req} - C_2$, where C1 and C2 are the calibration values, I_{req} is the requested current in mA, and R_s is the sense resistor in ohms.

Example: *calibration=3.487,4*

calibration

Function: Returns the current two calibration values stored in EEPROM.

Syntax calibration

Returns: The current two calibration values stored in EEPROM terminated by '/r'.

enhanced=

Function: Sets the set-point values for a sequence of pulses.
Syntax: enhanced = [+,-]nnn.n,[+,-]nnn.n,[+,-]nnn.n, …
Returns: '0' if successful
Comments: If a sequence of n pulses is desired, n values will be included in this command. The current set-point will be set to the first value in the list. When a falling edge of an incoming TTL pulse is detected, the next value is loaded. When the end of the list is reached, the output is set to 0.0 mA. "Enhanced Ready" will be displayed on the LCD. When the sequence is complete "Enhanced Done" will be displayed on the LDC.
Example: *enhanced=2.3,4,-5,2.1*

lighton

Function: Turns the LCD backlite on.
Syntax lighton
Returns: '0' if successful.

lightoff

Function Turns the LCD backlite off
Syntax lightoff
Returns: '0' if successful

output=

Function: Sets the output magnitude and polarity of the simulator. To generate a pulse either an external TTL pulse or a software command, both discussed elsewhere in this document, is required.
Syntax: Output=[+,-]nnn.n
Returns: '0' if successful
Comments: The output is in mA and can be any number in the range of -100.0 mA to 100 mA. The decimal is optional. If more than one decimal place is included it will be rounded to the nearest 0.1 mA. The set-point will be displayed on the LCD.
Examples: *output=23.2*
Sets the output to 23.2 mA.
Output=-33
Sets the output to -33.0 mA

output

Function: Returns the current set-point in mA.
Syntax Output
Returns Text string of the current set-point in mA terminated by '/r'.

reset

Function: Causes the stimulator to reset to compatibility mode with a set-point of 0.0 mA.
Syntax reset
Returns: '0' if successful

wavetrain=

Function: Initiates a fixed period and duration wavetrain at the current set-point.
Syntax wavetrain=nnn.n,nnn.n
Returns: '0' if successful
Comments: Initiates a fixed period and duration wave-train at the current output set-point. This does not require an external TTL signal and the wave-train begins immediately. The period must be longer than duration. The set-point, duration, and period will be displayed on the LCD
Example: *wavetrain=300,10*

4.7 Stimulator Parts List

U1 Fairchild Semiconductor Optocoupler Transistor Output. 4N25. Digikey Part# 4N25FS-ND
U2 Texas Instruments Low Power 12-Bit Digital-To-Analog Converters. TLV5616CP. Digikey Part# 296-3041-5-ND
U3 Omron Low Signal Relay. G6AK-234P-ST-US-DC5 Digikey Part# Z749-ND
U4 Miniature 1W Isolated Regulated DC/DC Converter. Burr-Brown Products from Texas Instruments. DCR010505P Digikey Part# DCR010505P-ND
U5 Miniature, 1W Isolated Unregulated DC/DC Converter. Burr-Brown Products from Texas Instruments.DCP010512B Digikey Part# DCP010512BP-ND
U6 Optoplanar High-Speed Logic-To-Logic Optocouplers. Fairchild Semiconductor. 74OL6000 Digikey Part # 74OL6000-ND
U7 Optoplanar High-Speed Logic-To-Logic Optocouplers. Fairchild Semiconductor. 74OL6000 Digikey Part # 74OL6000-ND
U8 Optoplanar High-Speed Logic-To-Logic Optocouplers. Fairchild Semiconductor. 74OL6000 Digikey Part # 74OL6000-ND
U9 Optoplanar High-Speed Logic-To-Logic Optocouplers. Fairchild Semiconductor. 74OL6000 Digikey Part # 74OL6000-ND
U10 Pico Electronics 5V-200V Isolated dc-dc converter 5AV200
Z1 : Programmable Voltage Reference. STMicroelectronics. TL431ACZ Digikey Part# 497- 3035-5-ND
Q3 NPN Transistor 2N2222
Q4 NPN Transistor 2N2222
C1 350V 100µF Radial Capacitor Digikey Part# 493-1223-ND
C2 350V 100µF Radial Capacitor Digikey Part# 493-1223-ND
C4 1250V 0.1µF radial capacitor ECW-H12104JV. Digikey Part# P10494-ND
C5 1 uF 50V KS Radial Digikey Part# P993-ND

C7 1 uF 50V KS Radial Digikey Part# P993-ND
C6 2.2 µF 25 V 10% Digikey Part# 399-1339-ND
C8. 2.2 µF 25 V 10% Digikey Part# 399-1339-ND
C9 2.2 µF 25 V 10% Digikey Part# 399-1339-ND
R2 820 Ω ¼ Wt
R3 47 kΩ ¼ Wt
R4 8.2 kΩ ¼ Wt
R5 1kΩ ¼ W
R6 1kΩ ¼ W
R7 33 Ω ¼ W
R8 2.2 kΩ ¼ W
R9 47 kΩ ¼ W
R10 220kΩ ¼ W
R11 10kΩ ¼ W
R12 2.2 kΩ ¼ W
D2 1N4001
D3 1N4001

CHAPTER V

DUAL CAMERA IMAGING SYSTEM FOR CARDIAC STUDIES

Mark R. Holcomb[1], Veniamin Y. Sidorov[2], Marcella C. Woods[2], Jonathan M. Gilligan[3], and John P. Wikswo[1,2,4]

1. Department of Physics and Astronomy, Vanderbilt University, Nashville, TN
2. Department of Biomedical Engineering, Vanderbilt University, Nashville, TN
3. Department of Earth and Environmental Science, Vanderbilt University, Nashville, TN.
4. Department of Molecular Physiology and Biophysics, Vanderbilt University, Nashville, TN

Portions of this chapter were submitted for publication in *IEEE TBME*

5.1. Abstract

Fluorescence imaging allows the study of the electrodynamics of an isolated heart. Typically a single dye is used. By monitoring the intensity of the fluorescence, a dynamic quantity can be observed, *i.e.*, transmembrane potential (V_m) or intracellular calcium concentration $[Ca^{2+}]_i$. We describe a straightforward dual camera system which allows simultaneous measurement of these two dynamic quantities from the same region. An optional software camera calibration routine eliminates the need for precise camera alignment. The system allows for rapid setup and high spatial resolution and is generally applicable to any two-camera measurement.

5.2. Introduction

Fluorescence imaging has become the primary modality for studying the electrodynamics of isolated hearts. Typically a single dye is used, and by monitoring the intensity of the fluorescence, a dynamic quantity can be observed, *i.e.*, transmembrane potential (V_m) or intracellular calcium concentration $[Ca^{2+}]_i$. Ideally, both are viewed simultaneously [1]. We have designed a straightforward dual camera system which allows simultaneous measurement of these two dynamic quantities from the same region. Previously, dual photodiode arrays have been developed; however, these systems require precise alignment because of the small number of pixels [2,3]. In contrast, the dual CCD system described here allows for rapid setup and high spatial resolution and is generally applicable to any two-camera measurement. Other similar systems have been reported by Omichi et. al. [4], and Chuck et.al.[5].

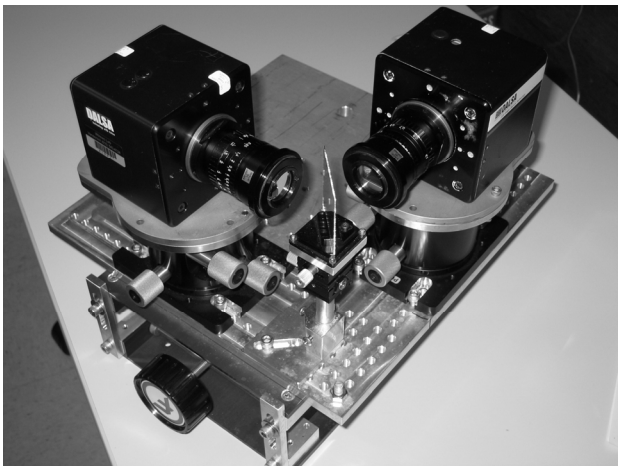

Figure 5.1. Dual camera system. Two cameras with lenses and filters are mounted on tilt and rotation stages. All elements are connected to a custom baseplate, which is mounted on a 20 cm × 20 cm labjack. The 45 degree mirror can be covered with a housing with circular ports.

5.3. Camera Hardware

Our dual camera system is shown in figure 5.1. The first optical element is a dichroic mirror (635 DCLP, Omega Optical), oriented at 45 degrees with respect to both cameras, that reflects the $[Ca^{2+}]_i$ signal and transmits the V_m signal. The V_m camera uses a 710 nm long pass filter (25 mm round 710AELP, Omega Optical), and the $[Ca^{2+}]_i$ camera uses a 585 $\pm$ 20 nm band pass filter (25 mm round 585AF40, Omega Optical). Both cameras have a lens (25 mm 1 inch format C-mount, Navitar) to which the filters are attached by a custom connector. Each camera (DS-12-16K5H 128×128 pixel 490 fps, Dalsa) sits upon a pair of custom mounting plates supported by a tilt and rotation stage (Newport P080N). A 6 mm thick aluminum base plate can accommodate various combinations of lenses and working distances. The entire system is mounted on a 20 cm × 20 cm lab jack that allows the height to be easily adjusted. A custom computer program controls all data acquisition, camera synchronization, laser illumination, and external stimuli.

5.4. Image Alignment

For maximum usefulness, the images recorded by the cameras should correlate spatially as well as temporally. The Newport stages allow quick and accurate mechanical alignment. Because the translation stages are expensive, as are the custom machined parts, we developed an alternative to precise mechanical alignment using a numerical algorithm that allows fine image alignment with only very coarse mechanical alignment of the cameras. A "rubber sheet transformation" similar to that described by Gonzalez et. al [6] is utilized.

Direct placement of fiducial reference points on the heart that are visible in both cameras would permit a traditional image registration, but this would interfere with the fluorescence data; therefore we chose a camera calibration technique which uses a stand-alone alignment grid of small points, each termed an alignment marker (AM). We used a backlit 35 mm photomask with a rectangular grid of translucent AMs containing 15 AMs in the horizontal direction and 11 AMs in the vertical direction. The procedure described shortly can be used with any size grid as long as it can be seen entirely by both cameras. The AMs were circular with a diameter of approximately 0.15 mm so that the width of each AM will occupy two or three pixels using the 12 mm × 12 mm field of view we used in our experiments. The exact size of the AMs is not critical. A photomask is convenient but not necessary; we have also used a simple grid made on a laser printer. The exact spacing of the AMs is not critical since both cameras view the same grid and only their relative positions are used. The calibration target is the same size as the desired field of view to ensure that the entire grid can be seen in focus by both cameras.

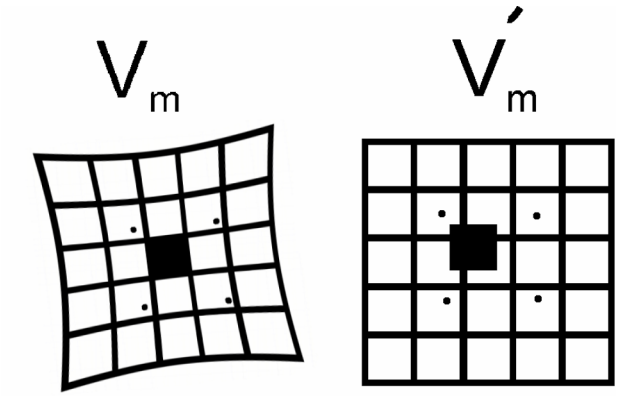

Figure 5.2. Pixel mapping. (a) V_m image (b) V_m' image. A single highlighted pixel in the V_m image with its four closest alignment points (a) is mapped to the image grid V_m' (b) using the corresponding alignment points in the $[Ca^{2+}]_i$ image.

The calibration procedure begins by each camera recording one image with the alignment grid in the field of view of both cameras. For each of the two images, we first identify the approximate location of each AM in an image. To do this automatically we sort all pixels by intensity while keeping their associated spatial coordinates. The brightest pixel is taken as the approximate location of one of the AMs. All pixels within a distance of five pixels from this pixel are removed from our search for other AMs, as the AM separation is about 10 pixels. With these nearby pixels removed from consideration, the brightest pixel remaining identifies the approximate location of another AM. We repeat this process of selection of the most intense pixel and removal of nearby pixels from the list until the approximate locations of all AMs are found.

Since the AMs are larger than one pixel, we next need to determine accurately the coordinates of the AM geometric centers. Because our AMs are less than two pixels in diameter we use the 3×3 set of pixels centered around each approximate AM location to determine a center-of-intensity of each AM given by

$$\vec{\mathbf{X}} = \frac{\sum_{i=x-1}^{x+1}\sum_{j=y-1}^{y+1} x_{ij}(I_{ij} - B)}{\sum_{i=x-1}^{x+1}\sum_{j=y-1}^{y+1} I_{ij}}, \tag{5.1}$$

where $\vec{\mathbf{X}}$ is the calculated coordinates of the geometric center of the AM, I_{ij} is the intensity of the ij^{th} pixel, and B is the average background intensity of the entire image. In the case where $(I_{ij}\text{-}B)$ gives a negative value, it is taken as zero. The approximate center of the AM, (x,y), in the previous step determines the limits of the summations. When the center-of-intensity has been computed for all AMs in both images, the resulting two tables of pairs of floating-point numbers listing the calculated geometric center of all

AMs in the alignment grid form the completed correspondence map. We term each entry in a table an alignment point.

Were we to assume that there were no distortions between the two images, we could use a least-squares fit with corresponding alignment points to compute a global offset vector and rotation. However, because of distortions from the lenses and differences in magnification, we find it is better to use the alignment point correspondence map to identify and correct for local distortions. For our experiments, we arbitrarily choose to adjust the V_m image and leave the $[Ca^{2+}]_i$ image unchanged, although it does not matter which image is adjusted. For each of the 16,384 pixels in the V_m image, we locate the closest four V_m alignment points. As illustrated in figure 5.2, we use our knowledge of the grid geometry to locate the corresponding four alignment points in the $[Ca^{2+}]_i$ image. We compute the position of a V_m pixel in relation to the $[Ca^{2+}]_i$ image by calculating the location $\vec{\mathbf{X}}'$ in V_m', the processed V_m image, that corresponds to the location (i,j) given by

$$\vec{\mathbf{X}}' = \frac{\sum_{k=1}^{4} \vec{\mathbf{r}}'_k - (\vec{\mathbf{r}}_k - \vec{\mathbf{X}}_{ij})}{4}, \tag{5.2}$$

where $\vec{\mathbf{X}}_{ij}$ is the original V_m pixel location, and $\vec{\mathbf{X}}'$ is the calculated corresponding point in the V_m' image. $\vec{\mathbf{r}}'_k$ and $\vec{\mathbf{r}}_k$ are alignment points in the $[Ca^{2+}]_i$ and V_m images respectively.

Most pixels from the V_m image do not correspond to only one pixel in the V_m' image. Because of distortions, the fractional pixels mapped into a particular pixel in V_m'

may not sum to unity. If n pixels from V_m partially map to pixel (i,j) in V_m' with percentages f_n, the intensity of the ij^{th} pixel in V_m' is given by

$$I_{ij}^{'} = \frac{\sum_{k=1}^{n} I_k f_k}{\sum_{k=1}^{n} f_k} \quad . \tag{5.3}$$

No processing is done on the $[Ca^{2+}]_i$ images other than to eliminate pixels that do not map to V_m'. At the end of this procedure a calibration file is saved that describes how to process the images from both cameras. An interactive program written in C allows the camera calibration to be accomplished very quickly. The same calibration file can be used repeatedly to process movies as long as the cameras are not moved with respect to each other.

5.5. Results

To demonstrate our technique, the cameras were deliberately misaligned. After completing the calibration procedure just described, we placed a test target in front of the cameras. Images (a) and (b) in figure 5.3 are unprocessed and show the test target (USAF 1951 Res Target, Edmund Optics) as seen from both cameras. Image (c) is the combination of the raw images before processing, with one set to 50% transparency. Note there are significant translational and rotational differences in the two images. Images (d) and (e) were processed using the calibration data. Image (f) shows the combined processed images, with the same one set to 50% transparency; note the significant improvement in this overlay in comparison with the one in (c). In tests in which the cameras were better aligned, the positions of features in the images typically

differ by no more than one pixel for the 128×128 pixel image. In the example shown in figure 5.3 the processed images differ by as much as two pixels. We believe that the large rotation in this example exposes the weakness of using only linear interpolation, although the results are still quite good.

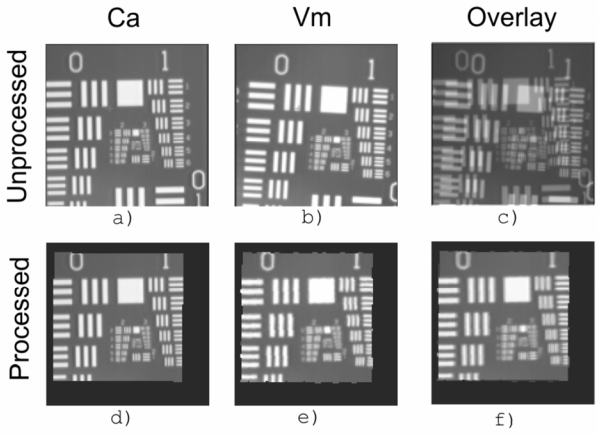

Figure 5.3. Demonstration of numerical alignment of two-camera images. (a) and (b) Unprocessed images from both cameras. (c) Overlay of intentionally misaligned, unprocessed images. (d) and (e) Processed images. (f) Overlay of the processed images. The field of view is approximately 12 mm × 12 mm

A disadvantage of the software calibration is that all pixels in the CCD cameras are not utilized since the aligned images can only represent the intersection of what is seen by both cameras. This effect can be seen as the black borders in the processed images d-f in figure 5.3. A second disadvantage is the calibration makes no allowance for surface curvature of the heart which could affect the mapping of a single point on the heart to the two planar images which were aligned using a planar array of AMs. For the small field of view we typically use, however, this is not a significant problem, but it could be accounted for by using a non-planar alignment grid in the calibration procedure.

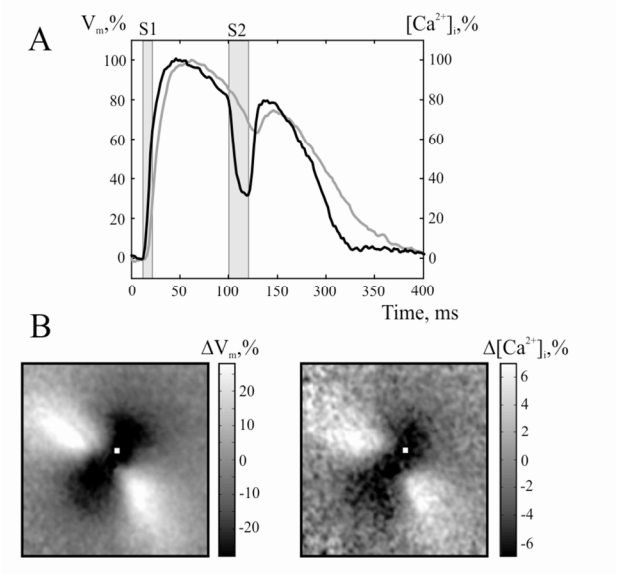

Figure 5.4. The voltage and calcium responses to anodal stimulation. The field of view is 12 mm × 12 mm. The S2 stimulus was 20 ms in duration and 20 mA in amplitude and was delivered at S1-S2 interval of 90 ms. The optical data were first preprocessed by applying a spatial 8 × 8 Gaussian filter and a 3-point mean temporal filter, then normalized on a pixel-by-pixel basis, and are presented as the percentage of highest change in fluorescence. A: Action potential (black trace) and calcium transient (gray trace) extracted from the same pixel (white square in B) at central hyperpolarized area. B: Voltage and calcium distributions at the end of S2. To display net voltage (ΔV_m) and calcium $[\Delta Ca^{2+}]_i$ displacements due to S2, the previous response was subtracted from S2 response.

The first experiments using this system were studies of V_m and $[Ca^{2+}]_i$ of a 12 mm × 12 mm area of the anterior left ventricle of a Langendorff-perfused rabbit heart. The calcium and voltage dyes used were Rhod-2 AM and RH-237, respectively (Invitrogen). The heart was prepared in a manner similar to what has been described previously [7]. Figure 5.4 shows the V_m and $[Ca^{2+}]_i$ response to a strong systolic stimulus (S2). The analysis of these data is beyond the scope of paper, but it does show the ability to distinguish the two signals. Briefly, it is well established that V_m leads $[Ca^{2+}]_i$ during

normal pacing (S1 stimulation) as shown; what is of interest in figure 5.4 is the response of the two signals upon termination of the S2 stimulus.

5.6. Discussion

This system can also be configured for different types of experiments. For example, it is an ideal setup for ratiometric imaging, in which only the filters would need to be changed [8]. We have also used this system with one low-resolution high-speed camera running at 5000 fps (26 ×26 pixels, CardioCCD-SMQ, Redshirt Imaging) and one high-spatial resolution camera (DS-12-16K5H 128 × 128 pixel 490 fps, Dalsa) in a field shock study[7]. In this case the heart was stained with only a voltage dye, and both cameras used the same long pass filters. The dichroic mirror was replaced with a partially silvered mirror which allowed both cameras to view the same activity.

By attaching a positive achroic lens (15 mm, Omega Optical) to the cubical mirror housing (NT56-265, Edmund, not shown in figure 5.1) such that the lens is now the first element in the system, we can magnify and narrow the field of view to be as small as 2 mm × 2 mm, which would be required to image, for example, a mouse heart. In adjusting the various parameters, we found that focusing the 25 mm lenses to infinity and adjusting the camera distance from the mirror-lens combination works best for controlling the field of view. Varying the distance between the entire system and the heart works best for adjusting focus. This configuration achieves a small field of view without losing a significant amount of light and preserves the shallow depth of field that is important in this type of imaging. This is essentially a tandem lens configuration which is common practice.

In conclusion, these simple configurations and techniques allow for both rapid experimental setup and high quality spatial correspondence between simultaneous images recorded by a pair of CCD cameras.

5.7. Acknowledgements

This work was supported in part by National Institutes of Health (R01-HL58241), and the Vanderbilt Institute for Integrated Biological Research and Education (VIIBRE).

5.8. References

1 Gray, R.A., Iyer, A., Bray, M.-A., Wikswo, J.P., "Voltage-calcium state-space dynamics during initiation of reentry". Heart Rhythm, vol. 3, no. 2, pp. 247-248, 2006.

2 Choi, B.-R., Salama, G., "Simultaneous maps of optical action potentials and calcium transients in guinea-pig hearts: mechanisms underlying concordant alternans". J. Physiol. (Lond.), vol. 529, pp. 171-188, 2000.

3 Efimov, I.R., Nikolski, V.P., and Salama, G., "Optical imaging of the heart". Circ. Res., vol. 95, no. 1, pp. 21-33, 2004.

4 Omichi, C., Lamp, S.T., Lin S.F., Yang, J., Baher, A., Zhou, S., Attin, M., Lee, M.H., Karagueuzian, H.S., Kogan, B., Qu, Z., Garfinkel, A., Chen, P.S., and Weiss, J.N., "Intracellular Ca dynamics in ventricular fibrillation". Am J Physiol Heart Circ Physiol 286 H1836, 2004.

5 Chuck, T., Meyers, K., France, D., Creazzo, T., Morley, G., "Transitions in the ventricular activation revealed by two-dimensional optical mapping". A Discov Mol Cell Evol Biol, pp 990, 2004.

6 Gonzalez &Woods, "Digital Image Processing". Addison-Wesley Publishing Company,pp 296, 1993.

7 Woods, M.C., "The Response of the Cardiac Bidomain to Electrical Stimulation". Doctoral dissertation, Nashville, TN: Vanderbilt University, pp. 109-135, 2005.

8 Knisley, S.B., Justice, R.K., Kong, W., and Johnson, P.L., “Ratiometry of transmembrane voltage-sensitive fluorescent dye emission in hearts”. Am. J. Physiol., vol. 279, no. 3, pp. 1421-1432, 2000.

CHAPTER VI

HIGH-RESOLUTION HIGH-SPEED PANORAMIC CARDIAC IMAGING SYSTEM

Dale W. Evertson (In Memorial),[1] Mark R. Holcomb,[2] Matthew D.C. Eames,[3,4] Mark-Anthony P. Bray,[3,5] Veniamin Y. Sidorov,[3] Junkai Xu,[2] Holley Wingard,[1] Hana M. Dobrovolny,[6,7] Marcella C. Woods,[3] Daniel J. Gauthier,[6,8] and John P. Wikswo[2,3,9]

1. Department of Mechanical Engineering, Vanderbilt University
2. Department of Physics, and Astronomy, Vanderbilt University
3. Department of Biomedical Engineering, Vanderbilt University
4. Present Address, Department of Biomedical Engineering, University of Virginia
5. Present Address, Division of Engineering and Applied Sciences, Harvard University
6. Department of Physics, Duke University
7. Center for Nonlinear and Complex Systems, Duke University
8. Department of Biomedical Engineering, Duke University
9. Department of Molecular Physiology and Biophysics, Vanderbilt University

Portions of this manuscript are under review for publication in *IEEE TBME*

6.1. Abstract

A panoramic cardiac imaging system consisting of three high-speed CCD cameras has been developed to image the surface electrophysiology of a rabbit heart via fluorescence imaging using a voltage-sensitive dye. A robust, unique mechanical system was designed to accommodate the three cameras and to adapt to the requirements of future experiments. A unified computer interface was created for this application – a single computer controls all three CCD cameras, illumination, stimulation, and a stepping motor used to rotate the heart. The geometric reconstruction algorithms are adapted from

a previous cardiac imaging system. We demonstrate the system by imaging a polymorphic cardiac tachycardia.

6.2. Introduction

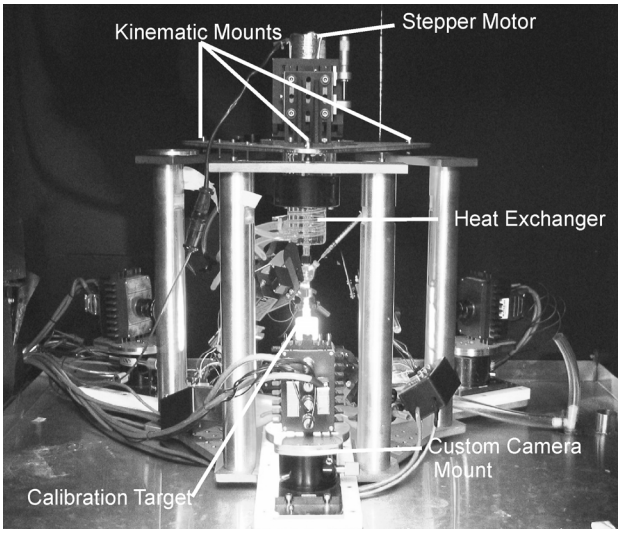

Figure 6.1. System as seen from outside the Faraday cage through one of three sets of double doors

Cardiac tissue is an electrically excitable medium that can support either normal or abnormal patterns of activation. The initiation of activation and its subsequent propagation bears significant importance in the design of pacemakers, defibrillators, and antiarrhythmic drugs. By studying the cardiac electrophysiology of rabbit hearts, researchers may extrapolate the acquired data and apply it to human heart electrophysiology. Panoramic cardiac optical mapping using a voltage-sensitive dye to report the time-dependence of the transmembrane potential has been used previously to record and analyze cardiac electrical activity. This technique, described in preliminary

form by Lin *et al.* [1] and further expanded by Bray *et al*. [2], involves (1) imaging an excised, Langendorf-perfused rabbit heart from three points of view, (2) numerically reconstructing the heart surface features, and (3) texture-mapping the acquired fluorescence images of the heart's electrical activity onto the virtual surface. The result is a movie of the electrical activity across the entire 3-dimensional epicardial surface. Subsequently, panoramic systems for studying hearts have been developed by Kay *et al.* [4], and Qu *et al*. [5].

A major engineering compromise in the design of our previous system [1,2] was the trade-off between the spatial and temporal resolution of the data acquisition. In the previous design, one high-speed charge-coupled-device (CCD) camera and two mirrors were used to image the entire surface of the heart. Therefore, all three points-of-view (POV) of the heart were recorded in a single image. The present paper describes a system, shown in figure 6.1, that uses three high-speed CCD cameras spaced 120 degrees around the heart on the horizontal plane. While additional considerations are required in a design in which three cameras are used (camera synchronization, user interface, etc.), with one camera assigned to each of the three POVs of the heart, the present system will image the epicardial surface with a greater number of pixels and will achieve better pixel resolution because each camera can be independently positioned.

In addition to improvements in the imaging modality, the system takes advantage of recent innovations in solid-state illumination. We excite the voltage-sensitive dye with an illumination system comprised of six high-intensity green LEDs coupled to CPU heat sinks and fans rather than the laser illumination used in the single-camera system. The entire LED illumination system, including power supplies, costs approximately $2,000,

making it much more cost-effective than the $50,000 Coherent Verdi laser used in the previous system.

In addition to improving the resolution of the images acquired with the present setup, we have implemented a new kinematic mechanical system to improve accuracy and usability and to reduce the need for camera recalibration. This new configuration was required to accommodate the additional cameras, but also addressed many of the shortcomings of the previous system. These improvements include (1) an integral system base plate to support all components, (2) a kinematic mount for supporting the heart, so that the heart can be sutured into place away from the CCD cameras and then mounted quickly in the camera system, and (3) three arrays of tapped holes near the heart for attaching experimental equipment that may be needed in future experiments. These mechanical improvements start with the system's base plate, which supports all the imaging components and the experimental heart. CAD files for all system components are available at (URL to be determined).

6.3. Experimental Setup

6.3.1. Base Plate

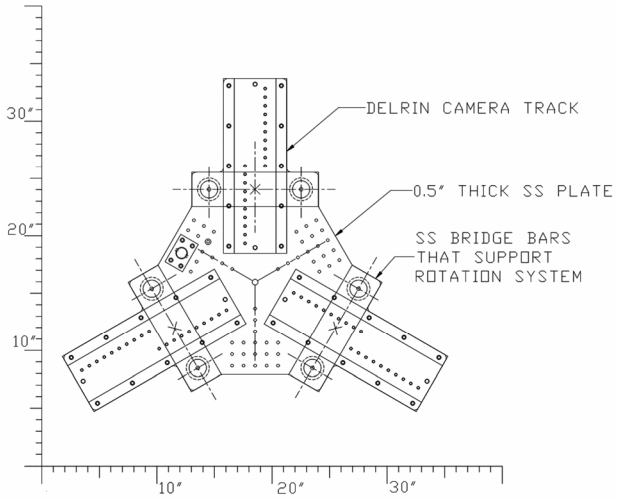

Figure 6.2. Top view of the system base plate. The base plate supports the three CCD cameras on radial tracks and the illumination system. The heart and perfusion system are supported by six vertical posts spanned by three horizontal bars.

A 13-mm-thick, stainless steel base plate is the mechanical centerpiece of the imaging system. It is supported by three neoprene vibration-isolation mounts (Part #64865K94, McMaster-Carr), which serve the secondary function of suspending the system above any fluids that may have accumulated in the stainless steel drip pan on which it rests. Figure 6.2 shows a top view of the base plate layout. Its primary function is to allow accurate and precise positioning of the system's three cameras, which are discussed later.

As shown in figure 6.2, three Delrin® tracks are attached to the base plate. The tracks allow easy adjustment of the distance between each of the system's three cameras

and the heart, which is suspended from an adjustable and locking perfusion system at the center of the base plate. Each track is machined to fit a stainless steel slider plate, which also serves as an adapter plate for the camera mount; the slider may be fastened to the track once it is positioned to the required heart-to-camera distance to lock the camera locations. Figure 6.3 shows one of the camera assemblies and track from the perspective of the heart.

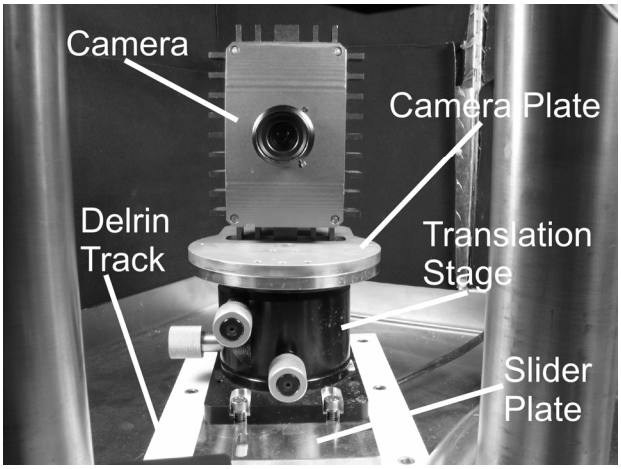

Figure 6.3. One of the three cameras and its mount on the Delrin track, as seen from the perspective of the heart.

Figure 6.2 also shows that on both sides of each track are 5.1-cm-diameter machined flats centered on threaded holes that allow the attachment of perpendicular support rods. Spanning each pair of supports is a 13-mm-thick rectangular section of aluminum (shown with a dotted line), which forms the basis of the kinematic mount system, described shortly. The aluminum plates support a removable triangular plate that in turn supports the heat exchanger on which the heart is secured. The remaining surface of the base plate is perforated with grids of 1/4-20 threaded holes on 1-inch centers,

including three lines of threaded holes extending radially away from the center of the base plate, for attaching the LED illumination system (also discussed later), and any necessary experimental devices.

6.3.2. Perfusion System

The pumps and heat exchangers used in this experimental setup are identical to or are updated versions of those used in our previous system [1,2]. For the purposes of this paper, the key function of the perfusion system is to maintain the viability of the heart *ex vivo* while the experiment is performed and data recorded. The perfusion system is also used to administer the voltage-sensitive fluorescent dye, di-4-ANEPPS, (Molecular Probes Inc) to the cardiac tissue.

6.3.3. Illumination

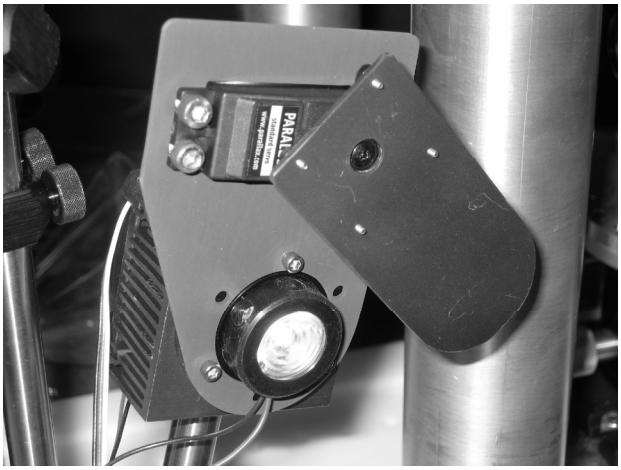

Figure 6.4. An LED mounted on CPU heat sink and fan with a motorized shutter.

High-power LEDs (LXHL-LM5C, Luxeon) provide green light for dye activation. Because heating of the junction may affect light output, we mounted the LEDs on CPU

heat sinks and fans (SKU 275016, COMPUSA), similar to that shown in figure 6.4. A custom bracket secures a lens (LXHL-NX05, Luxeon) to the front surface of each LED.

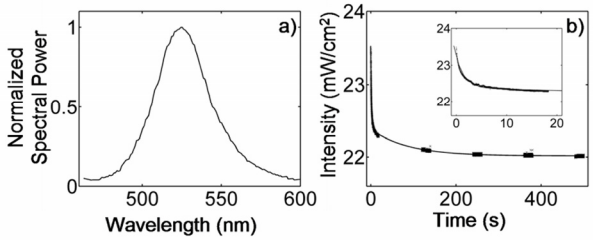

Figure 6.5. a) Emission spectrum of the green Luxeon Star/V LED (LXHL-LM5C). The spectrum peaks at ~525 nm. b) Temporal evolution of the intensity from the green Star/V LED. The data is fit to a biexponential with a slow time constant of 85.2 s and a fast time constant of 1.7 s. The intensity drops by about 7% from the initial turn-on to the eventual steady-state value. Data was taken with a silicon photodetector (New Focus, model #2031)

The emission spectrum supplied by the LED manufacturer is shown in figure 6.5a. The peak of the emission spectrum (~525 nm) is very close to the wavelength of the frequency-doubled Nd:YAG laser (532 nm) used in the previous study. Furthermore, the spectral bandwidth of the light is sufficiently narrow (~30 nm) so that no additional spectral filter of the light is required.

The LEDs must not only provide enough intensity for the experiments, but also the intensity must remain stable over the course of the experiment. Figure 6.5b shows the temporal evolution of LED intensity when configured similar to that shown in figure 6.4. Note the intensity drops approximately 7% over several minutes before reaching a steady-state value. This change in intensity is large in comparison to the change in fluorescence expected when the tissue depolarizes. Thus, the LEDs must be on several minutes before data acquisition.

The voltage-sensitive dye activated by the LEDs is prone to photobleaching if overexposed to light. This, along with the long LED stabilization time, led us to design a shutter system, also shown in figure 6.4. The shutter system allows the LEDs to remain on continuously at steady-state intensity while preventing photobleaching by only exposing the heart to light during data acquisition. The shutter motors (Standard Servo Stock#: 900-00005, Parallax) are controlled by simple pulse-width modulation and open and close automatically before and after data acquisition. The anodized motor mount and shutter are custom made.

Six LED assemblies are arranged about the heart centered on the faces of a virtual cube aligned with its diagonal (1 1 1) axis oriented along the vertical axis of the system. Thus, the LEDs are situated around the heart with three above and three below, in which the lower triad of LEDs is staggered by 60° around the vertical axis with respect to the upper LED triad.

To provide clamping arms for securing each heat sink / LED / lens assembly, 10-cm-long, 13-mm-diameter posts (SP-4, Newport) are secured to the heat sinks via 1/4-20 cap screws passed through the central gaps in the heat sink cooling fins and threaded into the end of the posts. Bisecting the angles between the cameras are three vertically-mounted 30-cm-long posts (SP-12, Newport) that have been secured to the base plate with 1/4-20 set screws. Two LED assemblies are attached to each 30-cm-long post by way of an angle post bracket (CA-2, Newport). By attaching one LED assembly angled upwards and the second angled downwards on each 30-cm-long post, the desired LED geometry can be achieved. The distance between the LED and heart can be adjusted by moving the 30-cm-long posts to a different radial 1/4-20 tapped holes in the base plate.

The LEDs are powered by three dual-mode power supplies (E3610A, Agilent), each providing up to 700 mA to two LEDs wired in series which is the LED manufacturer's specified maximum current. An additional power supply (BOP 20-5M, Kepco) is used to power the heat sink fans with 12 VDC.

6.3.4. Cameras

This panoramic imaging system uses three synchronized, high frame rate, 14-bit, charge-coupled device (CCD) cameras (CardioCCD-SMQ, Redshirt Imaging) to image the electrical activity across the surface of a heart. Each camera is capable of recording up to 2000, 3000, and 5000 fps at resolutions of 80 × 80, 40 × 40, and 26 × 26 pixels, respectively. We also have an alternate configuration which uses 128 × 128 pixel cameras running at 490 fps (DS-12-16K5H, Dalsa). The camera choice for a given experiment depends on the phenomenon being studied. All cameras are controlled by a single personal computer (Precision 650, Dell) equipped with 2 GB of RAM. This is a vast improvement over our previous design, which used a single CCD camera with 128 × 64 pixels operating at 335 fps. By using three cameras, the total number of pixels has increased from 8,192 in the old system up to either 19,200 for the Redshirt configuration or 49,152 for the Dalsa configuration. In the original setup, approximately 60% of the pixels were used to image the heart. In contrast, for our first two experiments with the new system described here, pixel utilization was approximately 52%, but by using three cameras, a two-fold increase in useable pixels is achieved when using the Redshirt configuration, and a five-fold increase when using the Dalsa configuration. A 50% or 500% increase in temporal resolution is achieved when using the highest spatial

resolution of the Dalsa and Redshirt cameras, respectively. Using the Redshirt 26 × 26 pixels 5000 fps mode, a 1400% increase in temporal resolution can be achieved. We have acquired successfully 2-D whole heart fluorescence data with this resolution and frame rate [6]. Both camera configurations use 12-mm C-mount lenses (LM12JCM, Kowa).

Each of the three cameras in the new system may be independently positioned and directed at the target object; in addition to the custom sliders described above, the camera mounts (PO80N, Newport) shown in figure 6.3 allow adjustment of the pan, tilt, and roll of the camera. This allows optimization of the position of the heart in the field-of-view. Camera synchronization is achieved via external pulses generated by a PCI timer card (PCI-6602, National Instruments).

6.3.5. Rotation System

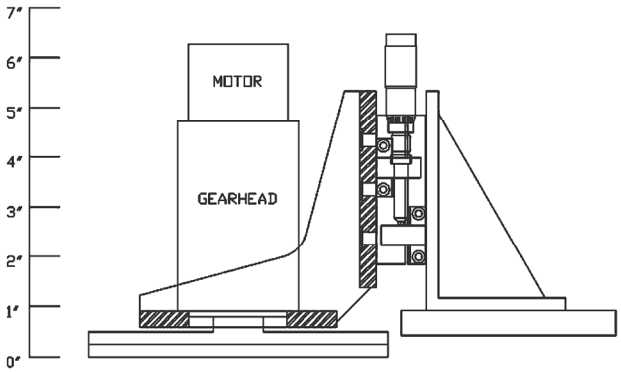

Figure 6.6. The Z-translation stage allows coarse and fine height adjustment of the experimental heart being imaged.

The heat exchanger in the perfusion system is suspended from a computer controlled stepping motor (S57-102-MO, Compumotor), connected to a 20:1 gearhead (PG60-020-T01, Bayside) providing precise angular positioning for the sequence of images necessary for creating the wire-frame reconstruction of the heart surface features. Figure 6.6 shows the motor and z-translation stage; it can also be seen in figure 6.1.

The stepping motor supporting the heat exchanger is attached, via a 90° angle bracket (360-90, Newport), to a vertically mounted translation stage with 25 mm of linear travel (423, Newport), as shown in figure 6.6. This permits accurate positioning of the heart in the field-of-view of the three cameras. The Newport translation stage is attached, via a second 90° angle bracket (EQ120-I, Newport), to the kinematically mounted triangular stainless steel plate. This plate has an array of holes drilled and tapped to allow the use of temporary mounts and stays in future experiments.

6.3.6. Kinematic Mount

The heat exchanger, to which the heart is secured, is held by a triangular plate that is supported above the base plate by a kinematic mount. As opposed to a mechanically-simple fastening solution, the kinematic design permits the triangular plate to be removed easily from the supports, enabling preparation of the heart for perfusion without obstruction by the imaging instrumentation. The plate can be placed in the same position with a high degree of precision and does not require any additional mechanical clamps or fasteners.

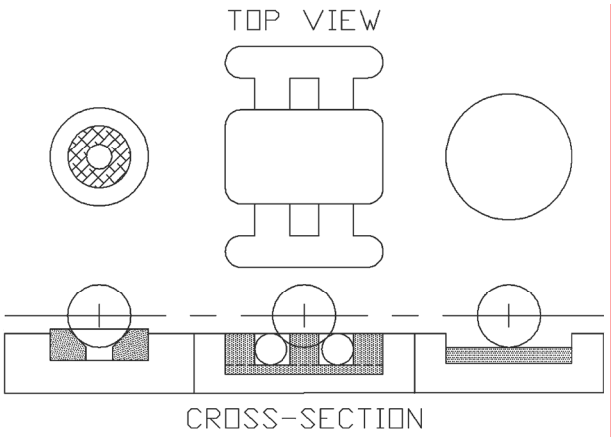

Figure 6.7. The three components of a kinematic mount (left to right) to restrict the six degrees of freedom of the plate: ball in cone--three degrees of restraint, ball on rods--two degrees, and ball on flat plate--one degree.

Each corner of the triangular plate is fitted with a precisely machined ball-and-post (Part #STB-26815, Reid Tool) which supports the triangular plate from three machined spot-faces. Attached to the posts protruding through to the top of the plate are lock-collars to prevent the ball-and-posts from dropping out of the triangular plate when removed from its supports while allowing the shoulder on the post above the ball to determine the height of the plate. The kinematic mounts can be seen in figure 6.1.

Three anodized aluminum rectangular plates span three pairs of vertical supports. Each plate has two machined spot-faces and corresponding counter bores for socket-head cap screws to ensure that the plates rest flat on the support posts. The third machined spot provides each of the three kinematic mounting points on which the machined ball-and-posts rest, described as follows [figure 6.7]:

(1) The first plate is machined to hold a hardened steel ring with a 45° bevel cut into the upper inside corner; the bevel forms a 90° angle with respect to the center of the resting ball-and-post. This removes lateral-translational freedom in the horizontal plane.

(2) A second plate is machined to fit two parallel hardened steel dowel pins such that their tangent surface form a 90° angle with respect to the center of the resting ball-and-post. By orienting the axis of the dowel pins towards the center of system, rotation in the azimuthal direction is prevented.

(3) The third plate is machined for a press fit of a hardened steel disk. This disk sets the height of the third corner of the triangular plate, thereby removing the final degree of freedom.

6.3.7. Enclosure

A custom-built aluminum Faraday cage (Duck Welding, Nashville) provides both electromagnetic isolation and a light-tight enclosure for the system. The enclosure is fabricated from 5-mm-thick aluminum floor plate and has double-doors on three sides to ensure convenient access to the camera system. The Faraday enclosure is cemented to a concrete-block wall that is spanned by steel-reinforced concrete lintels to minimize vibration of the system, which is located in the building subbasement. A metal framework suspended from the ceiling supports the perfusion system pumps and power supplies and isolates their vibrations from the camera system.

6.3.8. Computer Control

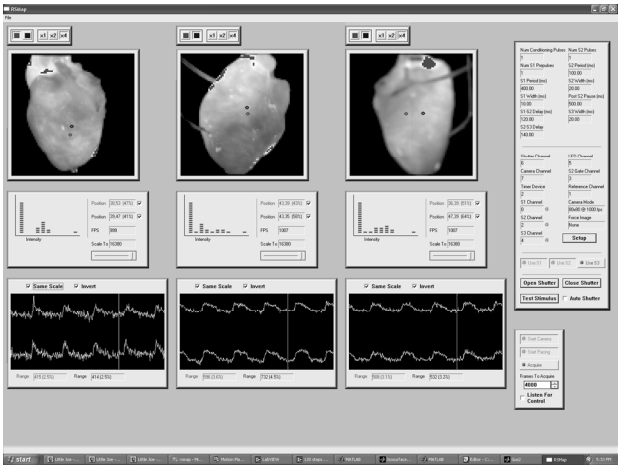

Figure 6.8. Screenshot of the control program during an experiment. Reduced frame-rate video feeds, intensity histograms, and real-time traces of a few selected pixels are displayed. The two panels on the right control illumination, rotation control, stimulus timing, and image acquisition.

The three cameras, illumination, stepping motor and cardiac stimulation are all controlled from one computer using a custom control program written in C. The control program, whose graphic user interface is shown in figure 6.8, displays a reduced-frame-rate video feed for monitoring camera focus and alignment, fluorescence signal strength information, settings for controlling the duration and method of high-frame-rate capture, and stimuli settings. This single program thereby eliminates the need for the experimenter to control multiple computers along with the associated peripheral devices.

6.4. Algorithms And Post Processing

The procedure for reconstructing the surface contours of the heart has been described previously [2], but is outlined here briefly. The geometric reconstruction of the

heart is preceded by determining the camera parameters, which are needed for the reconstruction algorithm. A calibration object with fiducial markers is placed in the panoramic setup. For our purposes, a hexagonal object was chosen as the optimal shape to provide adequate spatial perspective to each camera for the calibration algorithm (which requires non-coplanar views). An image transformation matrix is then generated for each camera. This provides the mapping for each (x,y,z) point in 3-D object space to its corresponding (x,y) point in the 2-D image plane of the camera.

The geometric reconstruction of the heart is generated using the method of occluding contours [3], which follows five steps:

(1) A virtual volume lattice of three-dimensional points (voxels) is initialized.

(2) A snapshot of the heart is acquired. The heart contour is segmented from the background, and contoured to yield the silhouette of the heart.

(3) The heart image is back-projected into the volume grid using the image transformation matrices determined earlier. A point-in-polygon test is used to find those voxels which lie within the image contour, which are marked. This is performed for each of the three cameras.

(4) The heart is rotated by $\Delta\theta$ using the microstepper and the volume lattice is rotated by the same amount.

(5) Steps (2)-(4) are repeated until a sufficient amount of the surface area of the heart has been mapped by all three cameras such that there are no regions of ambiguity.

The end result is a volume lattice in which the marked voxels represent those 3-D points that enclose an object with the same surface boundaries as the heart. The lattice is then isosurfaced to yield the final bounding surface of the reconstructed heart.

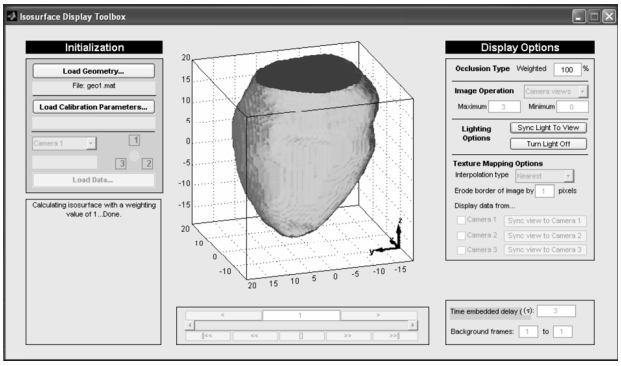

Figure 6.9. Isosurface Display Toolbox displaying the virtual cardiac surface before data is mapped onto the surface.

The fluorescence information may then be mapped onto the geometric surface. However, since regions of overlap exist on the surface that correspond to multiple camera perspectives but differ in fluorescence intensity depending on the camera view with respect to the relative position of the region, further steps must be taken to correct the fluorescence values to create a globally continuous intensity map. Therefore, the fluorescence intensity in these areas is weighted by the angle between the surface and the camera viewpoint. Those intensity values produced by surfaces perpendicular to the camera viewing axis receive the greatest weight, whereas those which are parallel receive the least. The weighted intensity average is then computed for these overlapping regions to produce the final intensity map, in a manner similar to that described in [3]. A custom-built interactive program, our Isosurface Display Toolbox, was written in MATLAB (The MathWorks Inc, Natick, MA USA) to construct the virtual cardiac surface shown in Figure 6.9 using our published algorithms [2].

6.5. Results

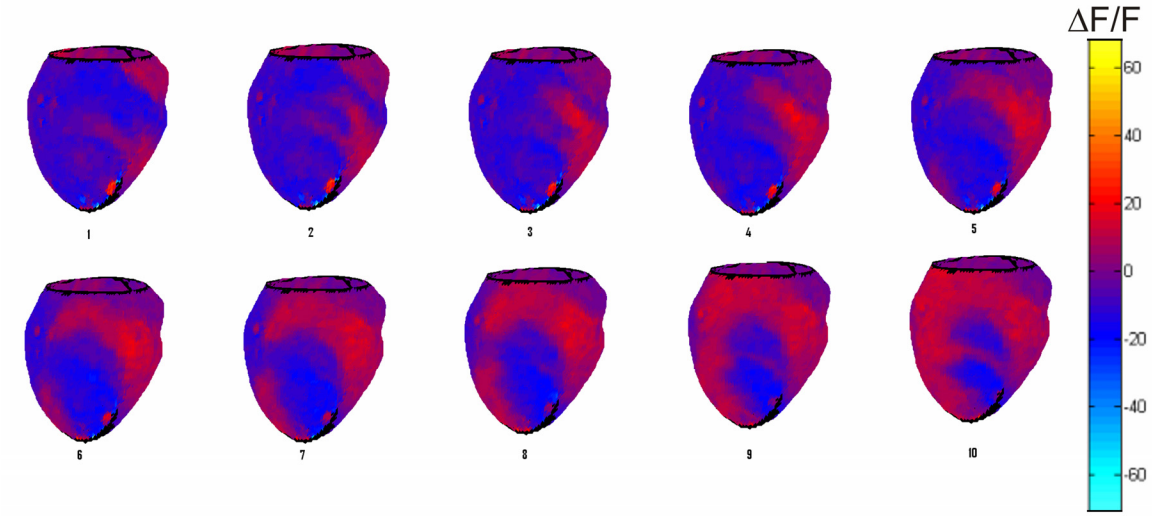

Figure 6.10. Figure of eight reentry during polymorphic tachycardia. Every 5th frame of a 1000 fps sequence is shown. The excited tissue is red. The persistent red dot in the lower right of each image is an artifact due to the electrode.

Using the system just described, we conducted three demonstration experiments using rabbit hearts; two using the Redshirt configuration, and one using the Dalsa cameras. Figure 6.10 shows a sample of the results using the Redshirt cameras in their 1000 fps-80 × 80 pixel mode. The heart was prepared as described previously [1]. Ten frames from a 50 ms interval of a rabbit heart in polymorphic tachycardia are shown. The arrhythmia was initiated by a series of four 20 ms stimuli of 20 mA spaced at 100 ms. A custom stimulator connected to a point-electrode placed on the left ventricle provided the stimulus. Every fifth frame is shown, which gives a 5 ms interval between images. The sequence shows a figure–of-eight reentry which is a common phenomenon observed in cardiac arrhythmias.

6.6. Discussion

We have described and demonstrated a system which allows for both high spatial and temporal resolution of the transmembrane potential over the entire epicardial surface of a rabbit heart. The primary advantage of the panoramic imaging approach is that it allows the tracking of electrical activity that might propagate out of the field of view of a single camera that can view only one side of the heart at a time. Our implementation of the panoramic camera is designed to optimize the mechanical stability of the system, the accuracy of the reconstruction, and ease-of-use. Elsewhere we will report the use of this system to study the effects of global ischemia on propagation, and the virtual electrode distribution from intracavity defibrillation strength shocks.

6.7. Acknowledgements

This work was supported in part by National Institutes of Health (R01-HL58241) and the Vanderbilt Institute for Integrated Biological Research and Education (VIIBRE). Hana Dobrovolny and Daniel Gauthier gratefully acknowledge the financial support of the National Science Foundation (PHY-0243584) and the National Institutes of Health (1R01-HL-72831). We thank Richard Gray of the University of Alabama at Birmingham for sharing his two Redshirt cameras for collaborative studies. We thank Tyler Winston and Patrick Park for their participation in the senior-engineering design project that was associated with the development of this camera, and Joan Walker for her advice and guidance during that part of the effort. We are indebted to Mike Welfel at PDM in Nashville, TN for supervising the careful machining of the mechanical components for the system, and Jeff Boone, Kenneth Miller, and Ron Lemaire at Duck Welding in

Nashville, TN for their design and fabrication of the Faraday shield. We thank Robel Bekele for his assistance with the illumination system. We thank Ron Reiserer for his advice.

6.8. References

1 Lin, S.F., and Wikswo, J.P., "Panoramic optical imaging of electrical propagation in isolated heart". J Biomed Opt, 4, 200, 1999.

2 Bray, M-A., Lin, S.F., and Wikswo, J.P., "Three-dimensional surface reconstruction and fluorescent visualization of cardiac activation". IEEE Trans BME, 47, 1383, 2000.

3 Niem, W., "Robust and fast modeling of 3D natural objects from multiple views". SPIE Proc., "Image and Video Processing II". vol. 2182, pp. 388–397, 1994.

4 Kay, M., and Rogers, J., "Three-dimensional surface reconstruction and panoramic optical mapping of large hearts". IEEE Trans BME, 51, 1219, 2004.

5 Qu, F., Fritz, A., Cheng, Y, Nikolski, V., Efimov, I.R., "Panoramic Imaging of Electrical Activity in the Rabbit Heart". PACE, 26: 946, 2003.

6 Woods, M.C., "The Response of the Cardiac Bidomain to Electrical Stimulation". Doctoral dissertation, Vanderbilt University, Chapter 6, 109-135, 2005.

CHAPTER VII

FIELD STIMULATION OF THE DIASTOLIC RABBIT RIGHT VENTRICLE

Mark R. Holcomb,[1] Veniamin Y. Sidorov,[2] David N. Mashburn,[1] Marcella C. Woods,[2] and John P. Wikswo[1,2,3]

1. Department of Physics, and Astronomy, Vanderbilt University
2. Department of Biomedical Engineering, Vanderbilt University
3. Department of Molecular Physiology and Biophysics, Vanderbilt University

7.1. Introduction

The application of strong electric shocks during cardiac defibrillation changes the transmembrane potential, V_m, throughout the myocardium, leading to the termination of reentrant waves that support cardiac fibrillation. There are two major processes that take place during successful defibrillation [1]: (1) The applied current traverses the entire myocardium, repeatedly moving between the intracellular and extracellular spaces, because of the spatially dependent electrical anisotropy of the cardiac tissue and structural heterogeneities which cause changes in V_m throughout the myocardium [2,3] and (2) these changes in V_m, by both excitory and inhibitory effects, lead to the termination of all fibrillation wavefronts. This study relates to both processes by examining the relationships between electroporation, virtual electrode polarization (VEP), and fiber geometry.

7.1.1. Electroporation

Cell membranes exposed to strong electric fields exhibit a large increase in conductivity which lasts for several seconds to minutes [4,5]. This effect is termed electroporation, wherein the electric field causes the formation of transient pores in the membrane. Electroporation is thought to play a primarily depressive role in defibrillation [12-14] although, in the whole animal, electroporation has been attributed to reduction of the defibrillation threshold by reduction of the total resistance in the defibrillation circuit [15]. The bidomain model discussed in section 2.6 has been very successful in predicting the response of cardiac tissue in a variety of stimulation conditions. However, the bidomain predicts very high V_m values during defibrillation strength shocks that are never observed in experiments [6]. It is generally accepted that these high V_m values are never observed due to electroporation. Neunlist *et al*. [5] showed that V_m approaches maximum hyperpolarization and depolarization values in a sigmodial fashion with increasing shock strength. Jones *et al*. [7] were the first to observe electroporation in cardiac tissue following defibrillation strength shocks. Electroporation occurs in single cardiac cells when absolute value of V_m reaches approximately 400 mV [4,8], but the value for intact tissue is unknown.

Krassowska *et al*. [9-11] have developed a macroscopic model of membrane electroporation that is in good agreement with experimental results. The central observation in these studies is that there is a critical value of transmembrane potential (V_{cr}) above which electroporation occurs. Stronger shocks do not cause V_m to exceed V_{cr} by a significant amount. The explanation of this observation is that above V_{cr} the pores

form, effectively shunting excess current across the membrane, and thereby preventing V_m from growing as large as would be expected from a simple cable model.

It is clear from equations (2.14) and (2.15) that the introduction of ion non-specific pores with high relative conductivity will make the resting potential less negative. In terms of the passive cable model it will shorten the length constant as well, which taken by itself would make defibrillation more difficult. Reductions of action potential amplitude and upstroke time following a strong shock are also indicators of electroporation [4,12].

The number and size of the pores are dependent on the shock strength and membrane kinetics, *i.e.*, systolic or diastolic shocks [16]. Simulations show that in a 2-D bidomain sheet, electroporation not only controls the degree of VEP but also partially determines the shape of macroscopic VEP [6].

Electroporation has been reported to be greater in regions of larger spatial heterogeneity such as the endocardium [17]. It is hypothesized that the large spatial heterogeneities lead to large field gradients which cause greater electroporation [5,17,18].

7.1.2. Virtual Electrode Polarization

Virtual electrode polarization refers to regions of tissue that become polarized or depolarized in response to stimulation, but are distant from an electrode. These "virtual" electrodes resemble tissue that is responding to a "real" electrode during a stimulus. There is good agreement between the predictions of bidomain simulations and experiment [19] for VEP associated with point stimulation. VEP is also thought to play a major role in defibrillation. Originally, it was thought that defibrillation shocks

succeeded by simply synchronizing the entire myocardium to the same depolarized level. Experimental observations indicate the process is much more complicated. For example, during shocks there are virtual anodes (regions of hyperpolarization), virtual cathodes (regions of depolarization), and areas that are initially unaffected. The locations, magnitude, spatial size, and temporal evolution of VEP are key links in understanding defibrillation. Efimov *et al.* [20] demonstrated direct evidence of the role of VEP in success and failure of defibrillation.

Clearly, a successful defibrillation shock must extinguish all fibrillatory activity and not introduce new ones [21,22]. As described in section 2.7, the cardiac action potential is roughly periodic and is often described in terms of its phase [23,24]. VEP modifies the phase portrait of the tissue which can lead to successful defibrillation, but can also lead to defibrillation failure by creating new large phase gradients. Biphasic shocks work, in part, by annihilating the phase gradients created by the initial shock.

Action potential durations (APDs) and refractory periods (RPs) are lengthened by virtual cathodes and shortened by virtual anodes [25]. The associated damped propagation in the affected areas can be proarrhythmic [26]. The liminal volume, the volume of tissue that needs to be elevated above threshold in order to create a propagating wavefront, is on the order of 1 mm^3 [27,28], and represents the size of the virtual cathode at threshold. VEP may also lead to excitable gaps in refractory tissue [20], and explain the process of break stimulation [19].

7.1.3. Fiber Geometry

Simulations show that fiber curvature with respect to an applied electric field, along with unequal anisotropy, leads to depolarization and hyperpolarization throughout the heart [2,29]. Fiber direction is thought to be a large factor in current distribution in defibrillation shocks [1,32]. The unequal conductivity ratios in the longitudinal and traverse directions with respect to the fibers are the critical factor in understanding the effect. Current distributes itself in the intracellular and extracellular spaces according to the conductivities in those spaces. Any fiber curvature with respect to the applied field results in a component of current that crosses the membrane, resulting in a change in V_m [30].

Fiber curvature and rotation are present in whole hearts at several levels [4-6]. The most obvious is due to the spheroidal shape of the heart. In previous field-shock studies of whole hearts, it was shown that this type of global curvature due to the shape of the heart dominates the field shock response [31]. Fiber curvature is also present due to rotation in and through the plane of the applied electric field.

The accomplishments of the bidomain model discussed in section 2.6 are one example of the importance of fiber orientation. The bidomain presents a good localized representation of the unequal anisotropies which are one of the determining factors in the response of cardiac tissue to point stimulation. Much effort has been directed at documenting the spatially complex fiber geometry of the ventricles using optical histology [33-39]. Interest in fiber geometry is not limited to the ventricles; Gray *et al*. [40] reported experimental evidence that the three-dimensional structure of the atria plays a major role in the activation sequences during fibrillation.

More recently, diffusion tensor magnetic resonance imaging (DTMRI) has been used as a non-destructive and much less expensive method than optical histology on serial sections to obtain three-dimensional fiber geometry of cardiac tissue [41]. Several studies have verified the accuracy of the DTMRI data. Hsu *et al*. [42] performed a direct comparison of DTMRI data and histology measurements on a section of canine myocardium and reported only small discrepancies. Holmes *et al*. [43] performed direct histological measurements and DTMRI data on a formaldehyde-fixed White New Zealand rabbit, the same species and preparation used in the present study. They reported an average of 3.7° difference in fiber direction measured by the two modalities. Muzikant *et al*. [44] demonstrated the usefulness of DTMRI data by showing that a model using DTMRI fiber information was more accurate than a bidomain simulation alone in describing the behavior near a pacing electrode.

Tissue structure beyond the classic bidomain have also been indicated as determining factors of the position of VEP , including unexcitable areas and voids [45], tissue-fluid interface[46], and general heterogeneities [47].

7.2. Materials and Methods

7.2.1. Experimental Preparation

All experiments conformed to the National Institutes of Health guidelines for the ethical use of animals in research and were pre-approved by the Vanderbilt Institutional Animal Care and Use Committee.

New Zealand white rabbits (2.2-3.6 kg) were first preanesthetized with intramuscular ketamine (50 mg/kg). Intravenous heparin (2000 units) and pentobarbital (60 mg/kg) were then administered, and the hearts were excised quickly in preparation for Langendorff perfusion of the whole heart. The ascending aorta was cannulated and secured for retrograde perfusion of the coronary arteries with oxygenated (95% O2; 5% CO2) Tyrode's solution of the following composition (in mM): 133 NaCl, 4 KCl, 2 $CaCl_2$, 1 $MgCl_2$, 1.5 NaH_2PO_4, 20 $NaHCO_3$, and 10 glucose. The temperature of the solution was maintained at 37° C, and the pH was regulated to 7.4 ± 0.05. After five minutes, the right ventricular wall was removed, and the right coronary artery was cannulated. The right ventricle (RV) was then affixed to a custom holder by cactus needles positioned around the periphery of RV. The holder was then placed in a warmed, oxygenated, circulating bath of Tyrode's solution as shown in Figure 7.1. To minimize motion artifacts, the excitation-contraction decoupler diacetyl monoxime (DAM, Sigma-Aldrich, St. Louis, MO) was added to the Tyrode's solution at a concentration of 15-20 mmol/L.

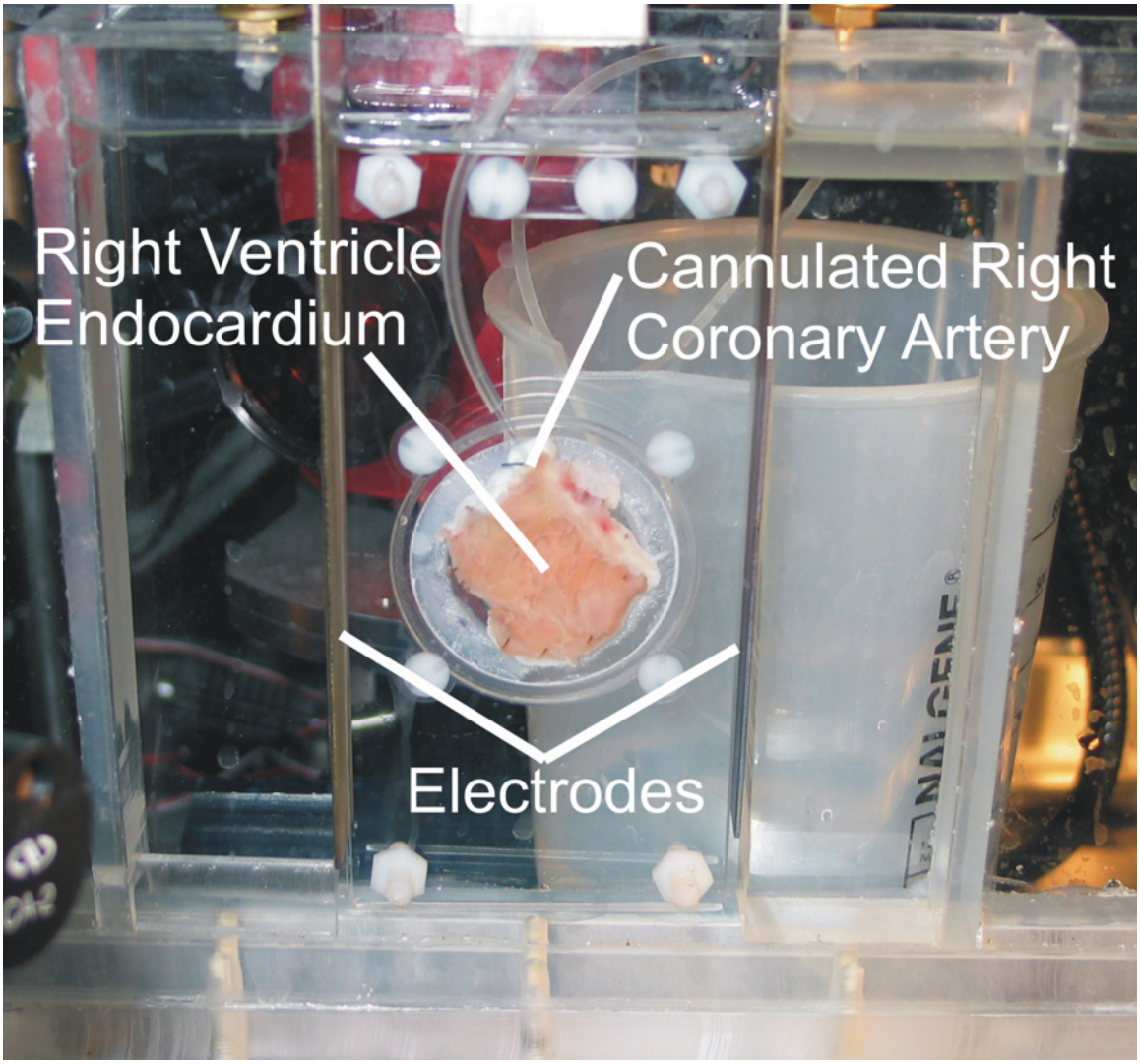

Figure 7.1. RV bath and holder. The bath is constructed of two glass plates separated by 2.5 cm plexiglass spacers sealed with silicone rubber. The electrodes are spaced 6 cm apart. The holder is made of plexiglass, and a thin sheet of Slygard silicone allows the RV to be attached to the holder with cactus needles. The RV overlaps a 22 mm diameter hole. The transparent glass allows viewing of both sides of the RV.

7.2.2. Stimulation Protocol

Pacing stimuli (S1) were delivered via the titanium plate electrodes, shown in Figure 7.1, at a basic length cycle of 400 ms. Constant current pulses between 60 mA and 100 mA were delivered by a custom USB (Universal Serial Bus) powered stimulator.

The duration of the pacing pulses ranged from 6 ms to 12 ms. Pacing was done at threshold. Strong shocks (S2) were produced by a custom, computer-controlled high-voltage stimulator (Ventritex, Sunnyvale, CA). S2 stimuli of 2 ms duration and varying amplitude were delivered during diastole (S1-S2 coupling interval of 400 ms) and applied via the same electrodes used for pacing. To allow the tissue time to recover between shocks, we waited two minutes between shocks of 33.3 V/cm or less and three minutes for larger shocks.

7.2.3. Optical Imaging

To view changes in V_m, 200μL of the voltage-sensitive fluorescent dye di-4-ANEPPS (0.5 mg/mL dimethyl sulfoxide; Molecular Probes, Eugene, OR) was administered via a bolus injection into a bubble trap above the RV. The RV was illuminated with a diode-pumped, solid-state 532 nm laser (Verdi, Coherent, Santa Clara, CA). The emitted light was passed through a cutoff filter (no. 25 Red, 607 nm, Tiffen, Japan). Redshirt CCD cameras (Decatur, GA) were used to record the fluorescence signals. A 2 cm × 2 cm region centered over the hole in the holder was imaged. The data were not filtered. All data were normalized on a pixel-by-pixel basis according to the change in fluorescence (F) during the S1 pacing response preceding the S2. The resulting normalized data (F_{norm}) ranged from 0 (rest) to 1 (peak) for the S1 response.

7.2.4. Experimental Considerations

The thin, flat RV preparations used in this study provide an opportunity to elucidate some of the relationships between electroporation, VEP, and fiber geometry while eliminating the curved ventricular boundaries characteristic of shock experiments on the intact heart. We selected the stimulation and image acquisition protocols to investigate these relationships within several experimental limitations.

The surgery to remove the RV wall, cannulate the coronary artery, and affix it to our holder is complex compared to what is required for whole heart studies. There are usually some regions of tissue that are ischemic or do not stain well. If a substantial amount of the RV is ischemic, or even a small region near the center of the RV is ischemic, then the preparation cannot be used. To be included in the analysis, an RV must remain "healthy" for the duration of the protocol. We defined a healthy preparation as one in which the tissue's action potential duration (APD) and action potential amplitude (APA) are characteristic of healthy tissue. Also, the analyzed areas must not border unhealthy regions. For most of our analyses we used regions centered in the field of view of each preparation. Not using all the data in the field of view is necessary to ensure the phenomena reported are not caused by edge effects or unhealthy tissue just outside the visible region.

Strong electric shocks have a deleterious effect on the preparations. Therefore, only a subset of all the protocols used in the study could be applied to a single preparation. The amount of time a preparation stays healthy varies by a factor of two or three, but there is no way to know how long a preparation will remain healthy in advance, so some preparations are probably underutilized.

Only one camera is available that can record at 5000 fps, so observations at this frame rate were limited to one side of the RV. Due to the goals of the study, the data were not temporally or spatially filtered. When imaging these preparations, the three utilized camera speeds have a noise standard deviation (SD) of approximately 0.05 initially, and degrade to a SD of approximately 0.08 at which point the preparations are no longer used. These measurements are with respect to the S1 normalized signals.

Biphasic waveforms [48] are used in clinical defibrillators and many studies similar to the present one. A device for producing high strength biphasic waveforms was not available. The response of diastolic tissue to monophasic shocks is relatively rare in the literature. Based on models, Walcott *et al*. [49] reported the optimal monophasic waveform for defibrillation is also the optimal first phase of a biphasic waveform. A complementary study using biphasic waveforms would be useful, but using monophasic shocks does not make the results of the present study less relevant.

The justification and purpose of the three protocols are described briefly here, and are expanded along with the results and discussion in other sections:

Protocol 1 views only the endocardium at 5000 fps at 26×26 pixels. Each pixel represents approximately 0.8 mm square. Shocks of 2 ms duration and strengths from 1 V/cm to 83.3 V/cm are used. The high frame rate shows that the degree of hyperpolarization is much greater in some areas than is visible in slower recordings. This allows a more meaningful correlation of maximum hyperpolarization (virtual anodes) and electroporation in diastolic tissue which is one of the primary goals of this study. These high temporal resolution recordings serve to characterize the preparation's response to stimulation and aid the interpretation of data from the other protocols; since the

symmetry and degree of hyperpolarization are observed repeatedly in the high speed recordings, it is reasonable to assume the same response is present in other acquisition protocols even if it is not clearly visible in the data.

Protocol 2 views both the epicardium and endocardium at 3000 fps at a resolution of 40×40 pixels with synchronized cameras. Each pixel represents approximately 0.5 mm square. Shocks of 2 ms duration with strengths from 1 V/cm to 83.3 V/cm are used. It is expected that the more heterogeneous endocardium would have more activation points, and hence shorter activation times. The frame rate and resolution were chosen to see the spatial detail of the activation points, as well as the distinguish the temporal differences.

Protocol 3 views both endocardium and epicardium at 1000 fps at a resolution of 80×80 pixels with synchronized cameras. Each pixel represents approximately 0.25 mm square. Shocks of 2 ms duration with strength of 60 V/cm at both polarities are applied at 0, 45, 90, and 135 degrees with respect to the original orientation. This, in effect, is a 360° rotation in 45° increments with respect to the electric field. The higher spatial resolution allows the comparison of VEP and electroporation with respect to field direction, not just reversal of polarity. DTMRI data were acquired from one RV following the protocol.

7.2.5. Analysis Methods

In the following sections we examine the temporal and spatial evolution of V_m in response to alternate polarity shocks. In order to analyze the data beyond a presentation of the S1 normalized fluorescence signals, we will utilize autocorrelations and cross-

correlations. In this section we use artificial datasets to illustrate the output of the various correlation methods which will help in the interpretation of the experimental data, and also justifies our choice for the methods we ultimately use.

Two correlation functions available in Matlab have detailed descriptions in the documentation and are often used in this type of analysis; *xcorr2* and *normxcorr2* provide 2-dimensional autocorrelations and cross-correlations. The principle difference in the two is that the latter normalizes the output to a range between -1 and 1. We will define two similar functions that, in most cases, better illustrate the interesting features of our data. We denote the first function as the Normalized Sliding Dot Product (NSDP). In the code snippet below, variables *a* and *b* are 16×16 arrays.

```
%Normalized Sliding Dot Product.
% a and b are 16x16 arrays (image data)
n1 = sum(dot(a,a));
n2 = sum(dot(b,b));
for i = -7:7
    for j = -7:7
       x = sum(sum(dot(circshift(a,[i j]),b)));
       cc(i+8,j+8) = x;
    end
end
cc = cc/(n1*n2)^(1/2);
```

The second function is denoted as the Zero Mean Normalized Sliding Dot Product (ZMNSDP). This is identical to NSDP except the mean pixel value of each image is subtracted from each pixel in the image before computation.

Panel A in figure 7.2 shows a 16×16 pixel checkerboard pattern of simulated data with repeated values of -1 and 1. Panels B and C show the autocorrelation of panel A using the Matlab functions *xcorr2* and *normxcorr2*, respectively. For a square input matrix of side n, both functions output a square matrix of side 2n-1. Panel D shows the output of the autocorrelation of panel A using the NSDP method which is an identical

checkerboard pattern of values -1 and 1. This is an intuitive result and is completely free of the edge-effects seen in panels B and C. In this special case, where the initial data already has a zero mean, the ZMNSDP method would give identical results to panel D.

Panel E shows a 16×16 pixel region with all pixels set to zero except for two. The two different pixels are set to 1 and -1. This is an idealized representation of one small virtual cathode and one small virtual anode surrounded by resting tissue. Panel F is identical to panel E except the positions of the virtual cathode and virtual anode are reversed. Panels G-J show the cross-correlations of panels E and F using *xcorr2*, *normxcorr2*, NSDP, and ZMNSDP, respectively. Rows (K-N), (O-R), (S-V), and (W-Z) show the cross-correlations produced by the four methods on panels E and F with all background pixels set to 0.05, 0.1, 0.2, and 0.5, respectively. This could be interpreted as one pair of complimentary virtual electrodes surrounded by progressively more activated tissue. The two Matlab functions clearly show edge artifacts that obscure the existence and location of the complementary virtual electrodes. For most of our analysis we will use the NSDP and ZMNSDP methods because of the intuitive application and interpretation of the results. The central pixel (zero shift) produced by the two methods is probably the most useful in identifying an underlying symmetry or asymmetry within the data.

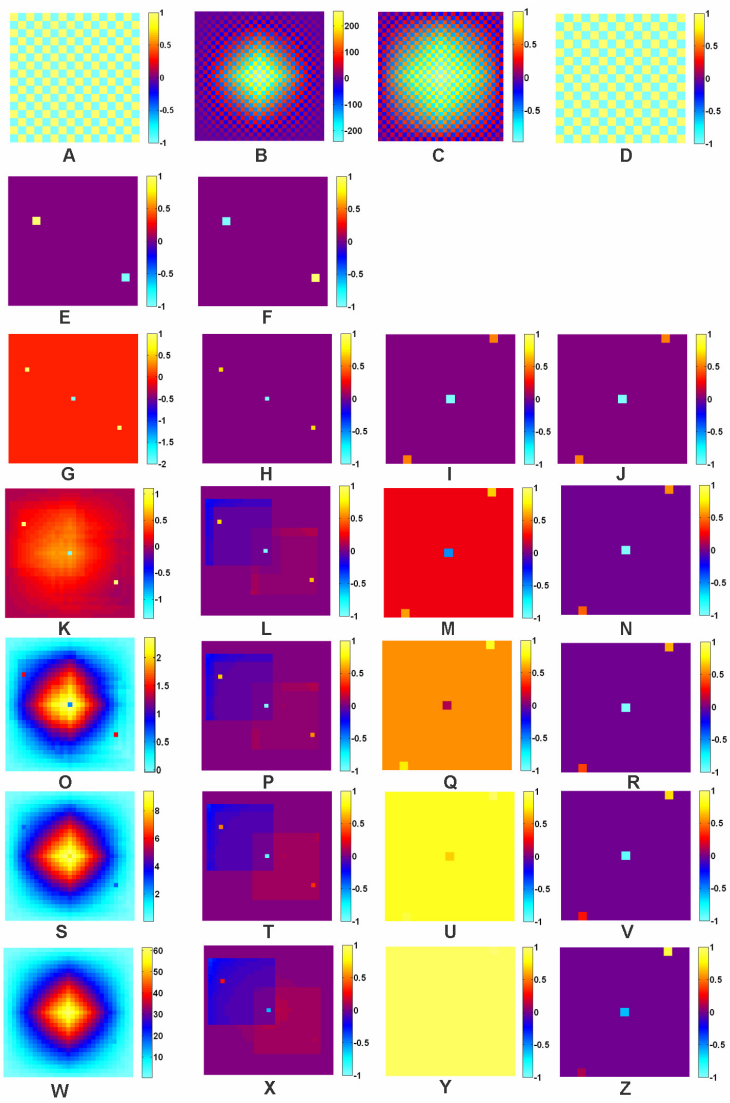

Figure 7.2. (A) shows a checkerboard pattern (1,-1,…) of simulated data. (B-D) shows the autocorrelation of A using the Matlab *xcorr2* function, Matlab *normxcorr2* function, and ZMSDP method, respectively. (E) shows simulated data with all pixels set to zero except two, for which the values are 1 and -1. (F) identical to E except the values of the two non-zero pixels is reversed. (G-J) shows the cross-correlation of E and F using the Matlab *xcorr2* function, Matlab *normxcorr2* function, NSDP method, and ZMNSDP method, respectively. (K-N) identical to G-J except the zero backgrounds in E and F are set to 0.05 before computation. (O-R) identical to G-J except the zero backgrounds in E and F are set to 0.1 before computation. (S-V) identical to G-J except the zero backgrounds in E and F are set to 0.2 before computation. (W-Z) identical to G-J except the zero backgrounds in E and F are set to 0.5 before computation.

7.3. Protocol 1

7.3.1. Complementary Shock Response

Four successful preparations were used in this protocol, denoted RV1-RV4. Parts A and B of Figures 7.3-7.6 show the endocardial response of RV1-RV4, respectively, to 2 ms 300 V (50 V/cm) shocks of both polarities. The direction of the electric field is indicated by the arrows. In the discussions that follow, positive and negative stimuli refer the field directions in parts A and B, respectively, of Figures 7.3-7.6. Note that regions of hyperpolarization that develop at one polarity are regions of early activation in response to the opposite polarity. This sharp reversal of virtual anodes and virtual cathodes for opposite polarities is not usually observed in diastolic tissue because activation obscures the effect. The regions of early activation and hyperpolarization are dispersed across the RV. This is distinctly different from the "left-right" effect observed in whole-heart studies [31]. This symmetric response to alternate polarities is not unexpected. As shown by Woods *et al.* [31], activation in whole hearts normally occurs on the same side as the cathode, and hyperpolarization occurs on the side facing the anode. Evidently, with the whole-heart curvature removed, the remaining heterogeneities are responsible for the more spatially dispersed VEP. In addition to the whole heart studies just mentioned, cardiac myocytes also show a symmetric response during field shock [50], as does intact cardiac tissue in response to point stimulation [19]. These results illustrate the important role structure plays in the response to field shock. The nature of this structure is examined in section 7.5.

The third row in each figure is the average (the pixel-by-pixel average of each of the corresponding images in the sequence) of the two polarities. Note there appears to be spatially uniform activation in these averaged sequences, which is what would be expected if the shock response is symmetric because of complementary virtual cathodes and anodes upon shock reversal. The average appears to be shifted to the red (activation) due to the proportionality of hyperpolarization and activation—the data are normalized to an S1 amplitude of 1, but a hyperpolarization of -0.2, for example, is large.

Rows D and E in the figures show the centered 16×16 pixel regions for A and B, respectively. This removes the edges of the tissue, and allows a more consistent comparison between preparations. Rows F and H in the figures show the autocorrelation of rows D and E, respectively, using the NSDP method. Rows G and I show the autocorrelation of D and E, respectively, using the ZMNSDP method. Rows J and K show the cross-correlation of D and E using the NSDP and ZMSDP methods, respectively. Each field of view in Figures 7.3-7.6 is approximately the same, but the RVs are slightly different sizes, and some stain toward the edges of the tissue better than others.

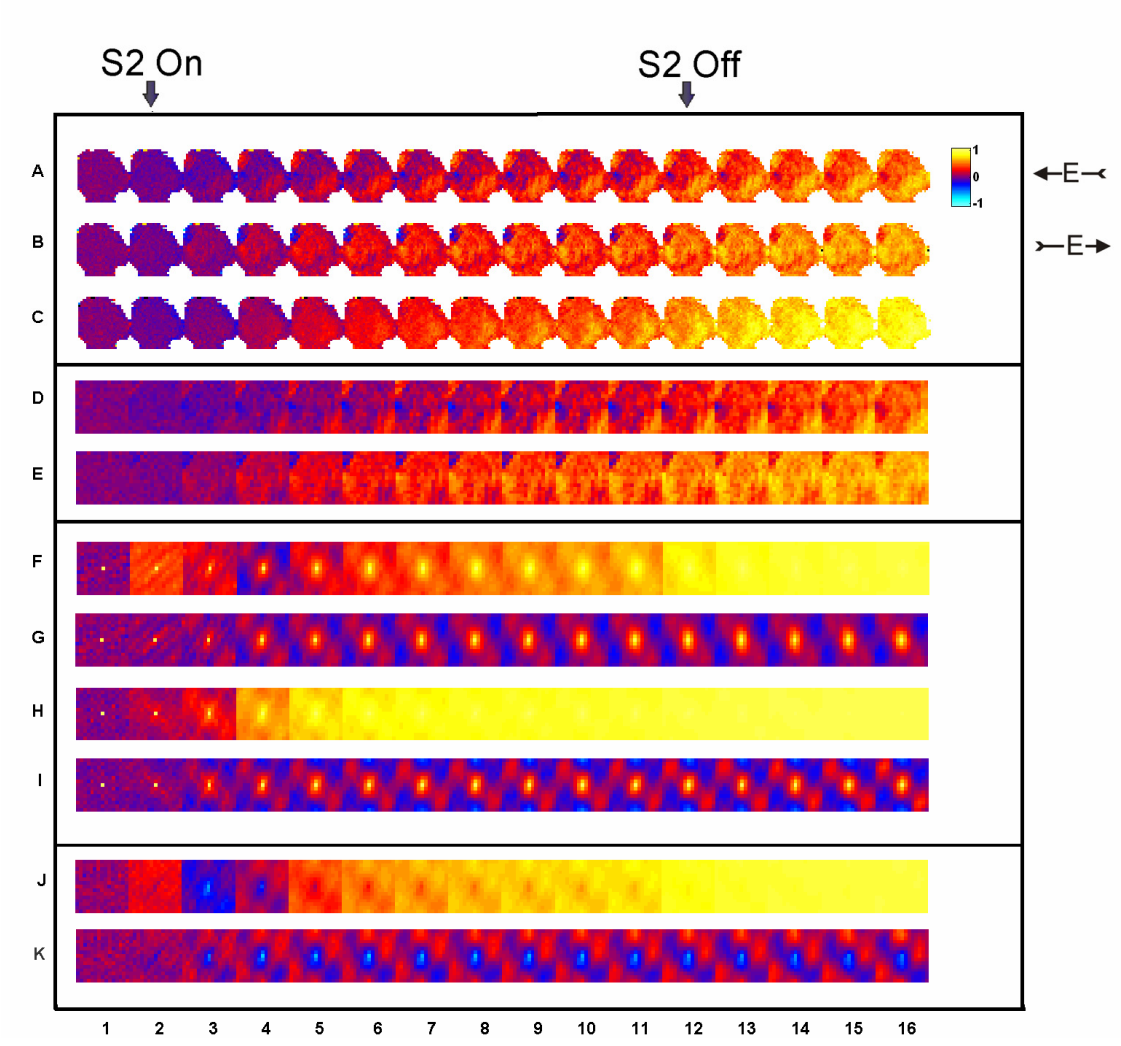

Figure 7.3. RV1 endocardial response to 2 ms 300 V (50 V/cm) shocks of both polarities (Direction of field indicated by arrows in A and B). The onset of the shock occurs at the beginning of frame 2 and terminates at the end of frame 11. Each sequence was acquired at 5000 fps with a resolution of 26×26 pixels. (C) Average of A and B. (F) and (G) are the autocorrelations of D using the NSDP and ZMNSDP methods, respectively. (H) and (I) are the autocorrelations of E using the NSDP and ZMNSDP methods, respectively. (J) and (K) are the cross-correlations of D and E using the NSDP and ZMNSDP methods, respectively.

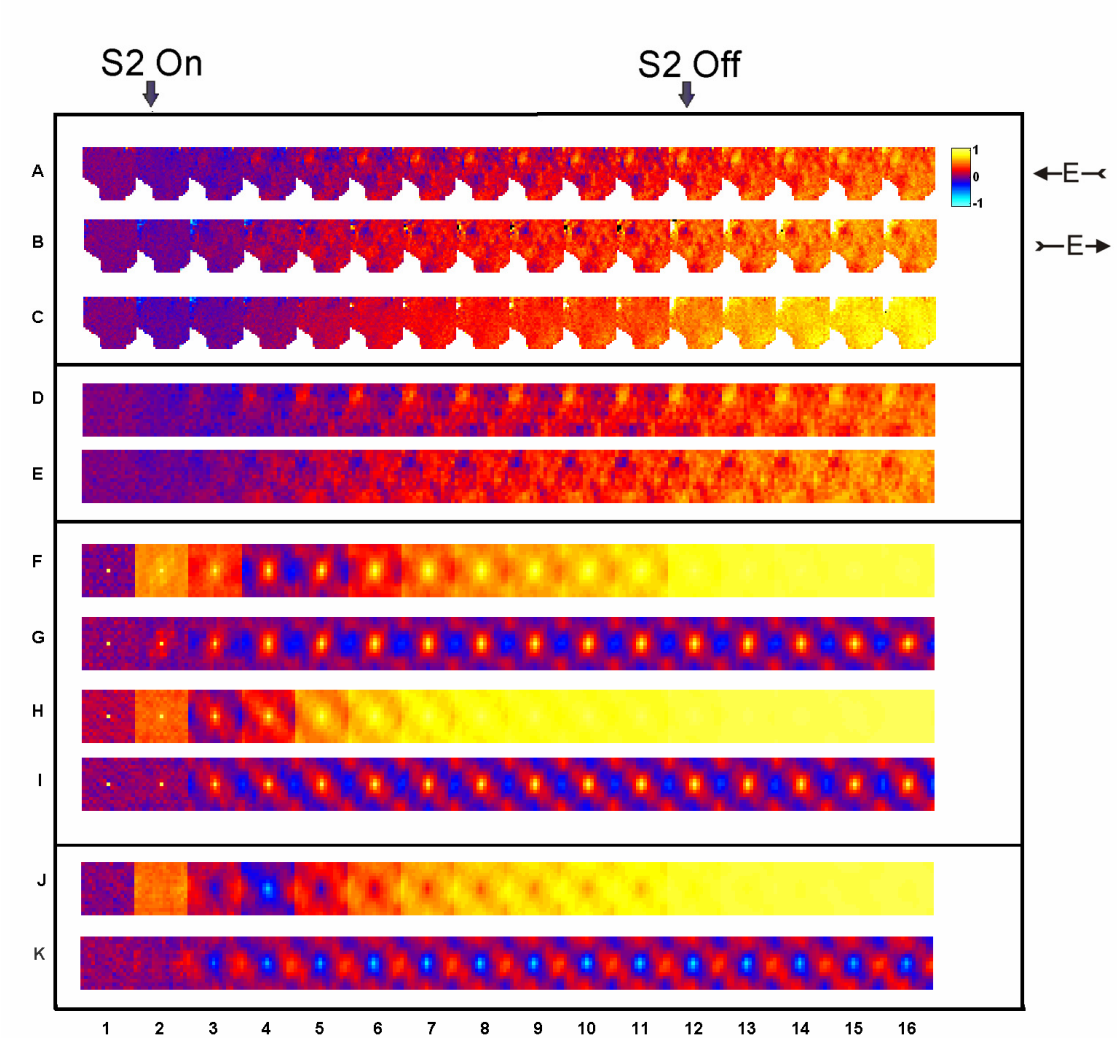

Figure 7.4. RV2 endocardial response to 2 ms 300 V (50 V/cm) shocks of both polarities (Direction of field indicated by arrows in A and B). The onset of the shock occurs at the beginning of frame 2 and terminates at the end of frame 11. Each sequence was acquired at 5000 fps with a resolution of 26×26 pixels. (C) Average of A and B. (F) and (G) are the autocorrelations of D using the NSDP and ZMNSDP methods, respectively. (H) and (I) are the autocorrelations of E using the NSDP and ZMNSDP methods, respectively. (J) and (K) are the cross-correlations of D and E using the NSDP and ZMNSDP methods, respectively.

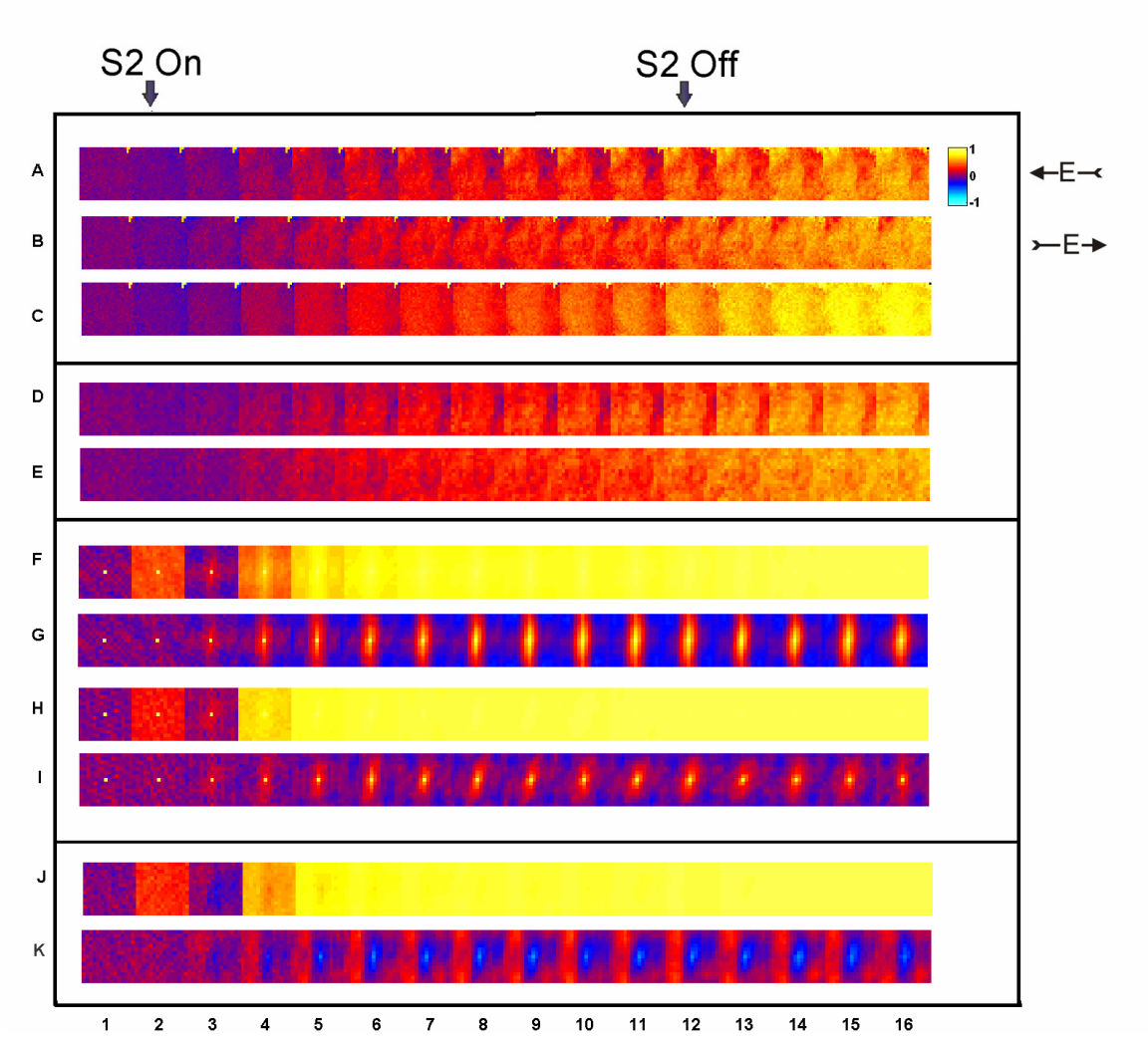

Figure 7.5. RV3 endocardial response to 2 ms 300 V (50 V/cm) shocks of both polarities (Direction of field indicated by arrows in A and B). The onset of the shock occurs at the beginning of frame 2 and terminates at the end of frame 11. Each sequence was acquired at 5000 fps with a resolution of 26×26 pixels. (C) Average of A and B. (F) and (G) are the autocorrelations of D using the NSDP and ZMNSDP methods, respectively. (H) and (I) are the autocorrelations of E using the NSDP and ZMNSDP methods, respectively. (J) and (K) are the cross-correlations of D and E using the NSDP and ZMNSDP methods, respectively.

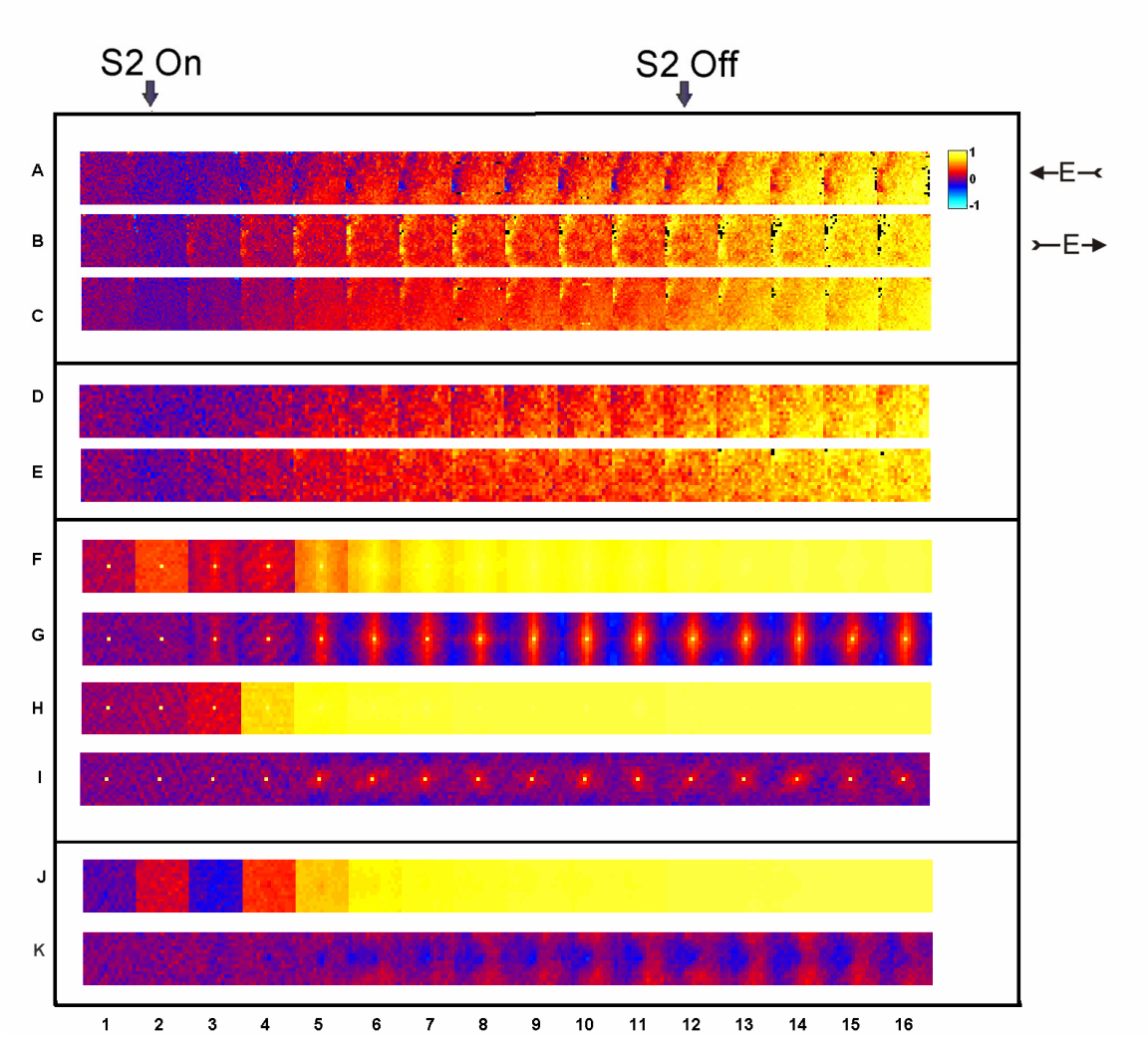

Figure 7.6. RV4 endocardial response to 2 ms 300 V (50 V/cm) shocks of both polarities (Direction of field indicated by arrows in A and B). The onset of the shock occurs at the beginning of frame 2 and terminates at the end of frame 11. Each sequence was acquired at 5000 fps with a resolution of 26×26 pixels. (C) Average of A and B. (F) and (G) are the autocorrelations of D using the NSDP and ZMNSDP methods, respectively. (H) and (I) are the autocorrelations of E using the NSDP and ZMNSDP methods, respectively. (J) and (K) are the cross-correlations of D and E using the NSDP and ZMNSDP methods, respectively.

Note there is no apparent structure in the frame preceding shock onset in the autocorrelations shown in parts F-I or cross-correlations in parts J-K. We can conclude that none of the spatial structure we see later in the correlations is due to background or

normalization artifacts. Parts F and H in the figures all show a nearly uniform global positive autocorrelation in the first 200 μs of the shock. This is due to an observed small polarity independent global hyperpolarization. It is interesting that the effect of the global hyperpolarization is not seen in parts G and I--the zero mean images used in these calculations remove any global shift. The sign independent global hyperpolarization is clearly seen in part J of the figures. In the first 200 μs of the shock, the cross-correlation shows nearly uniform positive values. Again, the cross-correlations shown in part K do not reflect this activity. A more though analysis of the brief sign independent global hyperpolarization observed will be presented shortly.

Activation quickly comes to dominate the autocorrelations shown in parts F and H and the cross-correlations shown in part J, even though structure is easily seen in the fluorescence data. As noted earlier, a hyperpolarization of -0.2 is large in this preparation. Therefore, the difference between resting tissue and a virtual anode is small in terms of S1 amplitude. This same effect was illustrated in figure 7.2. It is clear, for example, in Figure 7.3 that the positive polarity shock (F) has slower activation than the negative polarity (H). It can be seen in the fluorescence data that the virtual anodes in part D persist longer and are of greater spatial extent than those in part E. This is reflected in the corresponding autocorrelations in parts F and H. The effect is less pronounced in figure 7.4, but is still clearly visible in the data.

In all four preparations there are clear negative cross-correlations seen in parts J and K in the second 200 μs interval of the shock. This is indicative of a spatial reversal of virtual cathodes and virtual anodes upon reversal of shock polarity. In all preparations, a central negative region persists well beyond the end of the shock for the cross-

correlation shown in part K. The central negative region is more prominent for RV1 and RV2 due to the larger virtual anodes. Even though the tissue appears to be nearly uniformly activated 0.8 ms after shock termination (frame 16), there are still significant polarity dependent differences in V_m distribution visible in the cross-correlations shown in part K for all preparations.

Figure 7.7 shows an exhaustive cross-correlation within the sequence of the response of RV2 to a positive 2 ms 300V (50V/cm) shock; the data are taken from the first 8 frames of fluorescence data shown in part A of figure 7.4. The fluorescence data used were taken from a larger area (20×24 pixels) than the autocorrelations in figure 7.4. The slightly larger spatial sample was used to obtain more information. Other than the larger spatial sample, the diagonal in Figure 7.7 is simply the first eight frames of the auto-correlation shown in part F of Figure 7.4, except the *xcorr2* function is used. The shock onset is labeled 0.0. The effect of the small global hyperpolarization that occurs at shock onset is seen here as well. Comparing the frame of shock onset (0.0 ms) to later frames (0.6 ms to 1.2 ms) the broad slightly negative cross-correlation becomes larger as time progresses. This is due to the small global hyperpolarization at shock onset, and the areas of activation at the later times. There is no significant cross-correlation evident with the frame preceding the shock with any of the subsequent frames.

All autocorrelations from 0.2 ms and later show a positive central area that grows gradually when compared to more activated frames. This shows the features are anchored spatially; while the virtual anodes and activated regions do change in spatial extent, their positions remain fixed.

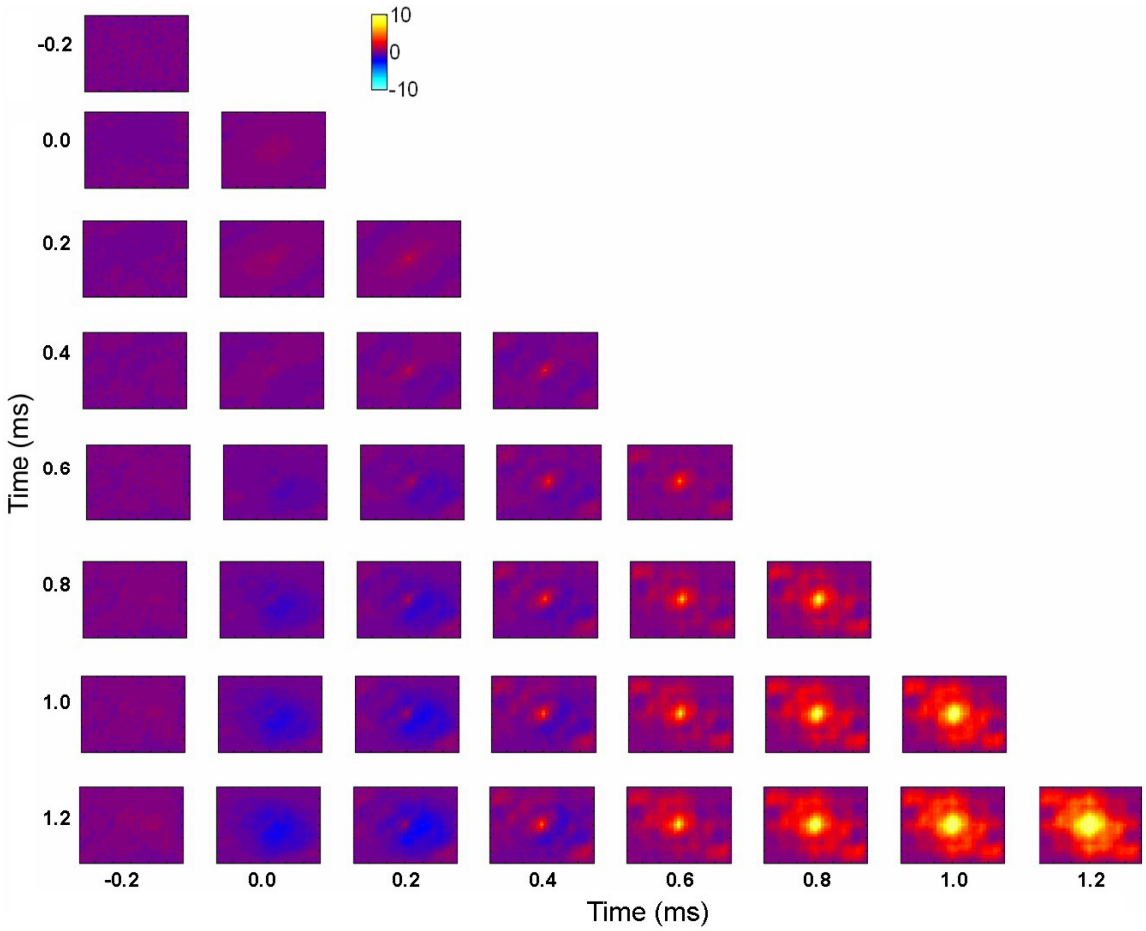

Figure 7.7. Cross-correlations (*xcorr2* method) of the positive 2 ms 300 V shock for RV2. Exhaustive cross-correlation for the frame preceding the shock (labeled -0.2 ms), and subsequent seven frames. The fluorescence data from a rectangular 20×24 region are taken on the RV to avoid the edges. The shock onset occurs at 0.0 ms.

Figure 7.8 shows and exhaustive cross-correlation between corresponding sequences of the response of RV2 to 2 ms 300V (50V/cm) shocks of both polarities. The data are taken from the first 8 frames of fluorescence data shown in parts A and B of Figure 7.4. Other than the larger spatial sample, the diagonal in Figure 7.8 is simply the cross-correlation shown in Figure 7.4 part J for the first eight frames, except the *xcorr2* method was used. The shock onset is labeled 0.0. The small global hyperpolarization that occurs at shock onset is manifested here as well. The cross-correlation of 0.2 ms

with all subsequent frames shows a small but sharp negative region in the center. This highlights that the initial positions of the virtual anodes at one polarity are the first positions to activate at the opposite polarity.

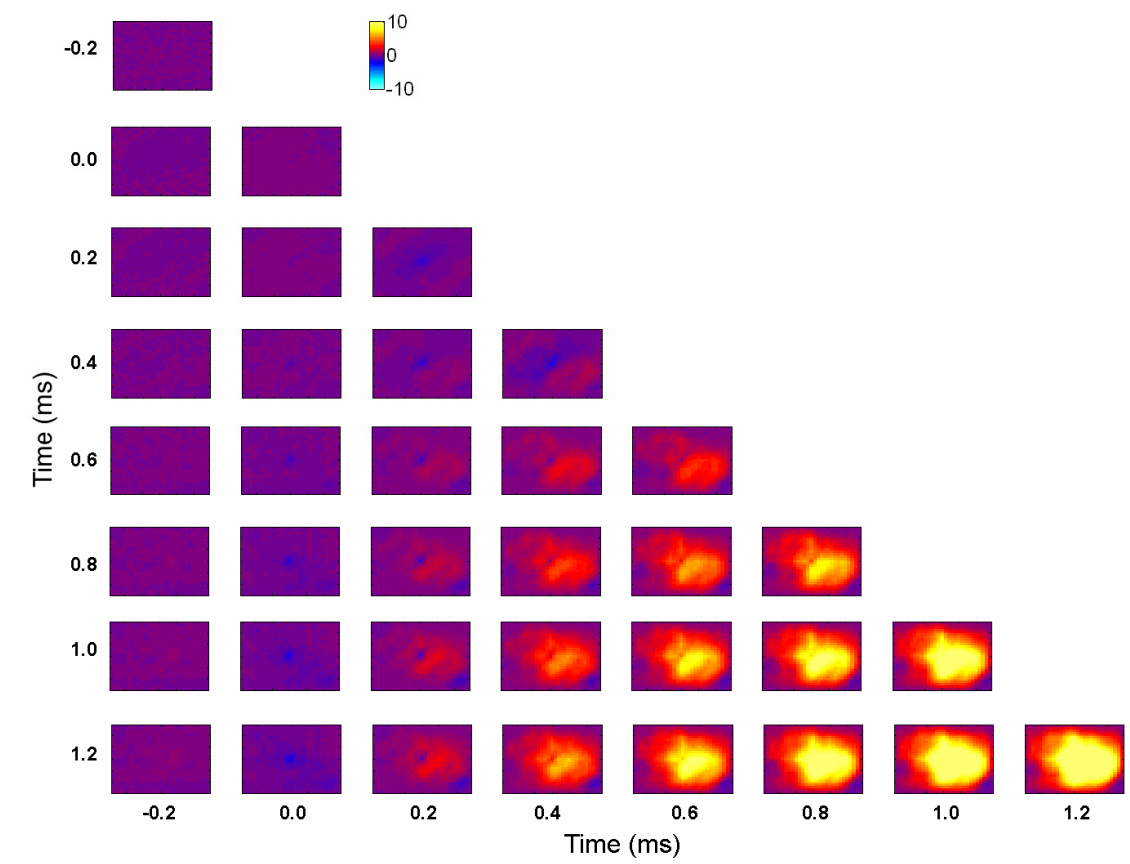

Figure 7.8. Cross-correlation (*xcorr2* method) of 2 ms 300 V shocks of both polarities for RV2. Exhaustive cross-correlation for the frame preceding the shock (labeled -0.2 ms), and subsequent seven frames. The fluorescence data from a rectangular 20×24 region are taken on the RV to avoid the edges. The shock onset occurs at 0.0 ms in both sequences.

The response of four preparations to 2 ms 50 V/cm shocks presented in this section reveal some interesting and consistent behavior. The fluorescence data and time series analysis shows that for all preparations at both polarities there is a brief (<200 μs) global hyperpolarization observed. The magnitude of this hyperpolarization and its

relationship to field strength is examined shortly. After the initial 200 μs of the shock, macroscopic virtual anodes remain, which are dispersed across the RV and remain spatially fixed. Many of the virtual anodes persist for the 2 ms duration of the shock, and some for up to 1 ms beyond the termination of the shock. The locations of the virtual cathodes and virtual anodes are exchanged upon reversal of polarity. The activated regions grow with time, and eventually the entire RV becomes activated regardless of the polarity of the shock.

7.3.2. Polarity Dependent Activation

While the shock response symmetry discussed in section 7.3.1 is clear, it is interesting to note that the activation times are not always similar for opposite polarities. The activation of tissue is delayed by the regions of hyperpolarization. Woods [31] noted in whole hearts that this effect is more prominent in the left ventricle than the right ventricle. She theorized that the thicker LV wall and slower fiber rotation were the determining factors. She observed that for longer shocks, at some point the total activation time increased due to virtual anodes.

The non-symmetric activation times are clearly illustrated by the autocorrelation data in Figures 7.3 and 7.4. Figure 7.9 shows the proportion of activated pixels for 50 V/cm shocks of both polarities for each of the four RVs. RV1 and RV2 show the greatest difference. It is easily see in Figures 7.3 and 7.4 that the virtual anodes in the positive polarity shocks persist longer than those in the negative polarity. All RVs were placed in approximately the same orientation with respect to the field, but not precisely enough to claim a specific anatomical feature is responsible. It is interesting to note that the

negative polarity produces a shorter activation time in all four preparations. A more thorough analysis of anatomical features is presented in section 7.5. It is interesting to note that the total activation time, that point where 100% of the pixels are activated, has a small difference in all preparations considering some of the large differences in the temporal trajectories. This difference would not be as clear in a slower recording. The difference in trajectory could certainly affect the post-shock dynamics because of the resulting difference in membrane state.

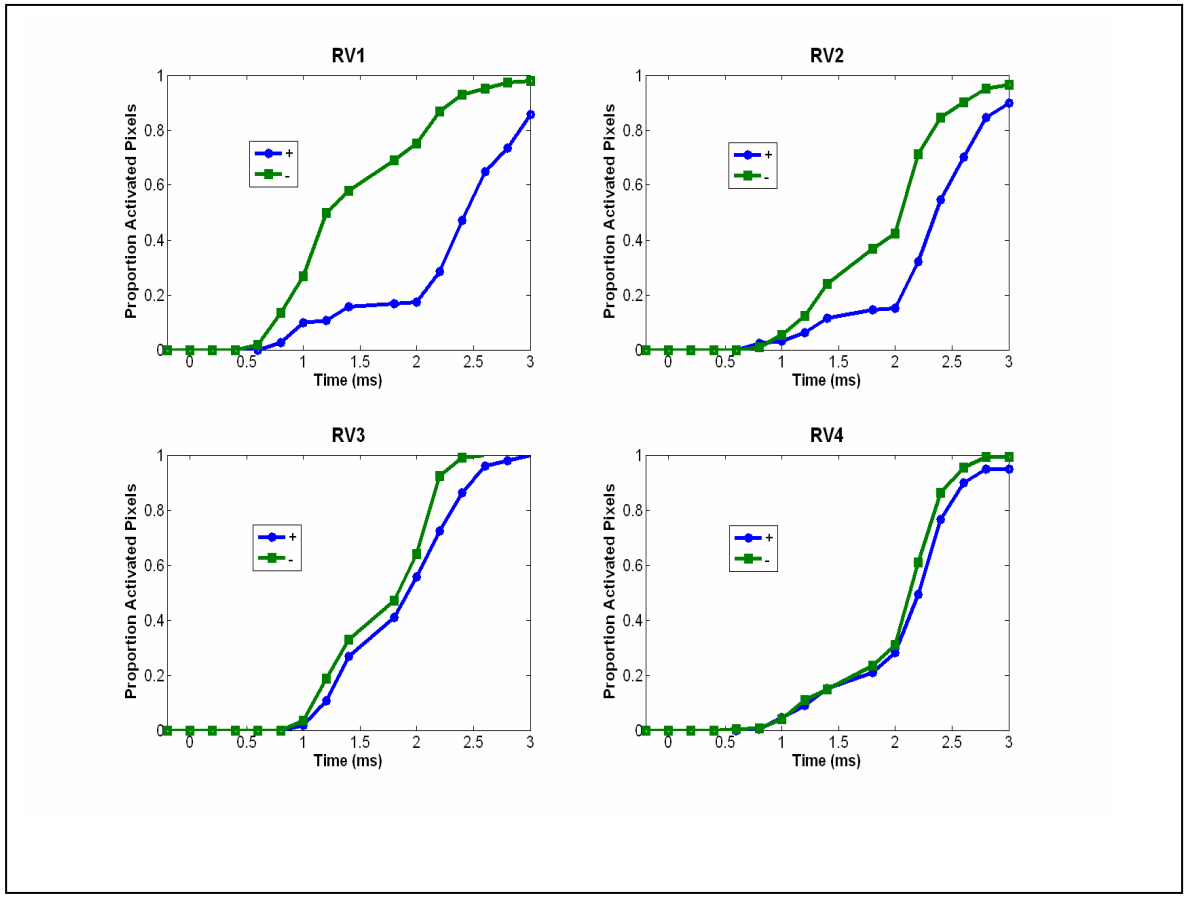

Figure 7.9. Proportion of activated pixels with time. For RV1-RV4 the proportion of activated pixels (F_{Norm}> 0.5) vs. time for a 2 ms 300 V (50 V/cm) shock that begins at 0 ms. The data are taken from the centered 16×16 pixel region in each preparation.

Figure 7.10 shows the sum of the frame products of alternate polarities for each of the RVs. Since the fluorescence signals are S1 normalized, the sum of the pixel by pixel products, effectively the dot product, illustrates the dynamics of the response to alternate polarities. At shock onset, there is a clear positive increase in RV2-RV4. This is due to the small global hyperpolarization (negative values) independent of polarity. In the subsequent frame, after the global hyperpolarization subsides, the complementary response from corresponding virtual cathodes (positive values) and virtual anodes (negative values) in all RVs lowers the sum, and as the sequences activate the sum increases. The greater hyperpolarization in RV1 and RV2 are clearly visible by the greater negative depression.

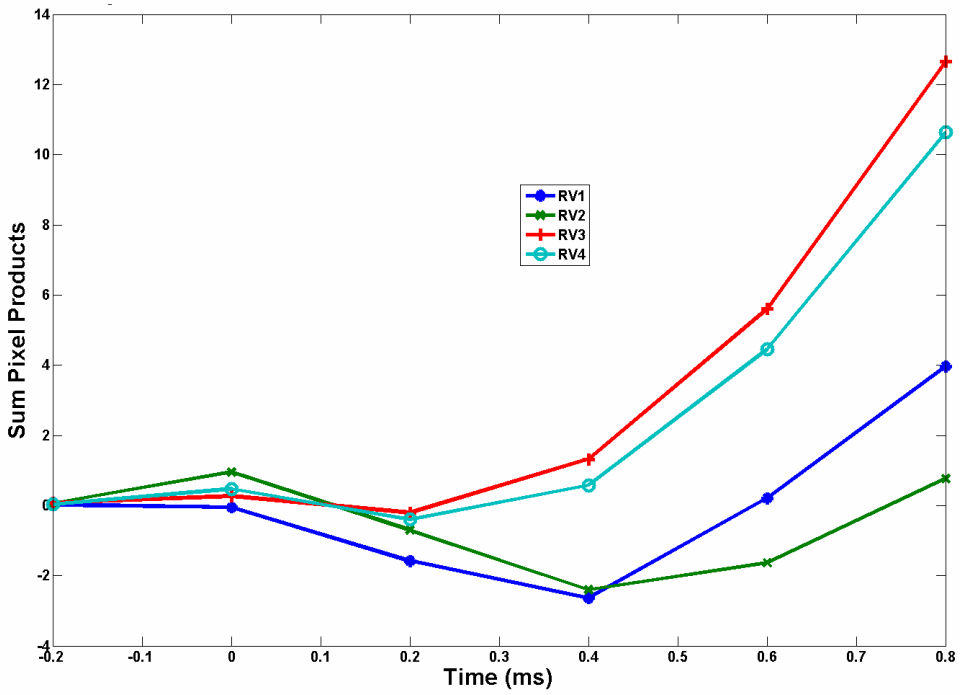

Figure 7.10. Temporal evolution of the direct frame product sum for 50 V/cm shocks. Each pixel in each frame is multiplied by the corresponding pixel in the frame sequence from the opposite polarity. The sums plotted are the sum of the products. This is equivalent of taking the dot product of corresponding images in the two sequences. The first frame reported is the frame preceding the shock.

The comparison of activation times and complementary response illustrates that while there is symmetry in the position of virtual cathodes and virtual anodes for different polarities, their affect on the activation time of the RV is not necessarily symmetric. Even though both shocks eventually lead to global activation, the resulting membrane state is clearly different due to the different extent of hyperpolarization for alternate polarities discussed earlier.

7.3.3. Hyperpolarization and Electroporation

Figure 7.11 shows the average response of a 1 cm ×1 cm region of endocardium (RV1) to three S1s, a strong S2, and subsequent S1s. Both hyperpolarization at the onset of the shock (frame 6001) and an increase in resting potential is easily seen for shocks of 300 V and greater. As described previously, there are several indicators of electroporation, but due to limitations in our pacing stimulator, the S1s immediately following strong S2s were not captured (likely due to increased threshold caused by electroporation). Therefore, the change in resting membrane potential is used as the sole indicator of electroporation in our data.

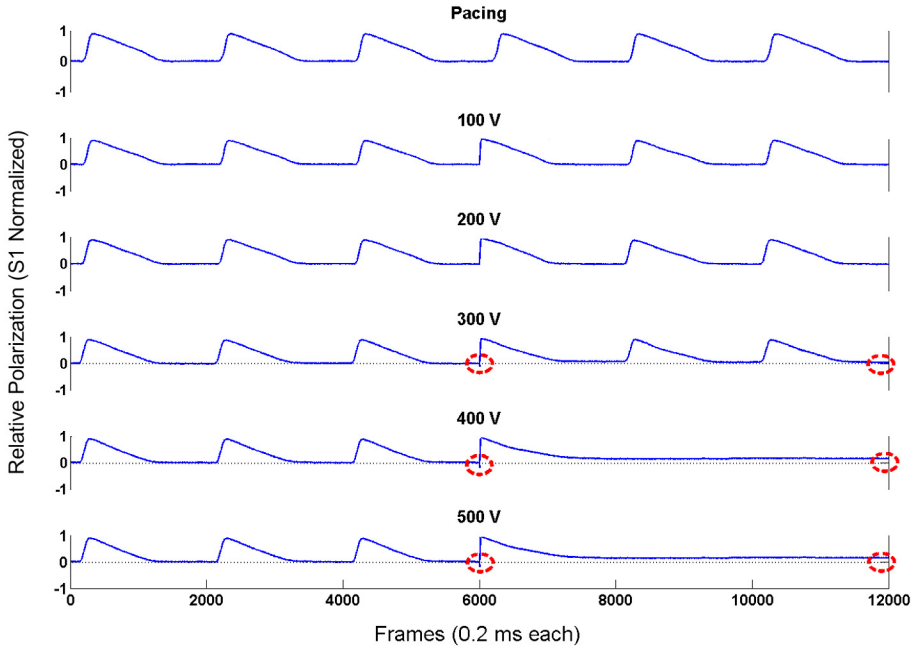

Figure 7.11. Comparison of S2 response to increasing shock strength for the same preparation (RV1). Three S1s precede the S2. The data are an average of a 1 cm × 1 cm region centered on the endocardium. In this heart, both hyperpolarization and increased resting potential following S2 are visible at shocks greater than 300 V. The 2 ms S2 shocks were delivered at the beginning of frame 6001 in each sequence. Each sequence was acquired at 5000 fps with a resolution of 26 × 26 pixels.

Figure 7.12 shows the amount of hyperpolarization and increase in resting potential is both larger for stronger shocks. Figure 7.13 and 7.14 show the degree of relative change in resting potential and hyperpolarization, respectively, for three RVs.

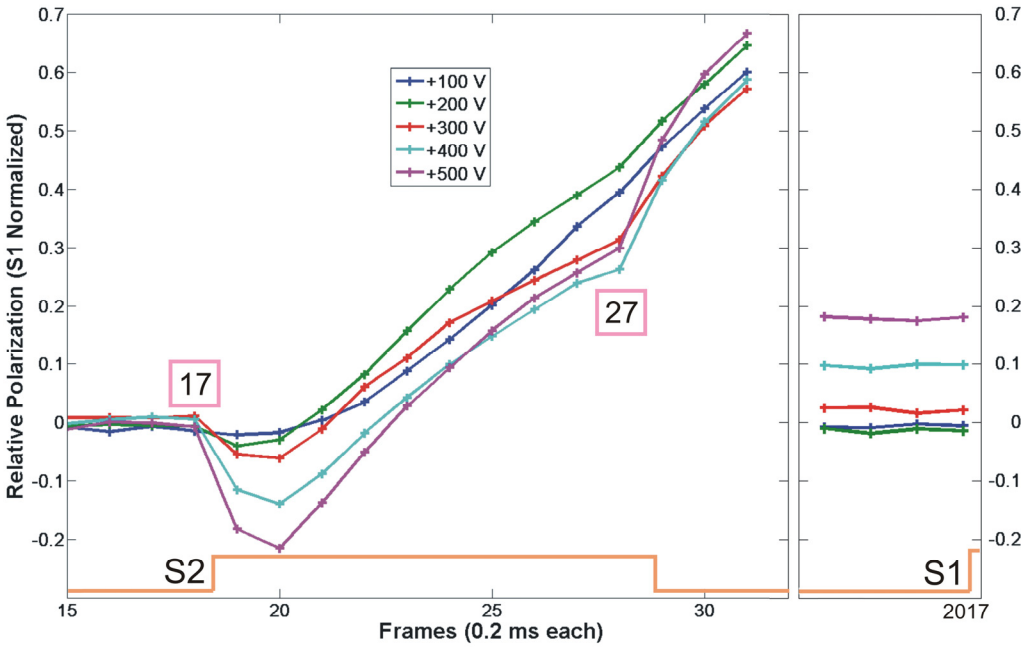

Figure 7.12. The response of an isolated RV (RV1) to 2 ms shocks of different strengths. The data are an average of a 1 cm × 1 cm region centered on the endocardium. S2 onset is at the beginning of frame 18 and terminates at the end of frame 27. Each sequence was acquired at 5000 fps with a resolution of 26 × 26 pixels. The frame capture duration is shown by the width of the frame 17 and 27 boxes.

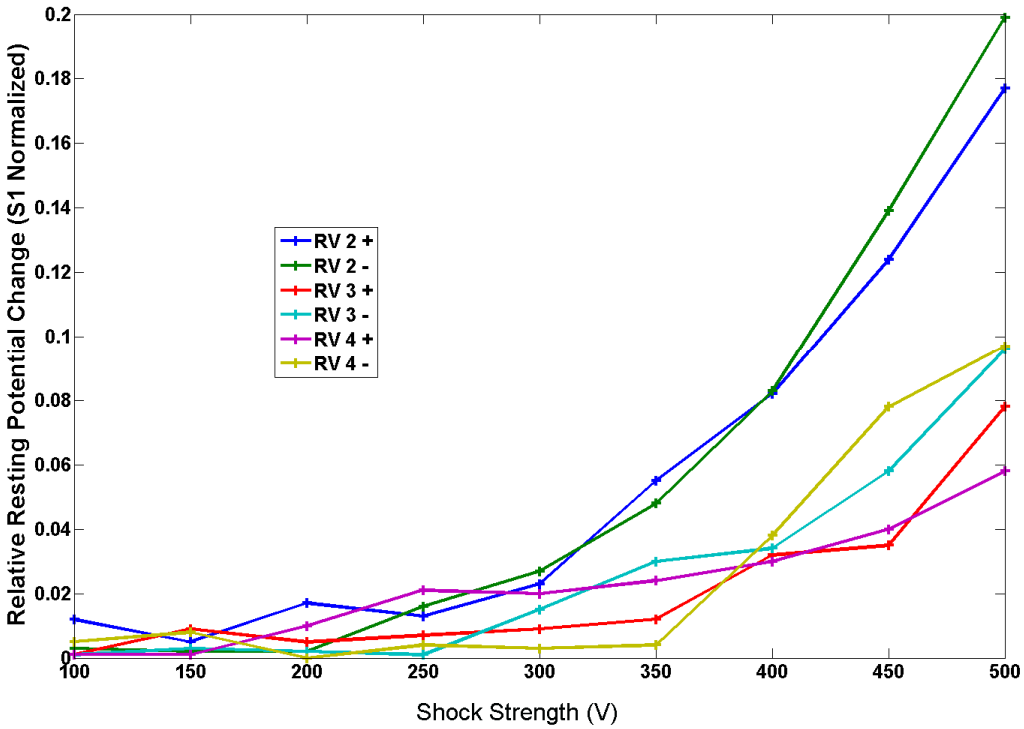

Figure 7.13. Post-shock resting potential shift attributed to electroporation. Relative change in resting potential for three RVs for 2 ms shock of increasing strengths. The data are an average of a 1 cm × 1 cm region centered on the endocardium. Each sequence was acquired at 5000 fps with a resolution of 26 × 26 pixels.

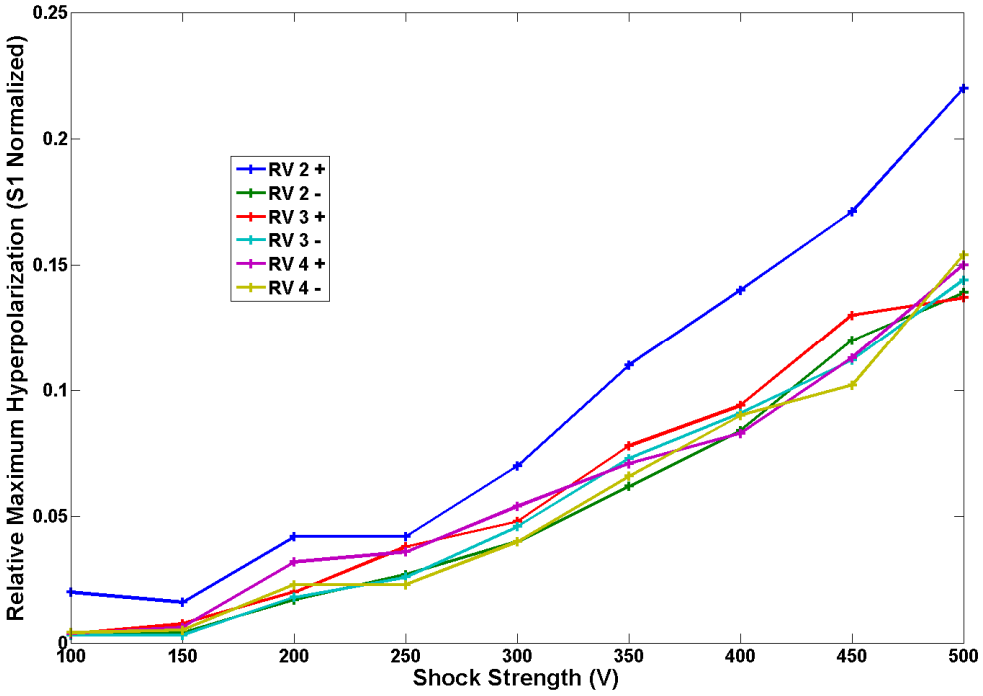

Figure 7.14. Rapid hyperpolarization after shock onset. For three RVs, the curves show the maximum relative hyperpolarization following 2 ms shock onset at different strengths. The data are an average of a 1 cm × 1 cm region centered on the endocardium. Each sequence was acquired at 5000 fps with a resolution of 26 ×26 pixels.

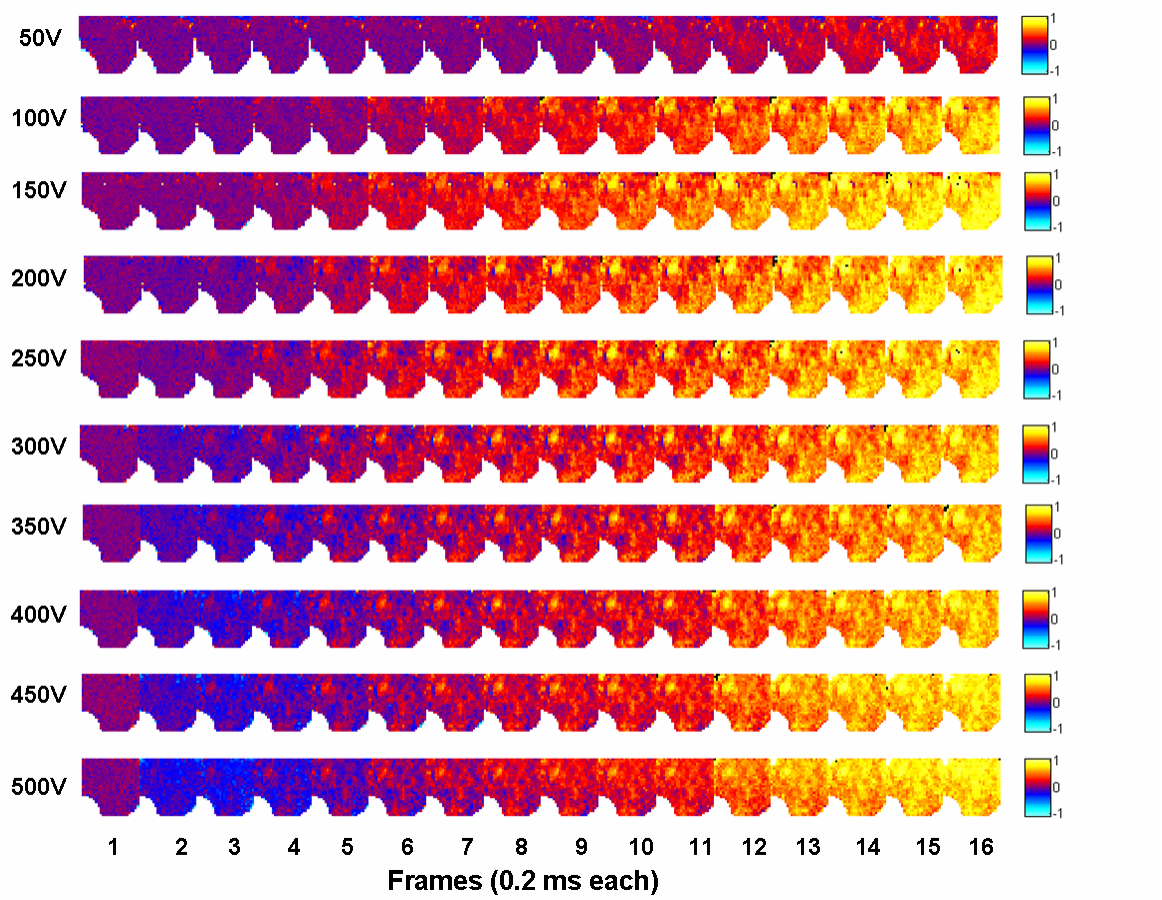

Figure 7.15. Endocardial response of RV2 to progressively stronger positive shocks. The onset of the shock occurs at the beginning of frame 2 and terminates at the end of frame 11. Each sequence was acquired at 5000 fps with a resolution of 26×26 pixels.

Figure 7.15 shows a complete positive protocol for RV2. Fast *et al.* [51] has recently reported that in a wedge preparation virtual cathodes become virtual anodes above 30 V/cm in systolic transmural field shocks. They used complimentary surface staining to show this was due to intramural virtual electrodes. We did not observe any apparent virtual anode/virtual cathode reversal in any of our preparations. Once a virtual electrode appears it changes in size and magnitude with increasing field strength, but never changes sign. As they increase in spatial extent, virtual anodes do come to

encompass the entire RV at high field strength, but we do not see a reversal of virtual cathodes and virtual anodes similar to that reported by Fast.

Figure 7.16 illustrates the relationship between the maximum hyperpolarization during 2 ms shocks and the subsequent change in resting potential. The data were taken from shocks of 300V, 350V, 400V, and 500V of both polarities for RV1-RV4. Figure 7.17 shows a complementary plot from the same dataset, but instead shows the maximum depolarization and the subsequent change in resting potential.

It is clear from figure 7.16 that resting offset is proportional to field strength. A least squares quadratic curve fit is shown. A roughly quadratic relationship between field strength and resting offset is consistent with models by Krassowska *et al*. [9-11]. Also, in these diastolic shocks resting offset appears to be relatively insensitive to maximum depolarization, very likely due to activation in the diastolic tissue. The relationship is approximately linear, and the least squares fit is shown in the figure. As stated earlier, a 16×16 pixel region centered in the field of view was used from each preparation in order to do comparisons between samples, and to ensure there is not an unusual boundary condition just outside the field of view due to ischemic tissue.

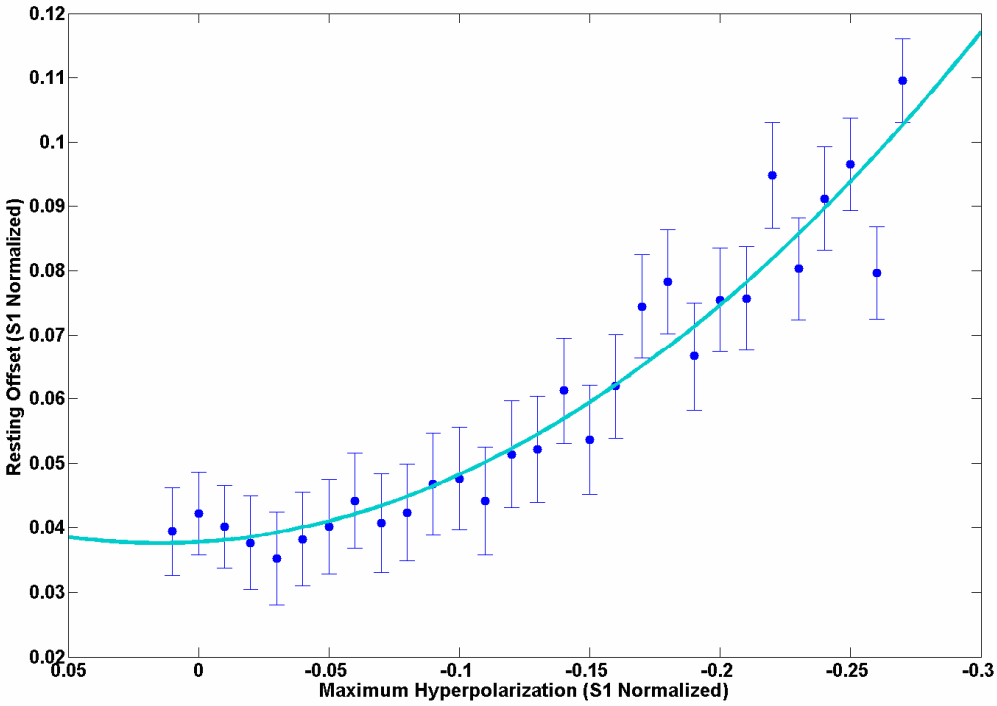

Figure 7.16. Resting offset vs. maximum hyperpolarization. The data are taken from the centered 16×16 pixel region centered in the field of view for shock strengths of 300V,350V,400V, and 500V of both polarities for RV1-RV4, during the shock. Each pixel in each shock is entered in a table along with its subsequent resting offset. A total of 5472 pixels were used. The plot is a summary of the results with a bin size of 0.01 for the hyperpolarization measurements. Only bins with counts greater than 50 are plotted. The error bars represent the standard deviation of the values in that bin. The standard deviation on the horizontal axis is on the order of the marker size due to the bin size. A least squares quadratic fit is shown.

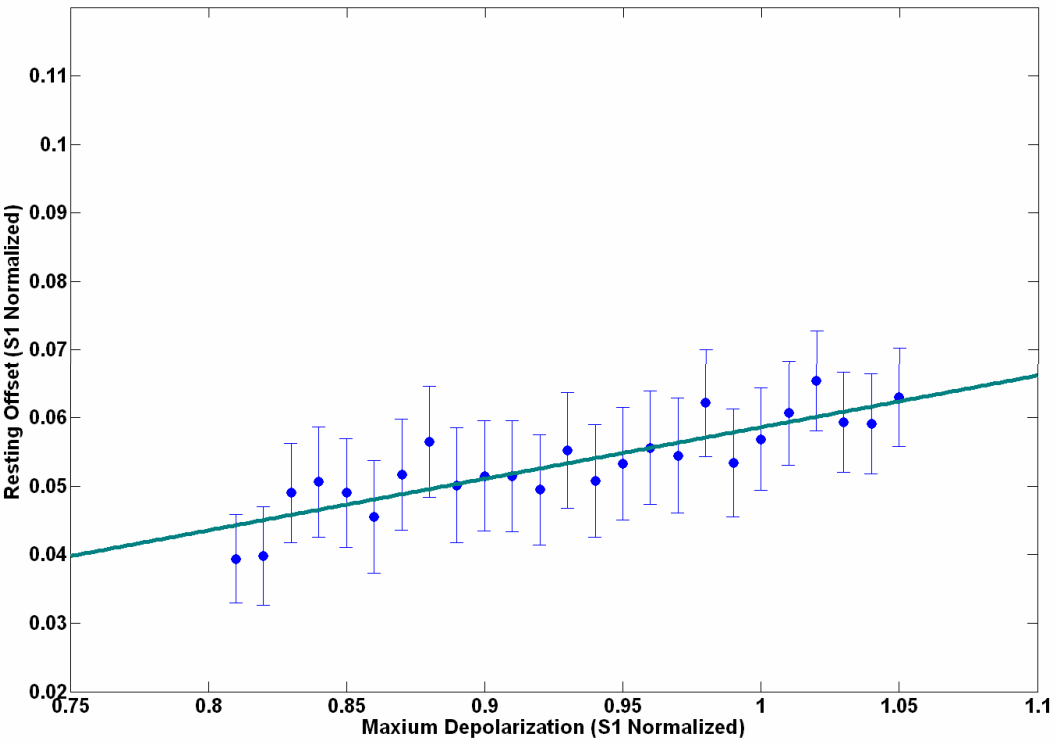

Figure 7.17. Resting offset vs. maximum depolarization. The data are taken from the centered 16×16 pixel region centered in the field of view for shock strengths of 300V,350V,400V, and 500V of both polarities for RV1-RV4, during the 2 ms shock. Each pixel in each shock is entered in a table along with its subsequent resting offset. A total of 5472 pixels were used. The plot is a summary of the results with a bin size of 0.01 for the depolarization measurements. Only bins with counts greater than 50 are plotted. The error bars represent the standard deviation of the values in that bin. The standard deviation on the horizontal axis is on the order of the marker size due to the bin size. A least squares linear fit is shown.

The analysis in this section illustrates some of the relationships between field strength, hyperpolarization, and electroporation, both at the level of the entire RV and at the individual pixel level. The noise levels in the fluorescence signal make an analysis of individual pixels in specific shocks difficult, but the statistical results compiled over many shocks give clear results.

For the entire RV, the degree of hyperpolarization and increase in resting potential are directly related to field strength. We demonstrated that electroporation increases with stronger shocks. In this preparation, for the entire RV, we define a significant change as 3% of S1 amplitude. Maximum hyperpolarization becomes significant at approximately 40 V/cm, and the change in resting potential becomes significant at approximately 60 V/cm. The 3% was chosen based on the noise levels and we are not asserting there is a linear proportionality to the quantities by comparing them in this way. It does give the field strengths where the phenomena become significant in the fluorescence data.

On the level of individual pixels, it is seen that for multiple RVs and shock strengths, there is a clear and consistent relationship between hyperpolarization and electroporation at the individual pixel level. The relationship between hyperpolarization and resting offset appears to be approximately quadradic, which is consistent with models [9-11]. The insensitivity of resting offset to maximum depolarization is expected due to tissue activation. As noted earlier, the spatial extent of one pixel in this protocol is approximately 0.8 mm square. There are almost certainly interesting dynamics in the spatial scale of one pixel, and a follow-up study using a much smaller field of view would further aid in the interpretation of these results.

7.3.4. Ancillary Procedures

Upon completion of *Protocol 1* for RV1, a 4 ms 400 V shock was applied in systole. Parts A and B of Figure 7.18 show the response. The shock onset occurs at the beginning of frame 2. Part A uses the two frames preceding the shock as a baseline, and

the data are not normalized. Part B shows the S1 normalized data with resting tissue taken as the baseline. Note the tissue is completely activated at the time of shock onset. The entire RV slightly depolarizes, but even more interesting, the virtual cathodes appear in the same locations as in the 2 ms 400 V diastolic shock shown in part C. This supports our hypothesis that, in this preparation, the fiber geometry, not the membrane dynamics, is the determining factor in VEP location.

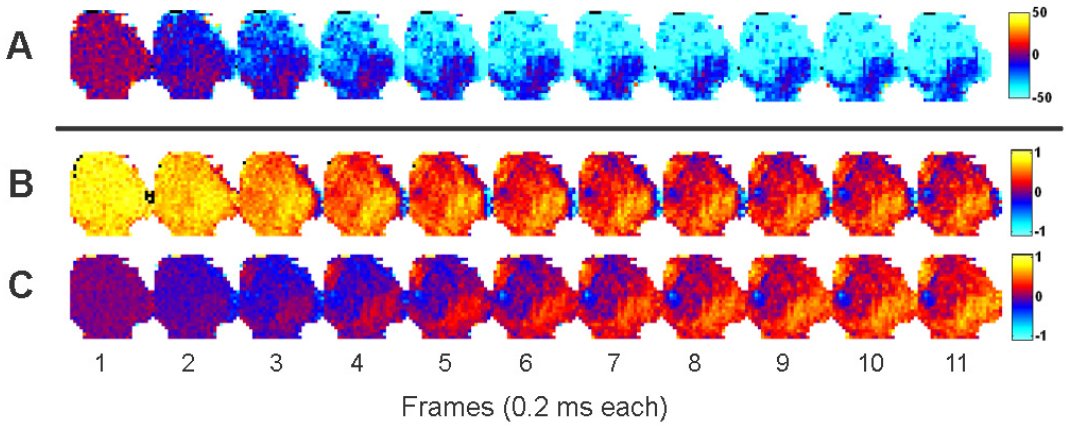

Figure 7.18. Comparison of systolic and diastolic shocks. (A) The response of RV1 to a 4 ms 400 V positive systolic shock. The two frames preceding the shock are use for the baseline. The color scale is ΔF/F. (B) The same data shown in A, but normalized and shown with respect to resting tissue. (C) The response of RV1 to a 2 ms 400 V positive diastolic shock. The shock onset is at the beginning of the second frame. Each sequence was acquired at 5000 fps with a resolution of 26×26 pixels.

Upon completion of *Protocol 1* for RV2, a 200 μs 500 V shock, and a 10 ms 500V shock were applied in diastole, with appropriate delays between them. The sequence for the 200 μs shock is shown in Figure 7.19. The entire shock is contained in the second frame. No increase in resting potential was detected following this shock.

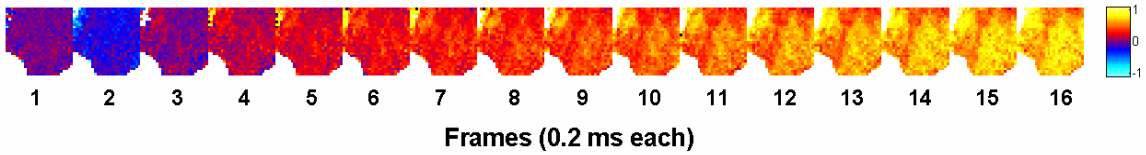

Figure 7.19. Response of RV2 to a 200 µs 500V shock. The shock onset is at the beginning of the second frame. The entire shock is contained in frame 2. The sequence was acquired at 5000 fps with a resolution of 26×26 pixels.

Figure 7.20 shows the trace of the response of RV2 to a 10 ms 500V positive shock. The increase in resting potential is very large in comparison to the 2 ms shocks presented earlier.

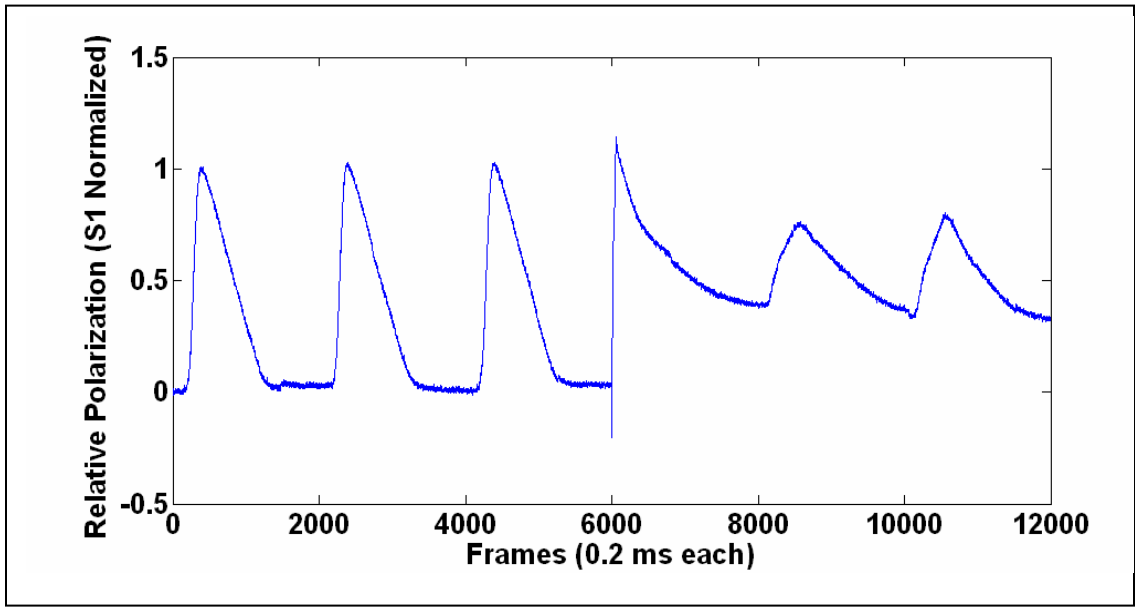

Figure 7.20. Response of RV2 to a 10 ms 500V shock. Three S1s precede the S2. The data are an average of a 1 cm × 1 cm region centered on the endocardium. The 10 ms 500V shock was delivered at the beginning of frame 6001. The sequence was acquired at 5000 fps with a resolution of 26×26 pixels.

These two observations for different shock durations are consistent with models [9-11] which predict that electroporation is a function of time as well as field strength.

The data from the ancillary protocols also serves to put the other results in context and further serves to characterize this preparation.

7.3.5. Global Hyperpolarization

As mentioned previously, there appears to be a brief shift of all pixels toward hyperpolarization at the onset of strong shocks. This is seen for 50 V/cm shocks in Figures 7.3-7.6. The entire RV seems to briefly hyperpolarize for strong shocks. Figure 7.21 shows a frame by frame histogram of the normalized data from 500 V shocks of both polarities of RV1. The bin size is 0.05. The frame with the highest percentage of pixels below resting occurs at shock onset (labeled 0.0 ms in Figure 7.21) for both polarities. In this frame, of the 599 pixels used, 586 (98%), and 570 (95%), are below resting for the positive and negative polarities, respectively. Additionally, only 1 pixel is above resting in this frame for the positive polarity, and 9 pixels above resting for the negative polarity. Similar results were obtained from the other RVs.

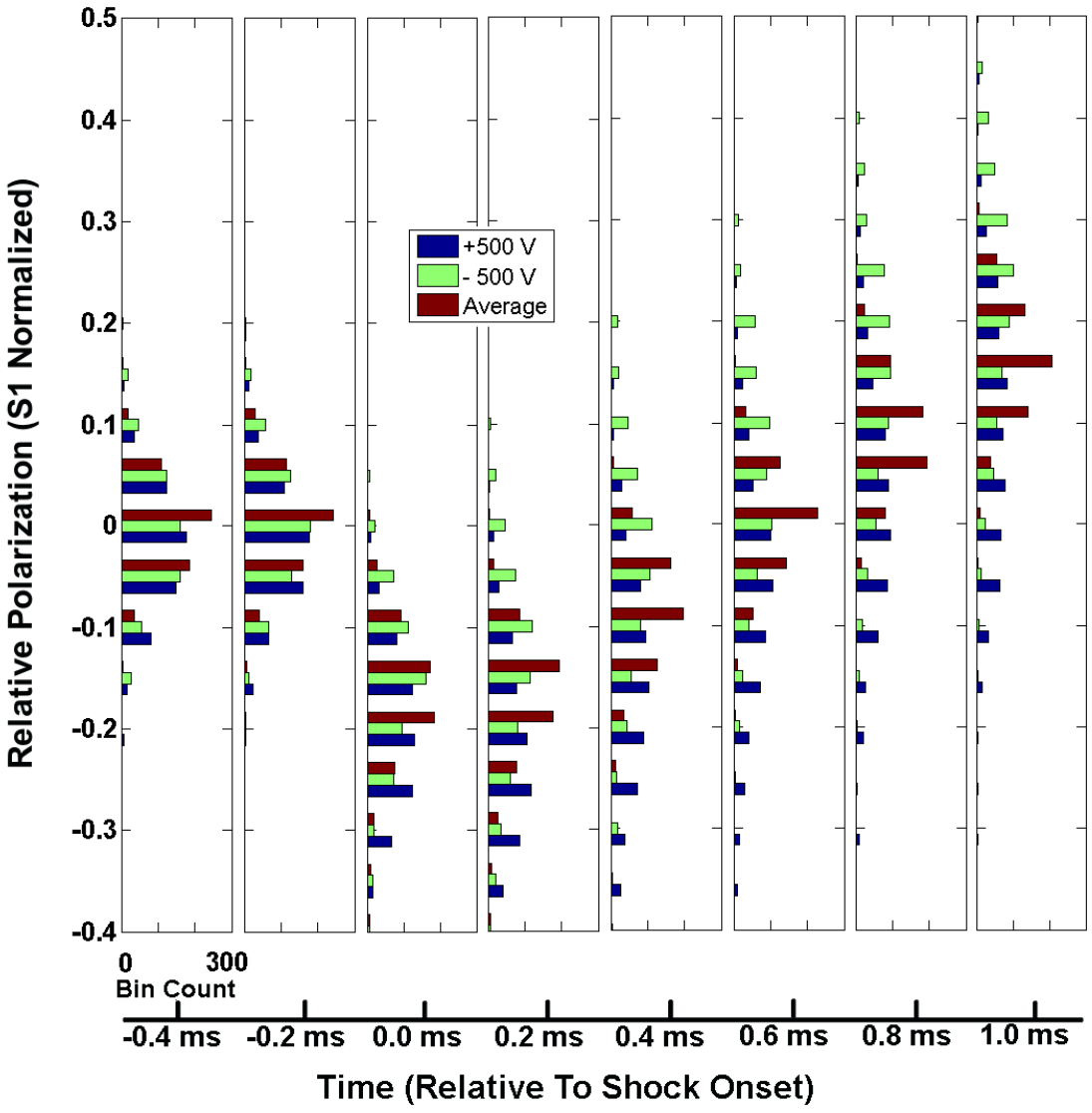

Figure 7.21. Distribution of individual pixel values during global hyperpolarization of a 2 ms 500 V shock. Frame by frame histogram of the normalized image sequences from RV1. The bin size is 0.05.

Figure 7.22 A and B show the response of RV1 to positive and negative polarity 500 V shocks, respectively. Parts C and D are the cross-correlations using the NSDP and ZMNSDP methods, respectively. The shock onset occurs at the beginning of the third frame. Note there is no apparent structure in either of the correlations preceding the

shock. The first frame of the cross-correlation shown in part C shows a uniformly positive distribution of values nearly equal to 1. This indicates the observed V_m distributions in response to the two shock polarities are almost indistinguishable in that 200 μs interval. As noted earlier, the global hyperpolarization is not apparent in the cross-correlation shown in part D. In part D, the frame corresponding to shock onset is only slightly different than the two frames preceding the shock which correspond to resting tissue, but there is a very small indication of a symmetric reversal. This further illustrates the sign independence and global nature of the effect. As time progresses, a central negative portion develops in part D that indicates the regions of activation and hyperpolarization are opposite for opposite polarities, as discussed previously. For comparison, figure 7.4 shows the same for 50 V/cm shocks. It is interesting to note that the global hyperpolarization indicated in figure 7.22 part C appears to have some small affect beyond the first frame of the shock.

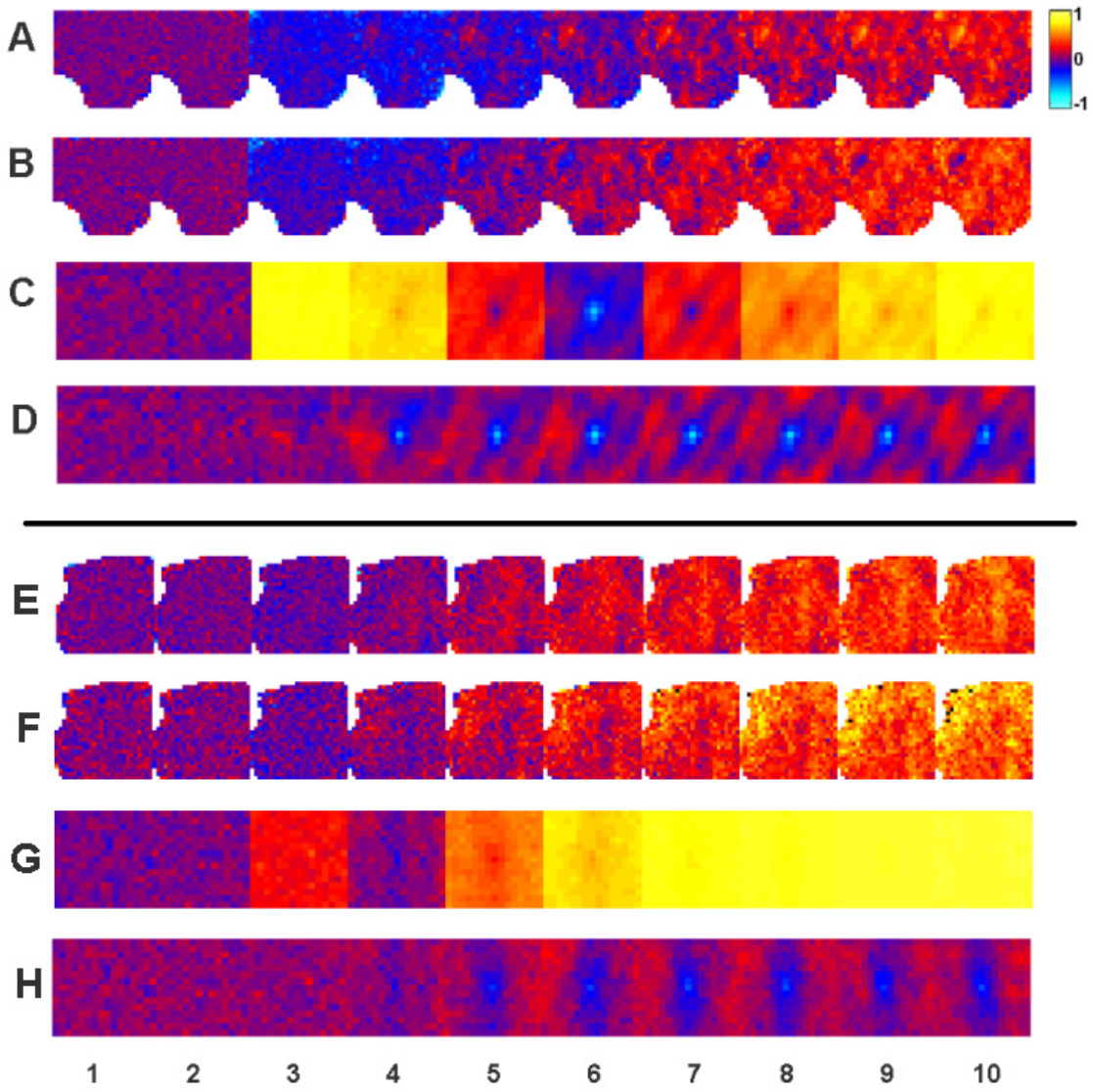

Figure 7.22. Strong shock correlations. (A) and (B) show the response of RV2 to2 ms 500 V (83.3 V/cm) positive and negative polarity shocks, respectively (C) and (D) show the cross-correlation of A and B using the NSDP and ZMNSDP methods, respectively. (E) and (F) show the response of a RH-237 stained RV preparation to 2 ms 500 V (83.3 V/cm) positive and negative polarity shocks, respectively. (G) and (H) show the cross-correlation of E and F using the NSDP and ZMNSDP methods, respectively. Each sequence was acquired at 5000 fps with a resolution of 26×26 pixels. The onset of the shock occurs at the beginning of frame 3.

To rule out the possibility of electromagnetic coupling between the imaging system and stimulator, we recorded image sequences while viewing a fluorescent target through the transparent bath while it was filled with perfusate. The laser illumination,

stimulator, bath, and filters were identically configured to those in the RV experiments. The change in fluorescence of the target was approximately 0.02 % greater than the average fluorescence of the fifty frames that preceded shock onset. The change in raw fluorescence of the frame containing the onset of the 500 V shock for RV2 is an increase of approximately 2% over the average of the previous fifty frames. This experiment was repeated four times at alternating polarity with similar results. This is a strong indication that the observed global hyperpolarization is not simply electromagnetic interference between the camera and stimulator.

As shown in Figures 7.12 and 7.14, the central region of the field of view experiences an average hyperpolarization that increases with shock strength. This effectively has two contributions: The first and most obvious contribution is from the macroscopic virtual anodes that persist for up to several ms beyond shock onset. The position of the virtual anodes, as has been shown, is sign dependent. The second contribution is from the shift of every pixel toward hyperpolarization during the first 200 μs of strong shocks that is sign independent.

The brief global hyperpolarization observed is unexpected. Di-4 is a polar dye. We stained a preparation with RH-237, a non-polar dye, and applied shocks of 300 V, 400 V, and 500 V of both polarities to the preparation. Figure 7.22 parts E and F show the response of the RH-237 stained RV to 500 V shocks of both polarities. The cross-correlation in G does indicate a small, somewhat uniform shift towards hyperpolarization, but nothing to the degree seen in part C or the other di-4 preparations. The cross-correlation shown in part H indicates the reversal of virtual cathodes and virtual anodes for opposite polarities in a way similar to what is observed in the di-4 preparations. We

did not see the same global hyperpolarization in response to any of the shocks that was observed in all the di-4 preparations. Even during the strongest shocks, at least 30% of the pixels in the RH-237 stained heart remained greater than or equal to zero. This suggests that the global hyperpolarization is caused by an interaction of di-4 and the external electric field rather than a global membrane hyperpolarization. Di-4 is one of the most commonly used voltage-sensitive dyes. The results and conclusions in studies where high strength electric fields are applied, by either field shock or electrode, may need to be reevaluated. The RH-237 stained heart did exhibit virtual anodes that lasted the duration of the 2 ms shock. This is consistent with the di-4 stained hearts. Therefore, this discrepancy does not invalidate the results obtained for hyperpolarization, but does cast doubt on the global hyperpolarization. There is a clear discrepancy in the results given by the two dyes, which by itself is a significant observation—At least one of the dyes is giving inaccurate results.

7.4. Protocol 2

Three successful preparations were used in this protocol, denoted RV5-RV7. *Protocol 2* was designed to examine the difference in activation times between the endocardium and epicardium. The endocardium has many more macroscopic surface heterogeneities than the epicardium. One would expect this increase in heterogeneity to cause shorter activation times. It has been reported previously that in a similar preparation the endocardium activates sooner than the epicardium in response to field shock [52]. We define activation as the time when every pixel in the region of interest has reached 50% of the previous S1 amplitude. We saw no significant or consistent

difference in activation times. For three RVs (RV5-RV7) both sides of the RVs were imaged. RV6 was oriented endocardium facing the holder; the other two were oriented epicardium facing the holder. Figure 7.23 shows the activation times for three RVs. Figure 7.24 shows the difference in activation times (Endocardium minus Epicardium).

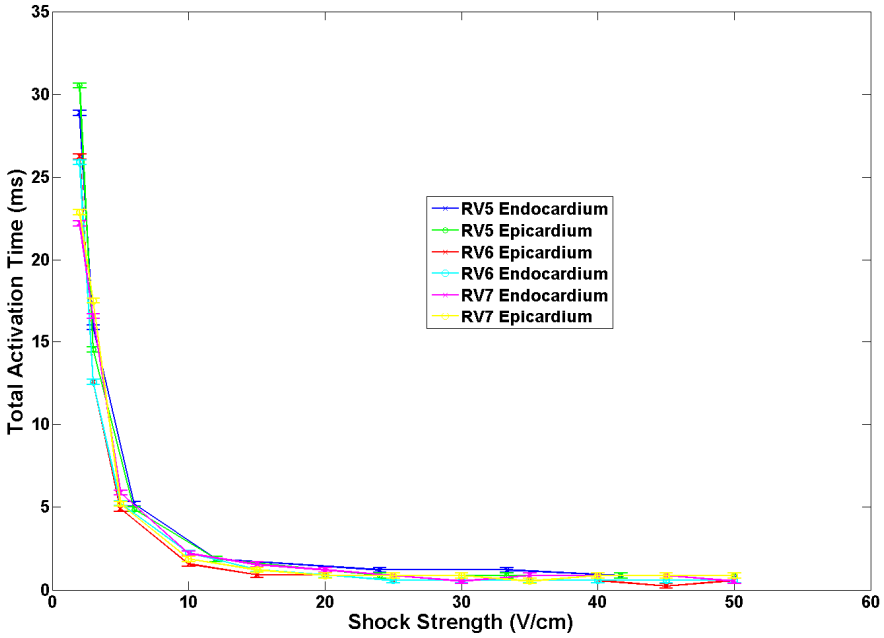

Figure 7.23. Endocardial and epicardial activation times. The data is from a 1 cm × 1 cm region centered on the RV. Data were collected at 3000 fps with a resolution of 40 × 40 pixels

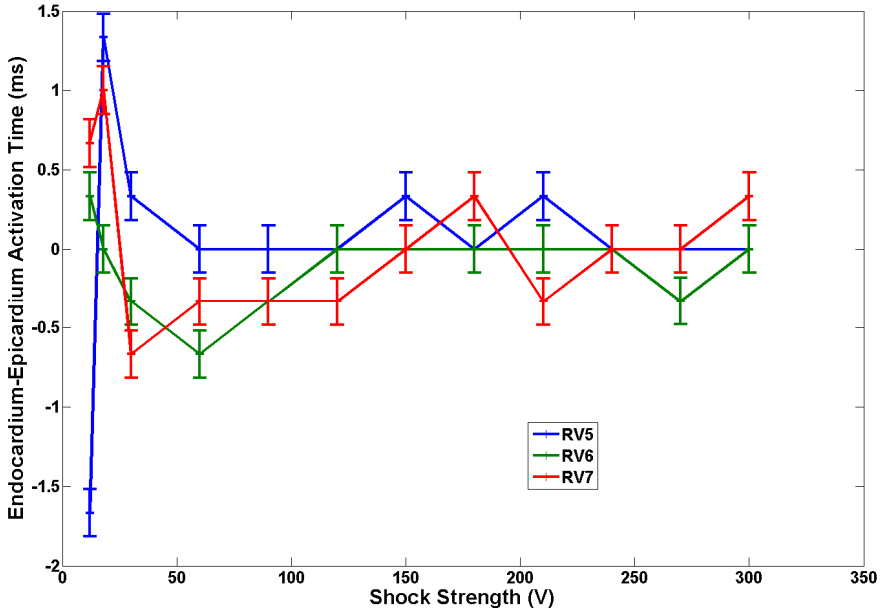

Figure 7.24. Activation time differences. The difference in activation times (Endocardium minus Epicardium) for increasing shock strength. The data is from a 1 cm × 1 cm region centered on the RV. Data were collected at 3000 fps with a resolution of 40 × 40 pixels

One possible explanation for the lack of difference detected is the thin RV, which for our preparations is approximately 1 mm thick. The more numerous heterogeneities of the endocardium may give rise to more points of activation, but our region of interest is 1 cm × 1 cm which is very large compared to the depth. The initial wavefronts can also travel traverse to the surface, which may lead to nearly identical activation times. The thinness of the RV also makes it somewhat translucent, and therefore the signal measured on one surface is not independent from the signal on the opposite surface.

Figure 7.25 shows both endocardium and epicardium pacing data taken in *Protocol 3* from RV10. It is clear there are more points of activation on the endocardium in each orientation. Using the criteria introduced earlier, the differences in activation times are 0 ms, 2 ms, 1ms, and 1 ms, with the endocardium having the shorter activation

time when a difference is detected. These pacing stimuli are near threshold, therefore macroscopic virtual anodes are not produced which normally affect activation. Nevertheless, these results buttress our original hypothesis that the more heterogeneous endocardium has more points of activation. Similar results were obtained for the other two preparations used in *protocol 3*

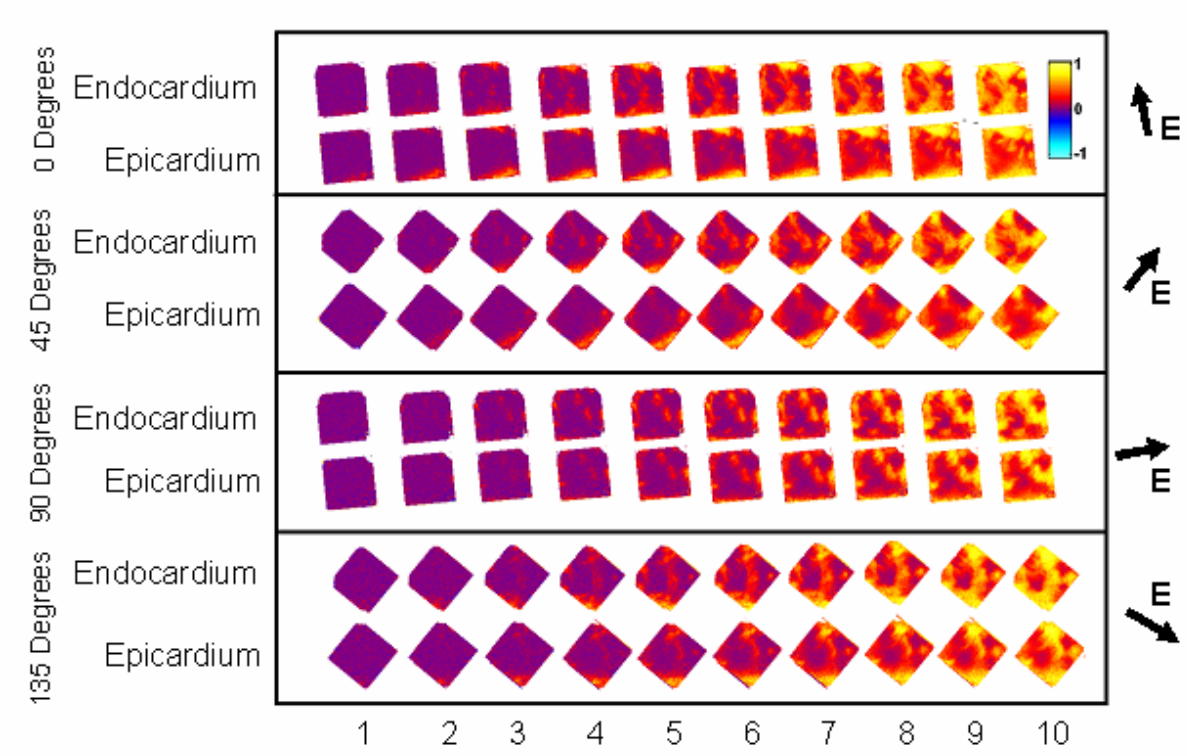

Figure 7.25. Pacing response of RV10 in different orientations. Pacing response of RV9 at angles of 0, 45, 90, and 135 degrees with respect to the original orientation. The pacing electric field in each case is right to left. The pacing stimulus terminates approximately 2 ms before frame 1 in each sequence. The data were acquired at 1000 fps with a resolution of 80×80 pixels. All images were rotated into the same orientation as the DTMRI data shown in figures 7.26 and 7.27.

7.5. Protocol 3

Three successful preparations were used in this protocol. Figure 7.26A shows an anatomical MRI of RV10. The lighter regions roughly correspond to greater tissue

density. Figure 7.26 parts B and C show white-light images of the endocardium and epicardium, respectively, taken with the acquisition cameras. The red outline in part A corresponds to the field of view in parts B and C. The anatomical scan was used for image registration for each of the four physical angles fluorescence data were taken. The images in parts B and C, for example, were taken at the original orientation, 0 degrees, but are rotated in the figure -84.3 degrees and spatially resampled to match the anatomical scan.

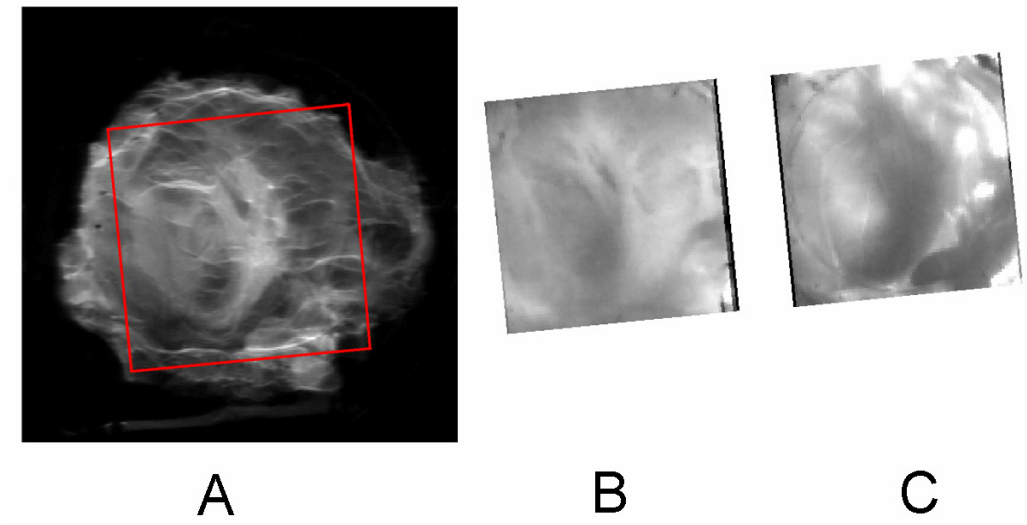

Figure 7.26. (A) An anatomical MRI of RV10. The lighter portions roughly correlate to greater tissue density. (B) White-light 80×80 pixel image of the RV10 endocardium. (C) White-light 80×80 pixel image of the RV10 epicardium. Part C is left-right reversed.

Figure 7.27 shows the DTMRI data in RGB format. The images are oriented identically to anatomical scan and white-light images shown in Figure 7.26. The trabecula structures seen in part B of figure 7.26 are easily seen in the first three frames of the DTMRI data. The fiber direction is primarily along the length of the trabecula

which is expected. The more vertical structures appear as bright red, and the structure that runs approximately 45 degrees appears yellow.

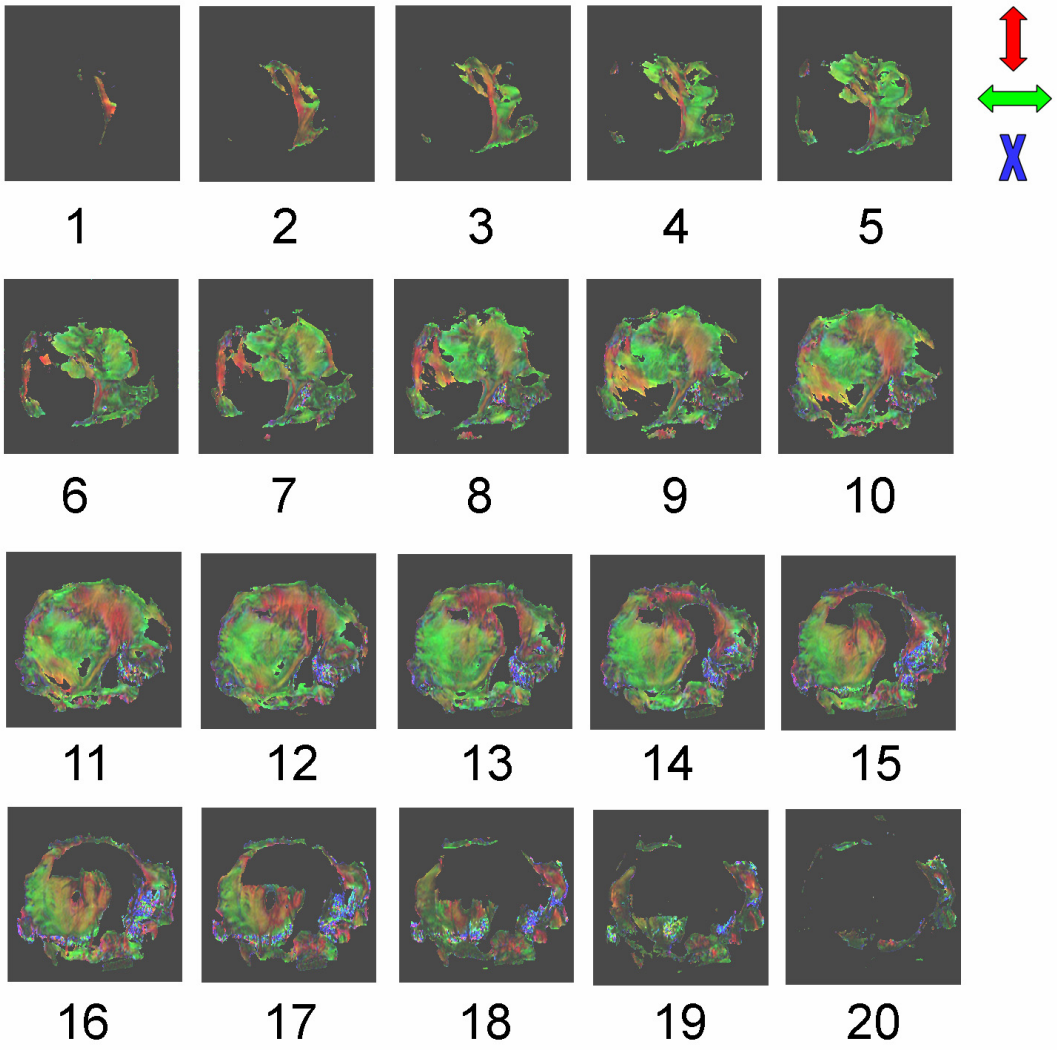

Figure 7.27. RBG images of DTMRI of RV10. Image 1 corresponds to the first slice on the endocardium, and progresses through the tissue to the epicardium. The color scale is indicated, red-vertical, green-horizontal, and blue-traverse to surface. The resolution of the scan is 281 μm vertical, 167 μm horizontal, and 188 μm traverse to the surface. Black areas are regions where no signal or no fractional anisotropy was detected.

A general rotation from primarily a horizontal direction to the vertical direction is clearly visible. The rotation appears to be at different rates—the more dense structure in the upper right appears to rotate faster than the rest of the tissue. It is unknown to what

degree the voids seen in frames later than 10 are real. It is thought a region of air or water caused the voids. For example, it is clear the semi-circular void in frame 17 is artificial. Despite the less than definitive results of this DTMRI scan, it does validate the procedure and highlights the rich structure of the RV.

Figure 7.28 shows the frame response of RV10 to 2 ms 60 V/cm shocks. The heart was rotated to 0, 45, 90, and 135 degrees with respect to the original orientation, where shocks of both polarities were applied. The frames shown are the first frame of the shock. The VEP patterns are easily seen, and change significantly with rotation. Parts C and D show the resting V_m 350 ms after the shock, which indicates electroporation. The patterns of electroporation also change significantly with rotation. In the third column, the change in resting appears to shift slightly toward hyperpolarization. This is most likely due to an artifact such as an intensity change of the laser. The edges of the preparation are predominantly hyperpolarized. This is probably due to these areas being cut, or possibly a contribution is made by the dye artifact discussed earlier.

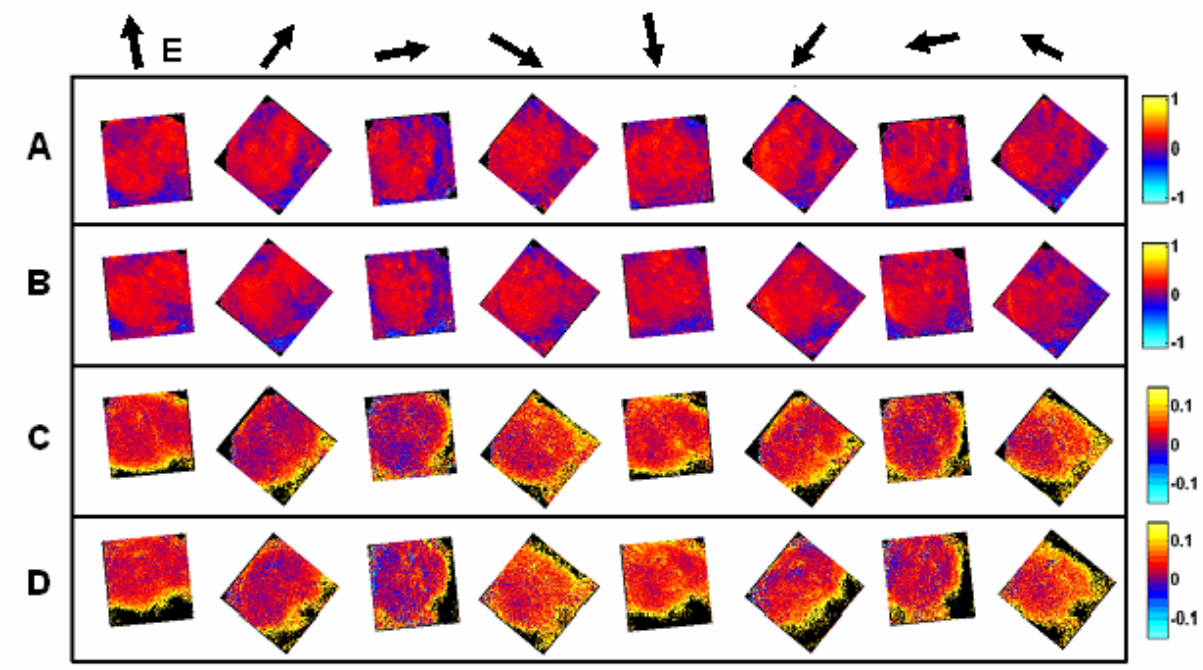

Figure 7.28. Shock response and subsequent resting offset of RV10 to 2 ms 60 V/cm shocks. (A) and (B) show the fluorescence endocardial and epicardial response in the frame of shock onset. (C) and (D) show the resting potential 350 ms after the shock. The data are acquired at 1000 fps at a resolution of 80×80 pixels. The images were rotated into the same orientation as the DTMRI data shown in figures 7.26 and 7.27. The direction of the electric field is indicated for each orientation.

It was our goal to show the locations of VEP and electroporation could be correlated to the fiber direction obtained from the DTMRI. There is no evident correlation between the first or second derivative of the fiber curvature with respect to the electric field in our analysis. The relationship is most likely more complicated than our original hypothesis [30]. Sobie *et al.* [53] have derived a generalized activating function for predicting virtual electrodes.

In retrospect, the selection of the high spatial resolution camera mode was a poor choice. There could be VEP structure that is not visible in the data that would support our original hypothesis. In future experiments one of the high speed acquisition modes

should probably be used. It is very expensive to acquire the DTMRI data, approximately $1600 for the one performed. The artificial voids make analysis more difficult. A refinement of the procedure can probably make future data more useful. A lower resolution DTMRI scan would be less expensive and could still be useful in future studies.

7.6. Conclusions

We have shown that this novel flattened rabbit right-ventricle preparation is an excellent testbed for investigations into the relationship between an externally applied electric field and intact diastolic cardiac tissue with the curvature removed. A better understanding of this relationship is of paramount importance to understanding the mechanisms of defibrillation and hence in the effective treatment of life-threatening arrhythmias. In addition to the RV preparation, the software and instrumentation presented in earlier chapters enables protocols that have precise control of experimental variables, particularly shock and camera synchronization, which make exact repeatability possible. Without exact repeatability some of the phenomena would not be as clear, or might have been overlooked entirely.

We found a striking symmetrical reversal of hyperpolarization and depolarization for shocks of opposite polarities. This reversal is usually not seen in diastolic tissue because activation obscures the effect. The ability to do frame by frame comparisons in 200 μs steps allowed us to observe this effect consistently even to the spatial resolution of an individual pixel. By doing a complimentary systolic shock, we reported evidence that this symmetric reversal is due to the interaction of fiber geometry and field direction

rather than membrane dynamics. We discovered that despite symmetric reversal of the virtual cathodes and virtual anodes for opposite polarities, the activation times are not always symmetric, with alternate polarity shocks sometimes giving very different temporal trajectories of activation primarily due to the differences in duration of some virtual anodes.

We validated model predictions by showing a clear relationship between hyperpolarization and electroporation in intact diastolic tissue. Furthermore, we showed that the degree of hyperpolarization is directly related to the maximum hyperpolarization both at the level of individual pixels and for the entire RV surface. We illustrated, with single acquisitions, that electroporation is dependent on duration of shock as well. We showed the locations of activation and hyperpolarization remain fixed from low to high strength shocks which implies that electroporation is not the determining factor in the location or size of virtual electrodes in this preparation.

We discovered a previously unknown di-4 artifact under high field strength and thoroughly documented the behavior. An apparent small global hyperpolarization seen in the first few hundred microseconds of strong shocks in every preparation is most likely due to a direct interaction of the dye and the strong field rather than being due to a global hyperpolarization of the cellular membranes. This is a significant finding, since di-4 is one of the most common voltage-sensitive dyes used, and the results and conclusions of other studies may need to be reevaluated.

We showed that in this preparation, the endocardium has many more points of activation due to the more heterogeneous surface. We failed to detect a difference in activation times of the two surfaces in response to strong shocks, probably due to the thin

and somewhat translucent tissue that results in significant optical averaging with depth. Nevertheless, we showed using pacing data taken from RVs as they are rotated that the endocardium has more points of early activation than the epicardium, which is consistent with our original hypothesis. We observed a decreasing activation time for stronger 2 ms shocks which is consistent with other preparations. We did not observe an increase in activation time due to virtual anodes in our 2 ms shocks.

To our knowledge no one has attempted to relate field shock data with fiber geometry information obtained with DTMRI, or fiber direction data acquired by any other means. The initial results validate the approach, but improvements in protocol are needed. The relationship between VEP and the fiber geometry obtained is more complex than our original hypothesis. Using the DTMRI data in a model may yield predictions that match the experimental results, but that is beyond the scope of this experimental study.

7.7 References

1 Trayanova N, Skouibine K, and Aguel F. "The role of cardiac tissue structure in defibrillation". Chaos 8:221-233, 1998.

2 Trayanova NA, Roth,BJ, and Malden LJ. "The Response of a Spherical Heart to a Uniform Electric Field: A Bidomain Analysis of Cardiac Stimulation". IEEE Trans. Biomed. Eng. 40:899-908, 1993.

3 Trayanova NA, Roth BJ, and Malden LJ. "A Spherical Heart in a Uniform Electric Field: A Study of Cardiac Stimulation". Computers in Cardiology196 (Abstr.), 1994.

4. Tovar O, and Tung L. "Electroporation Of Cardiac Cell-Membranes With Monophasic Or Biphasic Rectangular Pulses". PACE 14:1887-1892, 1991.

5. Neunlist M., and Tung L. “Dose-dependent reduction of cardiac transmembrane potential by high-intensity electrical shocks”. Am. J. Physiol. Heart 42:H2817-H2825, 1997.

6. Aguel F , Debruin KA, KrassowskaW, and Trayanova NA. “Effects of electroporation on the transmembrane potential distribution in a two-dimensional bidomain model of cardiac tissue”. J. Cardiovasc. Electrophysiol. 10:701-714, 1999.

7. Jones JL, Jones RE, and Balasky G. “Microlesion Formulation in Myocardial Cells by High-Intensity Electric Field Stimulation”. Am. J. Physiol. Heart 253:H480-H486, 1987.

8 Knisley SB. “Transmembrane potentials at the ends of ventricular myocytes during electroporation during field stimulation”. Abstract. PACE 1994;17:838

9 DeBruin KA, Krassowska W. “Modelling electroporation in a single cell. I. Effects of field strength and rest potential”. Biophys J 77;1213-24, 1999.

10 Krassowska W. “Effects of electroporation on transmembrane potential induced by defibrillation shocks”. PACE. 18:1644-1660, 1995.

11 Neu JC, and Krassowska W. “Asymptotic model of electroporation”. Phys. Rev. E.59:3471-3482, 1999.

12 Tovar O, and Tung L. “Electroporation of cardiac cell membranes with monophasic or biphasic rectangular pulses”. Pacing Clin Electrophysiol. 14(pt 2):1887–1892, 1991.

13 Kodama I, Shibata N, Sakuma I, Mitsui K, Iida M, Suzuki R, Fukui Y, Hosoda S, and Toyama J. “Aftereffects of high-intensity DC stimulation on the electromechanical performance of ventricular muscle”. Am J Physiol. 267:H248–H258, 1994.

14 Neunlist M, Tung L. “Dose-dependent reduction of cardiac transmembrane potential by high-intensity electrical shocks”. Am J Physiol. 273:H2817–H2825, 1997.

15 Malkin,R.A., Guan,D.X., and Wikswo,J.P. “Experimental evidence of improved transthoracic defibrillation consistent with electroporation - Enhancing pulses”. IEEE Trans. Biomed. Eng. 53:1901-1910, 2006.

16 DeBruin KA, Krassowska W. “Electroporation and shock induced transmembrane potential in a cardiac fiber during defibrillation strength shocks”. Ann Biomed Eng 26:584-96, 1998.

17 Al-Khadra AL, Nikolski V, and Efimov IR. “The role of elctroporation in defibrillation”. Circ Res 87: 797-804, 2000.

18 Knisley SB, Trayanova N, Aguel F. “Roles of electric field and fiber structure in cardiac electric stimulation”. Biophys J 77:1404 –1417, 1999.

19 Wikswo JP, Lin SF, and Abbas RA. “Virtual Electrodes in Cardiac Tissue: A Common Mechanism for Anodal and Cathodal Stimulation”. Biophys. J. 69:2195-2210, 1995.

20 Efimov IR, Cheng Y, Yamanouchi Y, Tchou PJ. “Direct evidence of the role of virtual electrode-induced phase singularity in success and failure of defibrillation”. J. Cardiovasc. Eledctrophysiol., 11:86-868, 2000.

21 Efimov IR, Gray RA, and Roth BJ. “Virtual electrodes and deexcitation: new insights into fibrillation induction and defibrillation”. J Cardiovasc Electrophysiol 11: 339–353, 2000.

22 Evans FG and Gray RA. “Shock-induced epicardial and endocardial virtual electrodes leading to ventricular fibrillation via reentry, graded responses, and transmural activation”. J Cardiovasc Electrophysiol 15: 79–87, 2004.

23 Gray RA, Jalife J, Panfilov A, Baxter WT, Cabo C, Davidenko JM, Pertsov AM. “Nonstationary vortexlike reentrant activity as a mechanism of polymorphic ventricular tachycardia in the isolated rabbit heart”. Circulation. 91:2454-2469, 1995.

24 Gray RA, Chattipakorn N. “Termination of spiral waves during cardiac fi brillation via shock-induced phase resetting”. Proc Natl Acad Sci U S A. 102:4672–7, 2005.

25 Cheng Y, Mowrey KA, Van Wagoner DR, Tchou PJ, Efimov IR. “Virtual Electrode-Induced Reexcitation. A Mechanism of Defibrillation.”

26 Sidorov, VY, Aliev, RR, Woods MC, Baudenbacher F, Baudenbacher P, and Wikswo JP, “Spatiotemporal dynamics of damped propagation in excitable cardiac tissue”. Phys Rev Lett, vol. 91, no. 20, pp. 208104, 2003.

27 Fozzard HA, Schoenberg M. “Strength-duration curves in cardiac purkinje fibers: Effects of liminal length and charge distribution”. J. Physiol 226, 593-618, 1972.

28 Fast VG, Kleber AG. “Role of wavefront curvature in propagation of cardiac impulse”. Cardivasc Res. Feb;33(2):258-71, 1997.

29 Entcheva, E., Trayanova, N.A., and Claydon, F.J., “Patterns of and mechanisms for shock-induced polarization in the heart : A bidomain analysis”. IEEE Trans Biomed Eng, vol. 46, no. 3, pp.260-270, 1999.

30 Roth B.J., and Beaudoin, D.L., “Approximate analytical solutions of the Bidomain equations for electrical stimulation of cardiac tissue with curving fibers”. Phys. Rev. E, 67:051925, 2003.

31 Woods, M.C., “The Response of the Cardiac Bidomain to Electrical Stimulation”. Doctoral dissertation, Vanderbilt University, Chapter 6, 109-135, 2005.

32 Trayanova N, Skouibine K. “Modeling defibrillation: effects of fiber Curvature”. J Electrocardiol. 31:23–29, 1998.

33 Hunter PJ. Proceedings: “Development of a mathematical model of the left ventricle”. J Physiol (London). 241:87P–88P, 1974.

34 Hunter PJ, Smaill BH. “The analysis of cardiac function: a continuum approach”. Prog Biophys MolBiol. 52:101–164, 1988.

35 Hunter PJ, Nielsen PM, Smaill BH, LeGrice IJ, Hunter IW. “An anatomical heart model withapplications to myocardial activation and ventricular mechanics”. Crit Rev Biomed Eng. 20:403–426, 1992.

36 LeGrice IJ, Hunter PJ, Smaill BH. “Laminar structure of the heart: a mathematical model”. Am J Physiol. 272:H2466–H2476, 1997.

37 LeGrice IJ, Smaill BH, Chai LZ, Edgar SG, Gavin JB, Hunter PJ. “Laminar structure of the heart:ventricular myocyte arrangement and connective tissue architecture in the dog”. Am J Physiol. 269(2Pt2):H571–H582, 1995.

38 Nielsen PM, Le Grice J, Smaill BH, Hunter PJ. “Mathematical model of geometry and fibrous structure of the heart”. Am J Physiol. 260:H1365–H1378, 1991.

39 Vetter FJ, McCulloch AD. “Three-dimensional analysis of regional cardiac function: a model of rabbit ventricular anatomy”. Prog Biophys Mol Biol. 69:157–183, 1998.

40 Gray RA, Pertsov AM, Jalife J. “Incomplete reentry and epicardial breakthrough patterns during atrial fibrillation in the sheep heart”. Circulation. 94:2649-2661, 1996.

41 Scollan DF, Holmes A, Zang J, and Winslow RL. “Reconstruction of Cardiac Ventricular Geometry and Fiber Orientation Using Magnetic Reasonance Imaging”.

42 Hsu EW, Muzikant AL, Matulevicius SA, Penland RC, and Henriquez CS. "Magnetic resonance myocardial fiber-orientation mapping with direct histological correlation". Am J Physiol Heart Circ Physio`l 274:H1627-H1634, 1998.

43 Holmes AA, Scollan DF, Winslow RL. "Direct histological validation of diffusion tensor MRI in formaldehyde-fixed myocardium". Magn Reson Med 2000;44:157–161.

44 Muzikant AL, Hsu EW, Wolf PD, Henriquez CS. "Region specific modeling of cardiac muscle: comparison of simulated and experimental potentials". Ann Biomed Eng. 30:867– 883, 2002.

45 Fast VG, Rohr S, Gillis AM, Kleber AG. "Activation of Cardiac Tissue by Extracellular Electrical Shocks". Circ.Res. 82,375, 1998.

46 Entcheva E, Eason J, Efimov IR, Cheng Y, Malkin R, Claydon F, "Virtual electrode effects in transvenous defibrillation-modulation by structure and interface: evidence from bidomain simulations and optical mapping". J Cardiovasc Electrophysiol. Sep;9(9):949-61, 1998.

47 Fishler MG. "Syncytial heterogeneity as a mechanism underlying cardiac far-field stimulation during defibrillation-level shocks". J.Cardiovasc.Electrophysiol. 9,384, 1998.

48 Gurvich NL, Markarychev VA. "Defibrillation of the heart with biphasic electrical impulses". Kardiologiya. 7:109-112, 1967.

49 Walcott GP, Walker RG, Cates AW, Krassowska W, Smith WM, Ideker RE. "Choosing the optimal monophasic and biphasic waveforms for ventricular Defibrillation". J Cardiovasc Electrophysiol. 6:737–750, 1995.

50 Fast VG, Cheek ER, Pollard AE, and Ideker RE. "Effects of electrical shocks on Cai and Vm in myocyte cultures". Circ Res 94;1589-1597, 2004.

51 Fast VG, Sharifov OF, Cheek ER, Newton JC, Ideker RE. "Intramural virtual electrodes during defibrillation shocks in left ventricular wall assessed by optical mapping of membrane potential". Circulation. 106:1007-14, 2002.

52 Pitruzzello AM, Woods MC, Wikswo JP, and Lin SF. "Differences in Cardiac Activation Times for Endocardium and Epicardium in Response to External Electric Shock". Oral Presentation, First Joint BMES/EMBS Conference. 1999.

53 Sobie EA, Susil RC, and Tung, L. “A generalized activating function for predicting virtual electrodes in cardiac tissue”. Biophys. J., vol. 73, pp. 1410–1423, 1997.